Effects of Compressive and Tensile Fields On the Load Carrying Capacity of Headed Anchors

A DISSERTATION

SUBMITTED TO THE FACULTY OF THE GRADUATE SCHOOL

OF THE UNIVERSITY OF MINNESOTA

BY

Roberto Piccinin

IN PARTIAL FULFILLMENT OF THE REQUIREMENTS

FOR THE DEGREE OF

DOCTOR OF PHILOSOPHY

Roberto Ballarini, Advisor

February 2011

ACKNOWLEDGEMENTS

My gratitude to my advisor, Professor Roberto Ballarini, is very difficult to express through simple words. He has been a great advisor and a good friend in the last two years. His guidance, knowledge, and encouragement through my studies and my doctoral work will always be remembered. I also sincerely thank professors Luigi Biolzi, Sara Cattaneo, Arturo Schultz, and Henryk Stolarski for their support, their tireless dedication, and fruitful discussions. Finally, I would like to thank Professor Perry Leo (in addition to professors H. Stolarski and A. Schultz) for serving on my committee.

I would like to thank Mr. Daniele Spinelli and the staff of the Laboratorio Prove Materiali of the Politecnico di Milano, Italy, for their help in the experimental part of this work.

My thesis research was made possible by funding from the Civil Engineering Department and the James L. Record Chair. The experimental work of this research was carried out with the support of Yucatan Decima concrete precast plant and its technical staff.

I thank Marco Pravetoni, Raffaello Verardi, Keith Palmer, Jim Hambleton, Federico Galli, Bulent Mercan, Steven Wojtkiewicz and all the other people that have contributed to make my stay in Minnesota memorable and unforgettable. Their friendship really enriched my life.

Finally, this dissertation is dedicated to my parents Marco and Daniela, to my son Bryan, to my sister Francesca, and to my incredible girlfriend, Fatima. They deserve much more than what I can write here, but they should know that their support, their

approach to life and their strength will always be an example for me; and if it is true that hard work is always rewarded, please, consider this work as my little contribution to your rewards.

TABLE OF CONTENTS

LIST OF TABLES

LIST OF FIGURES

INTRODUCTION

This dissertation presents and discusses the results of a numerical and experimental fracture mechanics based investigation of the effects of initial compressive and tensile stresses on the pullout failure of headed anchors embedded in concrete.

A literature review of the different applications and design formulas to predict the ultimate pullout capacity of headed anchors is provided in Chapter 1. It is shown that currently available design procedures are based on fracture mechanics and that the pullout failure is governed by the propagation of a single, discrete crack. While experimentally based formulas are available for anchors embedded in cracked concrete, no provisions or investigations are available for anchors embedded in a compressively prestressed concrete matrix. It is concluded that a better understanding of the effect of initial compressive and tensile fields on the load-carrying capacity of headed anchors is needed.

In Chapter 2, linear elastic fracture mechanics (LEFM) analytical and numerical insights of the progressive pullout of headed anchors embedded in an unstressed and stressed concrete matrix are described. The effects of stresses on the ultimate load carrying capacity and on the load displacement behavior are calculated in terms of the brittleness number using the finite element method.

The experimental part of this study is described in Chapters 3 and 4. The effects of compressive stresses and embedment depths on the failure mechanisms of the anchors are investigated. Ultimate load-carrying capacity, load displacement curves, and crack paths are presented and discussed.

In Chapter 5, the results obtained in the experiments are compared qualitatively and quantitatively with the numerical predictions. It is concluded that the LEFM model adequately describes the failure of headed anchors. The experimental behavior of very shallow anchors suggests that a deterministic continuum theory cannot be applied if the embedment depth is much smaller than the maximum aggregate size. However, since the numerical model is based on LEFM concepts, the inclusion of the effects of the nonlinear zone (fracture process zone) ahead of the tip of the main crack is suggested.

In Chapter 6, the results from the numerical simulations involving the use of non-linear cohesive elements to simulate the effects of the fracture process zone are presented. Qualitative and quantitative results are obtained using a pre-defined crack path method and an incremental crack propagation approach. Limits and differences between the experiments and the two methods are discussed.

In Chapter 7, a design formula for the capacity of headed anchors that takes into account for compressive fields applied to the concrete matrix is suggested. Further conclusions together with some suggestions for the future research are drawn.

CHAPTER 1

ANCHOR BOLTS AND THE PULLOUT FAILURE

1.1 Background

Connections between building components play critical roles in the behavior and reliability of structures. Numerous techniques have been developed to join elements depending upon the type of construction, materials used, and the structural requirements. The wood construction industry has relied on specialized glues or fibers, while steel bolts or welding are still commonly used by the steel industry. Early fastening techniques developed by the concrete and masonry industries borrowed concepts from other construction trades (Eligehausen *et al.* [1]), including the use of cast metal joints and embedded metal studs. Today, more refined fastening technologies are being used, such as steel headed studs or anchors. Furthermore, the evolution of the construction industry has led to a competition between "cast-in-place" (CIP) inserts and "post-installed" anchors designed to be installed after the concrete has cured. Compared to established CIP techniques, the post-installed anchoring discipline is relatively young. Even though prescriptive standards are available to regulate their use and installation, it is not uncommon to design and install anchors in accordance to a specific experimental proof test or product manufacturer's approval.

Steel anchors are used in the building construction for two main purposes:

- Connect structural elements;
- Transfer external loads to the concrete or the base material;

The external loads that need to be transferred to the base material are most often tension (normal) or shear loads. In some cases, the shear load might be applied with a certain eccentricity, giving rise to rotational moments. There are also applications that involve combinations of normal and shear loads (Fig. 1.1).

Anchors are classified based on the way they are installed and the mechanisms they employ to transfer external loads to the base material (Fig. 1.2). CIP anchors are placed inside the formwork and cast into the concrete. The transferring mechanism involves aggregate (bearing) interlock between the surface of the anchor and the base material (Fig. 1.2a). Post-installed anchors present more flexibility and can be installed in the concrete matrix in any position and with any orientation, provided that a hole to contain them is pre-drilled in the base material. Conceptually, the post-installed anchors are classified as expansion anchors (torque or deformation controlled), undercut anchors, and bonded anchors, according to the way the external loads are transferred to the base material. Expansion anchors transfer the applied external loads by means of frictional stresses (Fig. 1.2b). These (holding) stresses distribute along the pre-drilled hole after external deformations (generally, an expansion or a torque) are applied during the installation process. Undercut anchors are built with spreading parts that take advantage of mechanical interlock between concrete and anchor. The undercutting process is completed after a hole is drilled in the concrete matrix. With this system, much lower expansion forces are generated during the installation and loading processes. That is why, in some particular cases and installation conditions (angle, embedment depth, and anchor diameter), undercut and CIP anchors behave similarly. Finally, external loads can be transferred to the concrete matrix by means of chemical interlock or bond (Fig. 1.2c). In

this case, the external loads are transferred to the base material through the bond and adhesion along the chemical material used during the anchor installation process.

Different types of failure are to be expected depending upon the way anchors are installed and loaded. For design and conceptual purposes, the types of failure that are of interest for concrete anchors are divided into failures under tension loading and failures under shear loading. Under tension loading, the fastening systems might experience five different types of failures:

- Steel failure;
- Pullout failure;
- Pullthrough failure;
- Concrete splitting;
- Concrete breakout;

Steel failure is generally associated to yielding of the anchor, and the load capacity is easily determined from the product of the yielding stress of the material and the cross sectional area of the anchor. The pullout (or pull-through) failures are a result of sliding out of the anchor (or part of it) from the concrete or by pulling out a relatively small portion of the concrete matrix. Currently, there is no established procedure to theoretically determine the design ultimate load for pullout, pullthrough, and splitting failures. For these cases, an estimate of the ultimate load needs to be supported by experimental evidence. The concrete breakout capacity can be estimated using formulas available from prescriptive standards.

The failure modes of fastenings loaded in shear are, with some exceptions, identical to those described for tension loads. Theoretically, a pullout failure may occur

only for small anchor depth to anchor diameter ratios and low values of the tensile capacity of the matrix. In addition, steel failure is often preceded by spalling of the concrete in front of the anchor, even for fasteners sufficiently far from the edges. Finally, a concrete pry-out failure may occur for single fastenings located quite far away from the edges. This type of failure might be triggered by groups of anchors depending upon their embedment depths and the properties of the base material.

1.2 Pullout and Breakout Failures

From a design point of view, a ductile failure is defined when yielding of the fastener or the system of fasteners occurs before any breakout of concrete (steel failure). This is the case when the base material does not fail, the steel material is sufficiently ductile, and the length of the anchor over which inelastic deformations appear is sufficiently large. A brittle failure involves breakout or splitting of the base material before yielding of the anchor (or group of anchors), or by steel failure when the length of the anchor over which inelastic deformations appear is small. Despite numerous investigations (Asmus and Eligehausen [2], Asmus and Ozbol [3]) on the splitting failure of anchors in concrete, a theoretical splitting failure load formula is not yet available. On the other hand, concrete breakout failure is a very practical and common design case. This type of failure is very often confused with the pullout failure. To some extent, they are very similar in that they both involve the pulling out of some portion of the concrete matrix. For this reason, in the concrete community, the concrete breakout failure is usually referred to as concrete pullout failure.

1.2.1 Previous Studies: Unstressed Concrete

Steel headed anchors embedded in a concrete matrix are widely used in structural engineering applications. Since the early 1980's, several approaches and standards have been made available to predict the ultimate pullout capacity of headed anchors in concrete subjected to direct tension and shear forces. Their load-carrying capacity can be predicted with confidence for cases in which the stem yields (steel failure); predicting the maximum load achieved during the progressive failure of the concrete, however, is much more difficult. In the beginning, predictions relied on two distinct approaches:

- Assumption of an average prescribed traction distribution acting along the surface of a conical section of concrete with an assumed shape (plasticity-type models);
- Regression analyses of experimental data;

For tension loads, the failure surface (Jensen and Braestrup [4]) is assumed to be a frustum of a cone with an inclination angle between 25 (for shallow embedments) and 45 degrees (for deep embedments) with the head of the anchor coinciding with the head of the cone.

Among the plasticity-based models, the capacity used to be computed as:

- The product between the actual surface area and an assumed average uniform tensile stress;
- The product between an average uniform tensile stress and an assumed surface area;

The first ACI Code provisions on the topic (ACI Committee 349-89 [5]) allowed the capacity of a headed anchor of diameter *c*, embedded at a depth *d*, to be determined using a uniform tensile stress, $f_t = 4\sqrt{f'_c}$, where f_t and f'_c are in psi, acting on the

projected area of a conical failure surface inclined at 45 degrees with respect to the free surface. The limit load derived using this model and the empirical relation between the tensile and compressive strengths, is given by

$$P_{u,ACI} = \phi f_t \pi d^2 \left(1 + \frac{c}{d}\right) = \left(\phi \cdot 4 \cdot \sqrt{f'_c}\right) \pi d^2 \left(1 + \frac{c}{d}\right) \approx f_t d^2 \tag{1.1}$$

where ϕ is the strength reduction factor. The value of the tensile stress considered in the original ACI 349 formula comes from the averaging of the principal stress distribution along the assumed failure surface. According to the original model, in fact, the tensile stress is maximum at the head of the anchor ($f_t = 6 - 7\sqrt{f'_c}$, psi) and linearly decreases to zero at the free surface along the assumed failure surface. It follows that the tensile stress value of $f_t = 4\sqrt{f'_c}$ psi, acting on the projected circular area, can be obtained by averaging. ACI 349 provides also some valuable insights on the inclination of the failure surface. In fact, it is observed that the failure surface is inclined at a 45 degree angle only in the first stages of failure. In the following stages, the angle of inclination is reduced by the so-called disc action. This is related to the fact that bending of the uncracked portion of the base material generates compression around the failure surface and, in turn, reduces the angle of propagation of the crack. The disc action is more significant for relatively shallow embedment depths less than 5 in.

In the early 1980's, the *k*-method was developed in Germany (Eligehausen *et al.* [6], Eligehausen and Fuchs [7]), in which the predicted capacities of headed anchors were obtained from regression analyses of available experimental data. The most important innovation in the method is represented by the assumption of a different angle of inclination of the failure surface. The propagation of the fracture process is assumed to be

at angles between 30 and 40 degrees with respect to the free surface. Some *k*-factors were used and calibrated to available experimental data. Their values were also calibrated to take into account for the interaction of several anchors, their distance from the edges of the concrete matrix, and the interaction between shear and normal loadings.

Experimental and analytical contributions to the plasticity-type models for the pullout of headed anchors were introduced by Jensen and Braestrup [4], Stone and Carino [8], and Krenchel and Shah [9]. In the latter, acoustic emission was used to detect the micro-cracking and the cracking activity in the concrete during pullout tests. The development of micro cracking at various levels of loading was observed by cutting sections in the uncracked portion of concrete and by adopting slow loading and unloading cycles. It was observed that cracks started at about 30 percent of the maximum load and that for loads up to about 65 percent of the peak load, cracking was primarily concentrated near the head of the anchor. These initial micro cracks were inclined 15-20 degrees with respect to the horizontal surface. These investigations focused on the meaning of the Lok-test (Jensen and Braestrup [4], Krenchel and Shah [9]), which is associated with a support ring that produces significant compression on the surface of the specimen above the anchor. At loads near peak secondary cracks were observed running from the head of the anchor to the inside edge of the supports with inclinations ranging from 25 to 45 degrees.

In addition to these studies, two very important investigations need to be mentioned. In the first, Klinger and Mendonca [10] showed that the available design guidelines based on the d^2-dependence were significantly incorrect and unconservative for typical embedment depths. They performed an extensive literature review on the

tensile capacity of anchor bolts, where the results from experimentally obtained ultimate capacities were compared to the strengths predicted by six different procedures available in the US. Results from 90 tests, including 37 of which the failure was governed by the concrete, were investigated. It was concluded that the tensile capacities governed by steel failures were reasonably predicted by all methods. Because of the small scatter, a reduction factor $\phi = 0.9$ was recommended for these cases. For the cases governed by concrete failures, all the procedures overestimated the capacity for the majority of the tests. Because of the large scatter, a smaller strength reduction factor ($\phi = 0.65 - 0.85$) was suggested.

In the second study, a round robin investigation on anchors was carried out to compare analytical and numerical results with tests performed at various institutions and laboratories. The investigations were proposed and assigned between 1988 and 1990. 27 research groups with more than 60 researchers from Europe, America, Asia, and Australia contributed with more than 300 tests and analyses. The final report was concluded only in 1998, with the contributions of Elfgren [11]. In the final report, results from plane stress and axi-symmetric stress analyses and tests are reported. Other noticeable investigations (Farrow and Klinger [12], Farrow *et al.* [13]) were carried out in the last two decades.

Despite its obsolete nature, a plasticity-based formula for the pullout capacity of headed anchors was adopted in the PCI handbook [14]. Based on the studies by Shaikh and Yi [15], the PCI formulation was adopting the same failure surface with the same inclination angle as in ACI 349-89 [5]. However, the uniform tensile stress considered was equal to $f_t = \frac{1}{\sqrt{2}} 4\sqrt{f'_c}$ psi. The reduction factor $\frac{1}{\sqrt{2}}$ was introduced because the

original formulation had already shown to be incorrect and unconservative for typical embedment depths. Such a reduction led to a capacity corresponding to a lower bound of the available test data. Other reduction factors were introduced to take into account for anchors placed near the edge of the concrete matrix and for groups of anchors. The failure due to shear loading was implemented with the same principles.

To resolve these uncertainties, Ballarini *et al.* [16, 17] approached the problem of predicting the ultimate load capacity of headed anchors and of determining what material property is measured by the Lok-test (Jensen and Braestrup [4]), using linear elastic fracture mechanics. In their investigation, a more fundamental approach than the ones used in previous studies was applied to determine qualitatively and quantitatively the mechanisms of the pullout failure. Their idea of approaching the problem using fracture mechanics concepts stemmed from the fact that in all the experimental investigations available at the time, the failure in the pullout process was dominated by the propagation of a single crack. A two dimensional linear elastic fracture mechanics (LEFM) model with a mixed mode crack was used to study the pullout of rigid anchor bolts. Their analytical model of the plate and propagating cracks relied on the Green's functions for a concentrated force and a dislocation in an elastic half space. Replacing the point actions with distributions enabled them to satisfy the boundary conditions through a system of singular integral equations. Numerical solution of the equations produced the mixed mode stress intensity factors, crack paths and load-carrying capacity.

The introduction of a fracture mechanics approach received immediate attention and support from the fastening community. It became abundantly clear that the plasticity based formulas were not only inaccurate and unconservative, but neglected the correct

dependence of the pullout strength on the embedment depth and the effects of size of concrete. A clear confirmation of the strong size effect in the pullout failure of headed anchors was provided by Bazant and Sener [18]. In their studies, pullout failures of reinforced concrete bars without anchors were investigated. They showed that the results were predicted accurately by LEFM. Further studies by Eligehausen and Ozbolt [19], Ozbolt and Eligehausen [20], and Bazant *et al.* [21] using nonlocal finite element models showed that the concrete's size effect for headed anchors pullout failures is very strong and determined that for relatively large embedment depths there is very little difference between LEFM and nonlinear fracture mechanics approaches.

LEFM is a one-parameter system for which the equilibrium nominal stress, σ_N, corresponding to a crack of length l, is proportional to $K_c l^{-1/2}$, where K_c is the fracture toughness (which can be expressed in terms of the critical energy release rate, G_c, and Young's modulus, *E*, through the Irwin relation, $G_c = K_c^2 / E$). Dimensional consistency demands that the pull-out force be of the form

$$P_{u,LEFM} \approx K_c d^{3/2} \tag{1.2}$$

Ozbolt and Eligehausen [20], Eligehausen and Sawade [22], Ozbolt *et al.* [23], Eligehausen and Ozbolt [24] performed experimental and numerical investigations of numerous pullout tests and proposed a LEFM-based formula.

Use of Eq. 1.2 requires a fracture toughness test. Eligehausen and Ozbolt [24] and Fuchs *et al.* [25] proposed a formula based on an empirical relation between fracture toughness and the more easily measured compressive strength of the concrete

$$P_{u,LEFM} \approx K_c d^{3/2} \approx k_c \cdot \sqrt{f'_c} \cdot d^{3/2} \tag{1.3}$$

where k_c is the proportionality factor introduced by Fuchs *et al.* [25] in the Concrete Capacity Design (CCD) method and set equal to a constant value, independent of the embedment depth of the anchor. The CCD method represents the most recent approach for the design of cast-in place inserts. It is based on the *k*-method, and because of their common origin, the two methods predict similar capacities. The CCD method represents an advantage because:

- the anchor capacity is computed based on a 35 degree inclination angle with respect to the free surface and it uses a simpler geometry based on a rectangular failure prism (to take into account for edge distances and group effects) (Fig. 1.4);
- the $d^{3/2}$-dependence takes into account for concrete's size dependent fracture toughness and have been validated through numerous experiments;

ACI 318 started to include information on the behavior and design of concrete inserts since 2002 in one of its appendices (Appendix D) [26]. The procedure used by ACI 318 for cast-in-place anchors was developed from the CCD method limiting the design strength of concrete to 10,000 psi. Similar to the CCD method, the effects of edge and anchor spacing are taken into account by using simple shapes for the projected stress areas (rectangular, i.e.). Analogous design formulas based on fracture mechanics have been incorporated into several design codes and provisions (i.e., CEB-1997 [27], ACI 318-2008 [28], ACI 349-2006 [29], etc.).

Recently, Lee *et al.* [30] presented test results for large cast-in-place anchor bolts in concrete. The tests were intended to cover the lack of knowledge and provisions provided by ACI 318, Appendix D [26] and ACI 349-2006 [29], Appendix B. 20 Pullout tests were performed with an embedment depth greater than 25 in. and diameter greater

than 2 in. It was found that the slope of the concrete cone was much flatter than 45 degrees and that the CCD method was conservative for large embedment depths. The authors supported their conclusions suggesting that the CCD method was based on LEFM considerations, which are valid only for anchors with high bearing pressure, that is, anchors with small heads. In addition to this, for large head diameters, the failure angle was not 35 degrees but in the range of 25-30 degrees. The authors proposed then some modifications to the CCD method, changing the power of the exponent on the embedment depth in the pullout formula when large embedments or head diameters are employed.

The behavior of cast-in-place inserts in high-strength concrete under tensile loads was investigated by several authors. Primavera *et al.* [31] preformed tests on anchors embedded in 7,500 and 12,000 psi concrete. Failures were observed to reflect the cone-shaped surface. All anchors were observed to experience an increase in capacity with increasing strength. The load displacement behavior was strictly related to the strength of the concrete. Increasing the strength from 7,500 to 12,000 psi resulted in curves with higher initial stiffness and a more defined ultimate capacity. For all the tests, the inclination of the failure planes ranges between 21 and 28 degrees, contradicting the range of 35 to 45 degrees assumption in the current design methods. However, this supports the Commentary of ACI 349-2006 according to which shallower failure plane inclinations might occur due to disc action. The authors proposed to extend the validity of ACI 349 statement to embedment depths up to 8 in. Furthermore, it was concluded that the CCD method over predicted the capacity of the anchors proportionally to the concrete strength.

Similar conclusions were drawn by Cattaneo [32]. In their study, the behavior of wedge-type anchors in normal and high strength fiber reinforced concrete (HPC) was investigated. Again, the experimental evidence suggested that the use of HPC leads to higher capacities than those observed for normal strength concrete. In HPC the specimens exhibited a more ductile behavior, a reduced cracking pattern and cone diameter. Minor modifications to the CCD method were proposed, but the accuracy and ease of use of the method were considered still quite important. The problem could not be generalized because of the type of anchors investigated.

1.2.2 Previous Studies: Stressed Concrete

After an extensive experimental program (Eligehausen and Balogh [33]), the capacities obtained from Eq. (1.3) were reduced to account for cracking due to external loads (i.e., tension zones, negative moment loading conditions) or imposed deformations (i.e., creep, shrinkage, temperature) in the region where the anchor is placed. In most of the tests performed to assess the effect of concrete cracking (Eligehausen *et al.* [34]), cracks were preformed in a reinforced concrete matrix and their width was kept nearly constant by constraining the specimen. Subsequently, the anchors were monotonically loaded to failure. Concrete cone failures were observed and compared to the uncracked case; the load-displacement curves showed to be flatter, the ultimate load was markedly reduced, and the displacement at failure increased. Analyses of the experimental data indicated that for an average crack width of about 0.012-0.016 in., the concrete cone failure load for cracked concrete is about 75 percent of the value in uncracked concrete. In the case the anchors are located at the intersection of two cracks, the concrete failure

load is further reduced by about 20 percent. The reason for the reduction in capacity, according to these studies, is the disturbance of the axi-symmetric stress field, which reduces the surface area over which tensile stresses are redistributed. Eligehausen and Ozbolt [24] carried out nonlinear finite element analyses of headed anchors located in a crack and found that when a fastener is situated in a crack of sufficient width to prevent transfer of tensile stresses through its faces, the stress distribution within the concrete is altered and the surface area available for transfer of the tensile forces is decreased. Even though representative of many practical applications, it appears that the presence of reinforcement and the restraint applied to the cracked concrete matrix (to maintain a constant crack width) might not provide a complete understanding of the effect of transversal tension on the ultimate load carrying capacity of the inserts.

The problem of predicting the load-capacity of cast-in-place inserts placed in precast, prestressed concrete members to facilitate connections between different elements has received much less attention. In fact, ACI 318 does not provide modifications to Eq. (1.3) that account for prestress. The connection of cast-in-place concrete diaphragms or floor beams to precast concrete girders in bridges is but one example of applications involving prestress (Fig. 1.5).

Baran *et al.* [35] performed experiments on different types of cast-in-place inserts to determine the influence of reinforcement and prestress. As expected, they observed that the presence of a prestressing force in the direction orthogonal to the axes of the inserts embedded in reinforced concrete resulted in an increase in load capacity and ductility. 32 pullout tests on four different types of inserts were carried out in unreinforced and reinforced concrete, with and without axial compression. An increase in

capacity was noted for the reinforced concrete cases. Also, the behavior was more ductile and large deformations were observed before failure. The presence of axial compression slightly increased the capacities of the inserts, and when reinforcement spacing was reduced, effects similar to the presence of axial compression were observed. Failure cone inclination angles for the unreinforced specimens ranged from 29 to 45 degrees and were consistent with the large number of observations for the prediction of concrete pullout strength. Comparison with the actual code provisions were carried out and a discussion on the necessity to use or avoid the reduction factor for cracked concrete was completed. Because these tests were conducted in support of a larger study on the stability of precast concrete pedestrian bridges, the studies on the effect of compressive stresses applied to the concrete matrix are quite limited and, above all, they do not provide any design formula or recommendation.

1.3 Objectives

Because of the lack of knowledge and the absence of a design formula, the aim of this investigation is to understand and provide qualitative and quantitative insights on the behavior of headed anchors embedded in a stressed concrete matrix. Since experiments and previous investigations have shown that the above mentioned failure is dominated by the propagation of a single crack, fracture mechanics concepts will be used to characterize the mechanisms of the problem. Both compression and tension of the concrete matrix will be investigated. The latter case will be investigated to observe the differences between the actual code provisions for cracked concrete and the effective behavior of anchors in a concrete matrix undergoing tension.

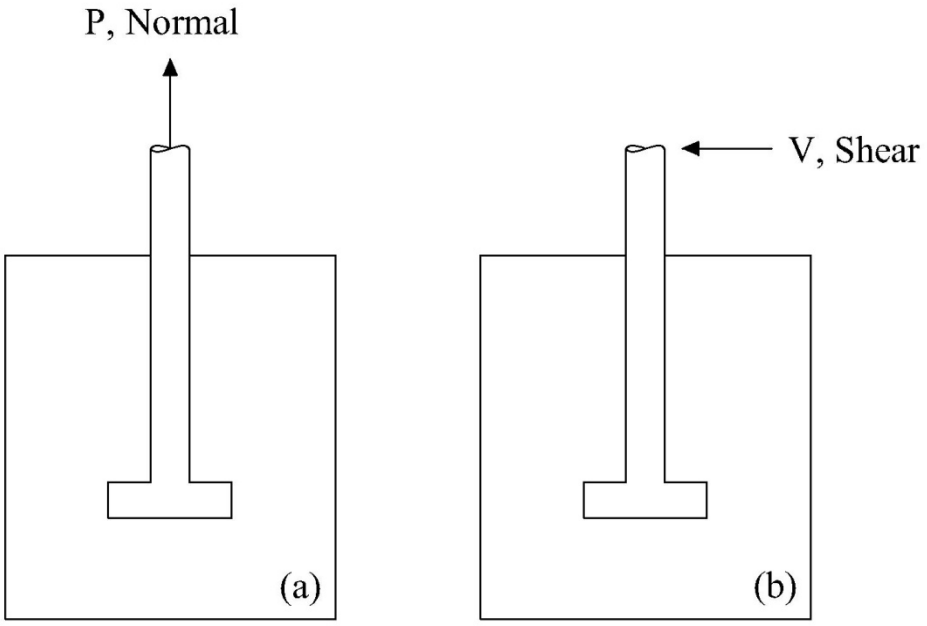

Fig. 1.1 – Types of loading involved in anchor's design

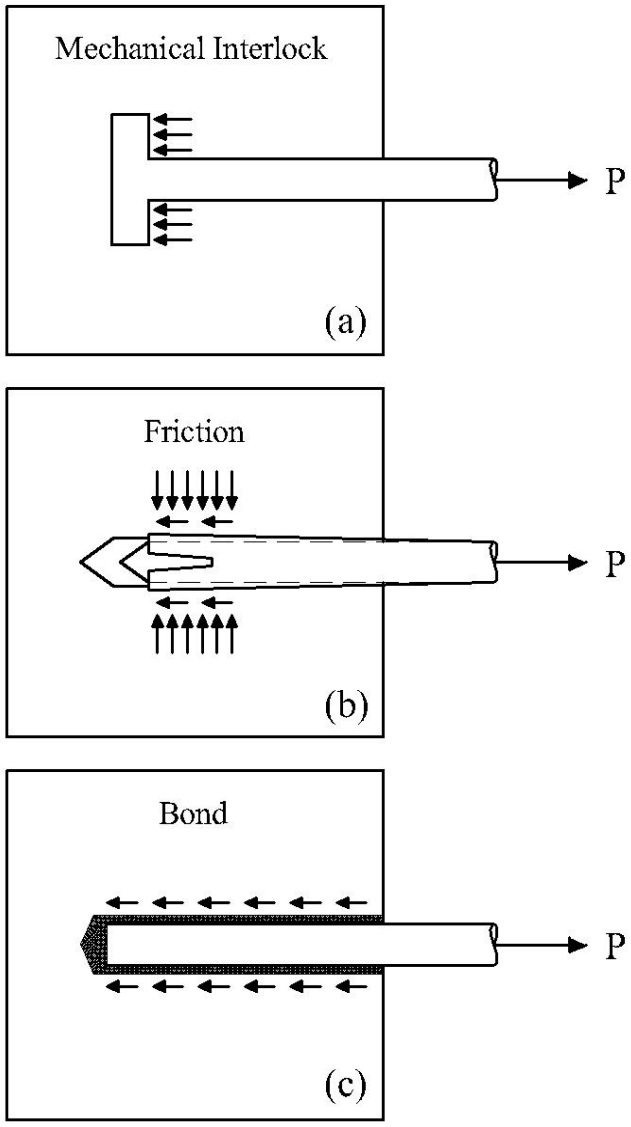

Fig. 1.2 – Fundamental mechanisms of load transfer for different concrete anchors

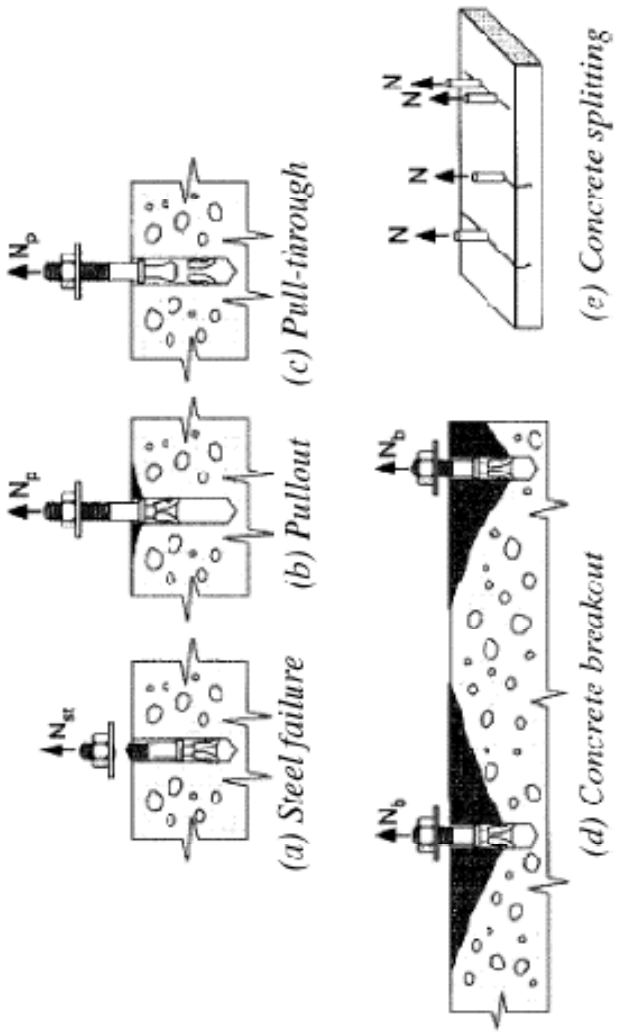

Fig. 1.3 – Failure modes for anchors under tensile loading (Fuchs *et al.* [25])

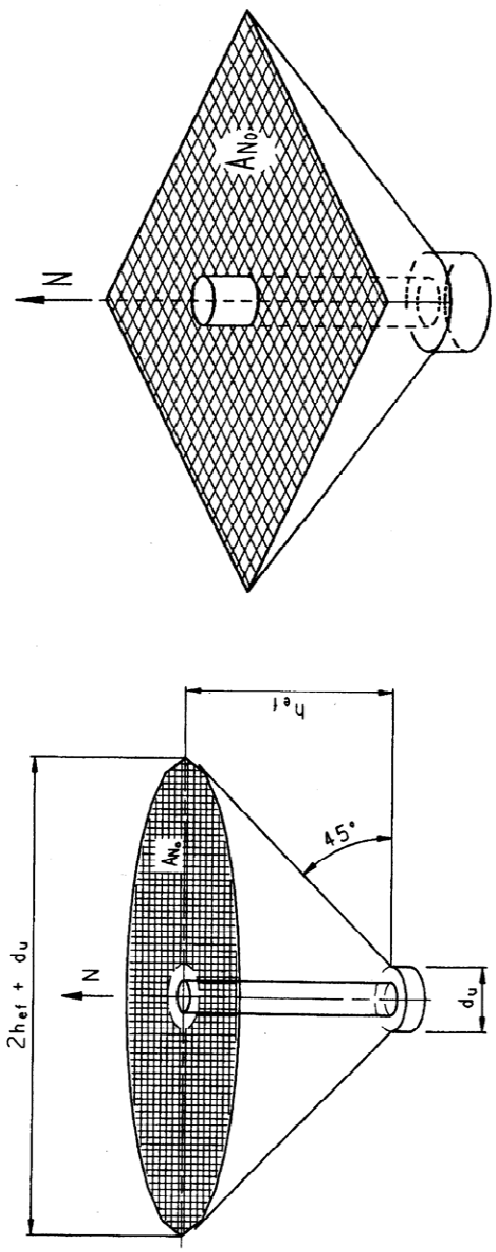

Fig. 1.4 – Comparison of surfaces of failure; ACI 349 (cone, left), CCD method (prism, right) (Fuchs *et al.* [25])

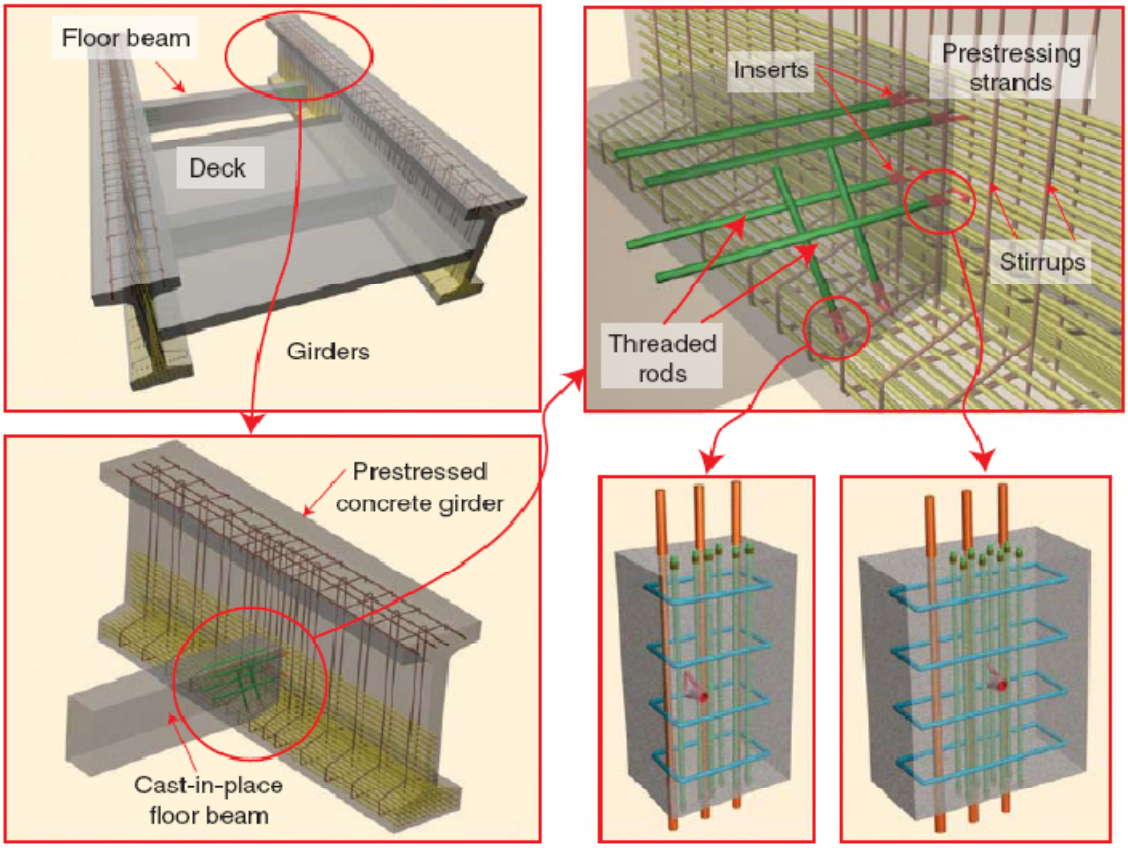

Fig. 1.5 – Example of installation of steel anchors in prestressed concrete members (Baran *et al.* [35])

CHAPTER 2

LINEAR ELASTIC FRACTURE MECHANICS INVESTIGATION

In this chapter, a finite element investigation is carried out to determine the effects of tensile and compressive residual stresses on the ultimate load carrying capacity and load-displacement response of headed anchors.

Linear elastic fracture mechanics concepts are introduced and reviewed in Appendix A. In that section, the limitations and applicability of those concepts to model fracture mechanics with the aid of numerical methods, and in particular, the finite element method, are also discussed.

2.1 The Brittleness Number

Plasticity-based and LEFM models provide useful upper bounds on the strength of a structure containing a crack. The smooth transition from ductile to brittle failure can be characterized using nonlinear fracture mechanics models, including those of the cohesive zone type. The concept of brittleness or ductility of a structural failure has been widely investigated since LEFM concepts were introduced. However, a well established definition of brittleness does not exist. One of the fundamental reasons is that the apparent brittleness of a structural failure depends simultaneously on the geometry of the structure, the material properties, the size of the structure, and the loading conditions.

The parameter β was introduced by Cherepanov [36] and is defined by

$$\beta \equiv \frac{L}{r_p} \approx \frac{f_t^2 L}{K_c^2} \tag{2.1}$$

where r_p is the length of the "process zone" (micro cracking and aggregate interlock) that develops in the vicinity of a very long crack and L is a characteristic dimension of the structure. β is referred to by the concrete fracture mechanics community as the brittleness number (Bazant and Planas [37]; note that Carpinteri [38] defines the brittleness number as $s = \beta^{-1}$). It is important to note that the brittleness number does not reflect the complex and potentially important interaction between a relatively large plastic zone and free boundaries. Therefore, the value of brittleness assigned to a specimen configuration through the use of a particular structural dimension in Equation (2.1) may not be representative of the brittleness of a different configuration comprised of the same material. For example, as pointed out by Bazant and Planas [37], valid toughness testing requirements for notched beam-like specimens, where the characteristic dimension L is taken as the beam depth, suggest the approximate constraint $\beta \geq 2.5$. However, for concrete anchors applications, where the characteristic length L can be taken as the embedment depth (which is typically much smaller than the dimensions of a beam structure) it is not uncommon to find values of $\beta \leq 1$ (Elfgren and Ohlsson [39]).

It is noted that the brittleness number as defined in (2.1) is proportional to Irwin's first estimate of the plastic zone size in metals (Irwin [40]).

Based on the aforementioned assumptions, Fig. 2.1 illustrates that the brittleness number determines whether failure is of the strength limited ductile type (defined in terms of some normalized maximum nominal stress, $\sigma_N^{\max}$), or of the toughness limited brittle type. Noting that L is proportional to d, and that any choice of nominal area

scales as d^2, plasticity predicts a size-independent strength, while linear elastic fracture mechanics predicts a $1/\sqrt{\beta}$ -dependence of strength.

The design formulas that are now available in design codes for headed anchors embedded in non-stressed concrete are the fruits of LEFM and nonlinear fracture mechanics models that have captured the transition illustrated in Fig. 2.1. As stated previously, no formulas are currently available that account for prestress or compressive stresses within the concrete; hence the motivation behind the LEFM model presented next.

2.2 Dimensional Analysis and Finite Element Model

In his studies, Ballarini *et al.* [16, 17] investigated the pullout failure mechanism by using fracture mechanics concepts. These involved the investigation of the propagation of discrete cracks emanating from the edges of the head of the anchor and propagating to the free surface, with different boundary conditions (i.e., location of support reactions). In his two-dimensional analyses, the anchor was modeled as a vertically loaded rigid plate in an elastic half-space. The top part of the plate was perfectly bonded to the elastic medium while the bottom part was free. Vogel and Ballarini [41] provided a finite element solution to the anchor pullout problem embedded in an unstressed concrete matrix in an axi-symmetric elastic space. Their study involved also anchors embedded in a plane strain configuration, validating the studies performed earlier by Ballarini *et al.* [16, 17].

Consider the idealized geometry shown in Fig. 2.2. Because of symmetry, only half cylindrical space is modeled. The dimensions of the axisymmetric cross section were

chosen based on the results of a preliminary investigation that determined that the propagating cracks would not interact with the truncated boundaries and that a uniform distribution of the prestress, σ, existed in the vicinity of the head of the anchor and the propagating crack front. The anchor bolt, embedded at a depth *d* within a matrix stressed to a level, σ, is represented by an infinitesimal discontinuity of diameter c with a rigid top surface (displacements restrained in all direction) and a traction-free lower surface. The stem and the thickness of the anchor are neglected. The curvilinear distance of the traction free crack front from the edge of the anchor is defined by l. The pullout load, P, is represented by the resultant reactive force on the top surface of the discontinuity produced by a uniform stress, p, applied along the bottom surface of the cylindrical model. The applied stress can be normalized as $\lambda = \frac{\sigma}{f_t}$ (Note that for the compressive case $\lambda > 0$, while for the tension case $\lambda < 0$).

Following Vogel and Ballarini [41], linearity and dimensional consistency in the solution of the pullout problem demand that the load associated with a given equilibrium crack length, l, is on the form

$$P_{LEFM} = f_1\left(\frac{l}{d}, \frac{d}{c}, \nu\right) \cdot K_{Ic} \cdot d^{1.5} \tag{2.2}$$

where ν is the Poisson's ratio (here assumed to be equal to 0.2). When a stress, σ, is applied to the elastic matrix orthogonally to the axis of the anchor, for the same equilibrium crack length, l, the load can be expressed as follows

$$P_{LEFM} = f_1\left(\frac{l}{d}, \frac{d}{c}, \nu\right) \cdot K_{Ic} \cdot d^{1.5} + f_2\left(\frac{l}{d}, \frac{d}{c}, \nu\right) \cdot \sigma \cdot d^2 \tag{2.3}$$

It follows that the maximum load, representing the pullout capacity, is

$$P_{u,LEFM} = \text{Max}[\, f_1\left(\frac{l}{d}, \frac{d}{c}, \nu\right) \cdot K_{Ic} \cdot d^{1.5} + f_2\left(\frac{l}{d}, \frac{d}{c}, \nu\right) \cdot \sigma] \tag{2.4}$$

Recalling the analytical expressions for the brittleness number and the applied stress, the pullout load can be written in terms of β and λ as

$$\frac{P_{u,LEFM}}{f_t \cdot d^2} = \text{Max}[\, f_1\left(\frac{l}{d}, \frac{d}{c}, \nu\right) \cdot \frac{K_{Ic}}{f_t \cdot d^{0.5}} + f_2\left(\frac{l}{d}, \frac{d}{c}, \nu\right) \cdot \frac{\sigma}{f_t}]$$

$$= \text{Max}[\, f_1\left(\frac{l}{d}, \frac{d}{c}, \nu\right) \cdot \frac{1}{\sqrt{\beta}} + f_2\left(\frac{l}{d}, \frac{d}{c}, \nu\right) \cdot \lambda] \tag{2.5}$$

The same normalization procedure can be used to investigate the obsolete ACI 349-89 [5] and the current ACI 318 formula [28] for the prediction of the pullout capacity of headed anchors. Considering the plasticity-based approach, the design formula

$$P_{u,ACI} = \phi \cdot f_t \cdot d^2 \cdot \pi \cdot \left(1 + \frac{c}{d}\right) \tag{2.6}$$

becomes, after normalization, of the form

$$\frac{P_{u,ACI}}{f_t \cdot d^2} = \phi\pi \cdot \left(1 + \frac{c}{d}\right) \tag{2.7}$$

Similarly, the formula based on the CCD method

$$P_{u,CCD} = k_c \cdot f_t \cdot d^{1.5} \tag{2.8}$$

can be normalized as follows

$$\frac{P_{u,CCD}}{f_t \cdot d^2} = k_c \cdot d^{-0.5} \tag{2.9}$$

Based on the illustrated dimensional analyses and with the aid of the finite element method, a series of incremental discrete finite element numerical simulations was carried out.

As it is typically assumed in LEFM incremental analyses of brittle and quasi-brittle materials, the crack is propagated when the Griffith equilibrium condition is reached (K_I for a given crack length l becomes equal to the fracture toughness K_{IC} of the material). FRANC-2D [42], a program that possesses automatic remeshing capabilities, was used to calculate the stress intensity factors and crack extension direction of the propagating front. The stress intensity factors were determined using the displacement correlation method (Barsoum [43]), and the crack path was selected using the maximum hoop stress criterion (Broek [44]). A representative deformed finite element mesh of the described configuration is shown in Fig. 2.2. It is noted that the model's predictions for ultimate capacity and load versus displacement behavior should be considered from the perspective of (i) an idealized geometry that neglects the effects produced by the precise geometry of embedded anchors and the radial cracking that often accompanies the crack propagation simulated in this work and (ii) a homogeneous material that neglects the intrinsic heterogeneity of concrete.

2.3 Results

In this section, the results from the incremental LEFM finite element analyses are presented. First, the results for the case of an unstressed matrix will be shown and discussed. These results will be compared to the available design code provisions for headed anchors. Secondly, the effect of stresses on the propagating crack front and the results of the numerical simulations involving a stressed matrix will be presented. Results include pullout capacities and load versus displacement behavior.

2.3.1 Unstressed Concrete

Load Carrying Capacity

Representative results for f_1 (Eq. (2.2)) as functions of crack length are shown in Fig. 2.3a. The maxima of each curve were used to establish Fig. 2.3b, which shows the normalized load carrying capacity as functions of embedment depth for several values of the brittleness number.

The results from the incremental analyses were used to provide comments and observations to the current and past formulations adopted by ACI 318 [28] and ACI 349-89 [5] for the pullout capacity of headed anchors. Fig. 2.4a, where the capacities predicted by Eq. (2.5), (2.7), and (2.9) are normalized by the ultimate capacity at the embedment depth $d/c=1$, illustrates that the obsolete plasticity-based formulation is inaccurate and unconservative for relatively large embedment depths. On the other hand, the results from LEFM are very close to the predictions of the ACI 318 code.

The normalized ultimate capacities obtained from the LEFM investigations were also used to establish Fig. 2.4b, where the capacities predicted by Eq. (2.5) and (2.9) were normalized by the ultimate capacity at the embedment depth $d/c=10$. With an experimentally calibrated constant factor, k_c, embedded in its formula, and with the assumption that exact pull-out forces are being provided, the ACI 318 code-based prediction is ideally represented by a horizontal line while results from the LEFM incremental analyses show that the ultimate load carrying capacity slightly decreases with increasing d/c.

Fig. 2.4b provides valuable information. First, and as clearly demonstrated by previous experimental investigations (Ozbolt and Eligehausen [20]), it shows that for

relatively large embedment depths there is very little difference between the LEFM predictions and the ACI 318 code-based formula. For relatively small embedment depths, however, the code-based formula is associated with pull-out forces that are lower than the upper bound LEFM predictions. Fig. 2.4b thus shows that predicting the ultimate capacity for $d/c < 2$ may require nonlinear fracture mechanics models that account for the process zone that accompanies a propagating crack front. Whether this is the case will be explored through a comparison of experiments with theory in subsequent chapters.

Load versus Displacement Behavior

The load displacement behavior of headed anchors in stressed and unstressed concrete provides the work of fracture, *WOF*, defined as the area under the force-displacement curve. The load-point displacement, Δ, in the simulations is defined as the relative displacement between the top and the bottom surfaces of the discontinuity defining the anchor (Fig. 2.2).

The normalized work of fracture can be written as

$$WOF_n = \frac{E}{f_t^{\,2} \cdot d^3} WOF = \int_0^{\Delta_{\max}} \left(\frac{P}{f_t d^2} \right) d\left(\frac{E\Delta}{d f_t} \right) \tag{2.10}$$

and represents the area under the normalized force-displacement curves.

Fig. 2.5 shows the load versus displacement behavior for a given brittleness number and zero stress. As expected, relatively deep embedments ($d/c = 10$) lead to snap-back instabilities. It is noted that the crack propagation simulations showed that as the crack approaches the free surface the convergence to zero force is very slow. Therefore the curves shown are truncated when the crack front reaches a distance from the free surface that is equal to ten percent of the embedment depth.

2.3.2 Stressed Concrete

The effects of compressive or tensile stresses on the load carrying capacity were first investigated by observing their influence on the pullout crack propagating front.

The compressive stress produces two effects that increase the load-carrying capacity and the ductility of the anchor. The close-up view of the tip of the traction free crack (Fig. 2.6a), shows that the first contribution is made by the component of the stress acting perpendicular to the line defining the crack surfaces (the components of stress associated with the applied loading are not shown in this figure). This stress resists crack opening, and in turn crack extension. The second contribution, also shown in the figure, is from the component of the prestress in the direction parallel to the line defining the crack surfaces. The direction of this stress increases the algebraic value of the Mode-II stress intensity factor, changes the direction of maximum hoop stress, and as shown in Fig.2.7, steers the crack front parallel to the free surface and the direction of the prestress.

Tensile stresses, as shown in Fig. 2.6b, produce the opposite effects, facilitating crack opening and steering the crack front towards the free surface.

Load Carrying Capacity

The effects of prestress on load-carrying capacity for selected values of λ and β are shown in Figs 2.8a-e. As indicated by LEFM-derived Eq. (2.5), the load-carrying capacity varies linearly with prestress. Figs. 2.9a-d illustrate Eq. (2.5) prediction of an inverse square root decrease in strength with increasing brittleness.

For $\beta = 2.5$ a modest but significant increase of the order of 15-20% is achieved for the largest value of prestress of practical relevance, $\lambda \sim 0.4 - 0.6$. For more typical

values of $\beta < 1$, however, even for large values of prestress ($\lambda \sim 1$), the increase in capacity is approximately 15% at most.

For tensile prestress, the model predicts that for $\beta = 2.5$ and $\lambda = -0.6$ there is a reduction in ultimate load capacity of the order of 25-30%. Again, for values of $\beta < 1$, the reduction in capacity is equal to about 15%.

For $0.1 \le \beta \le 10$ and $0 \le \lambda \le 1$, the following equation represents a sufficiently accurate fit of the results for ultimate capacity

$$\frac{P_u}{f_t d^2} = \frac{3.15}{\sqrt{\beta}} + 0.53\lambda \tag{2.11}$$

Eq. (2.11) provides a basis for the development of a design formula for ultimate capacity that accounts for prestress.

Load versus Displacement Behavior

From the normalized load versus displacement curves shown in Figs. 2.10a-d it can be observed that when a confining (compressive) prestress is applied the increase in dissipated energy in the post-peak is large, while the increase in ultimate load is modest. This increase is a result of the significant increase in the length of crack propagation, as shown in the representative plots in Fig. 2.7. The opposite is true when tensile stresses are applied to the concrete matrix. As expected from the unstressed case, relatively deep embedment and tensile prestress lead to snap-back instabilities in the load-displacement curve. Similarly to the unstressed case, the curves shown are truncated when the crack front reaches a distance from the free surface that is equal to ten percent of the embedment depth.

Crack Initiation Angles and Crack Paths

The LEFM simulations showed that the crack initiation angle (around the head of the anchor) is at equal to 15 degrees at most with respect to the free horizontal surface. This angle slightly increases up to 30 degrees when the crack propagates and reaches about 30 to 50% of its total length. When approaching the free surface, the crack steers parallel to its orientation. This is not surprising, since the external surface is stress free and the pullout load might be seen as a point load applied at the free end of a cantilever beam.

When prestress is applied, the initiation angle decreases and so the overall crack path inclination up to the surface. Crack paths plots obtained from the LEFM simulations can be found in Chapters 5, 6, and Appendix B.

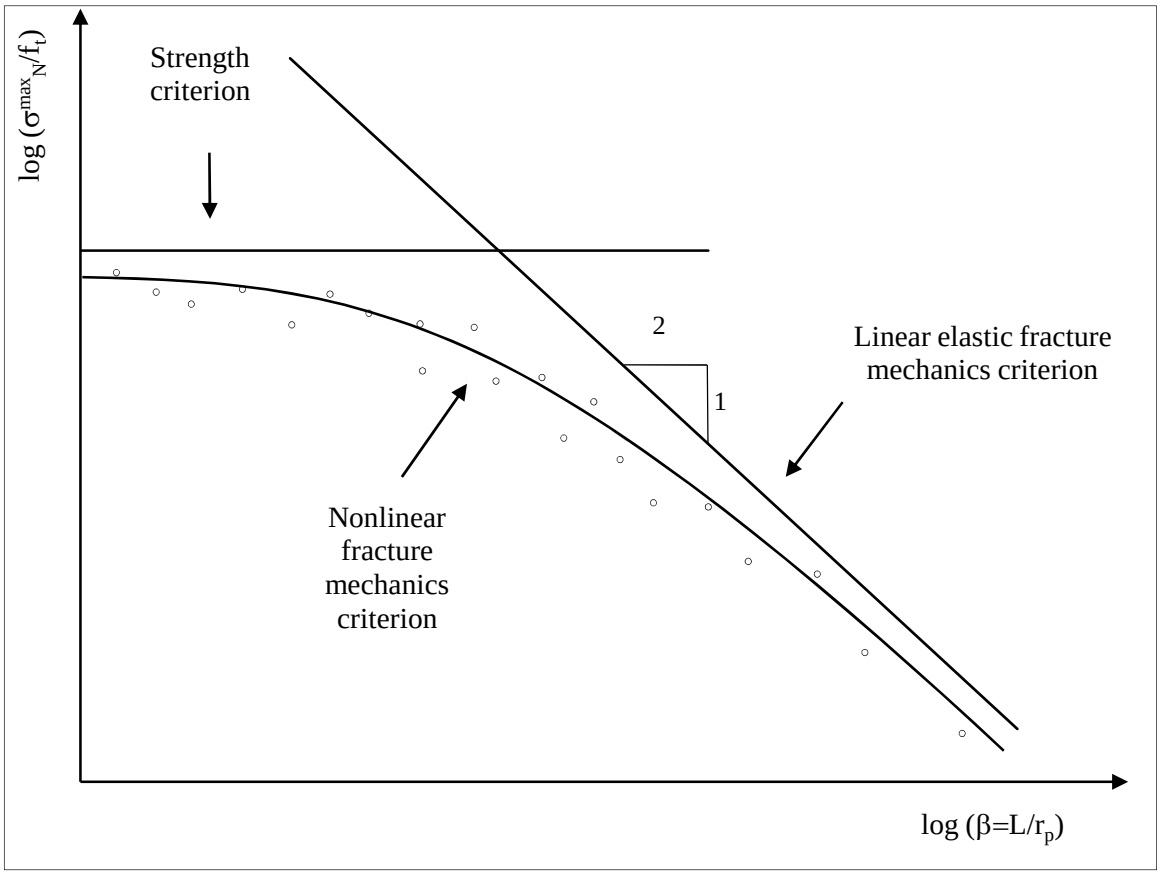

Fig. 2.1 – Nominal strength versus structural size

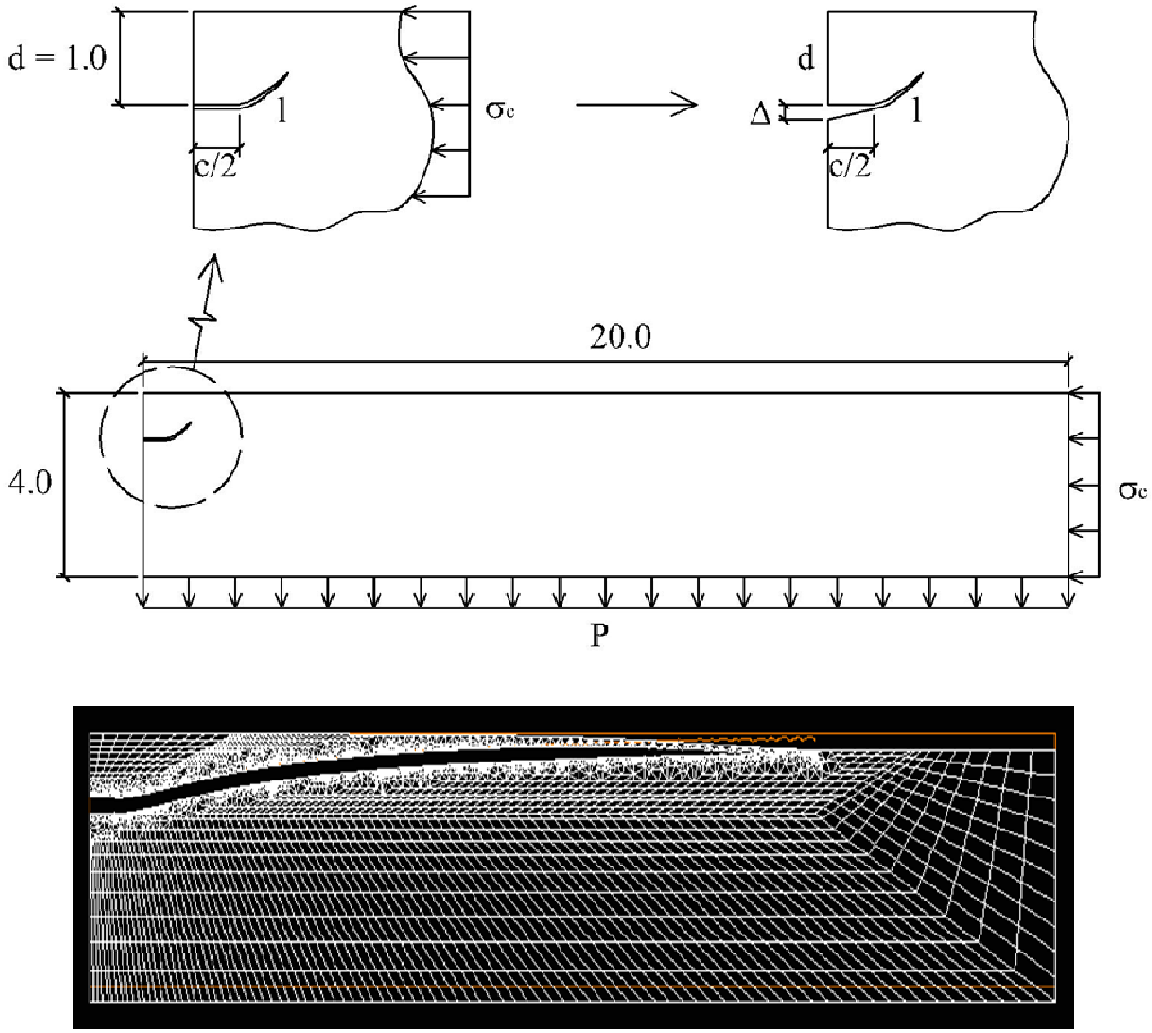

Fig. 2.2 – Cross section of the axisymmetric headed anchor model under prestress. The axis of rotation/symmetry is represented by the left edge of the section (Top); Finite element discretization of the axisymmetric headed anchor ($d/c=1$) with detail of the deformed configuration at the end of the crack propagation simulation (Bottom)

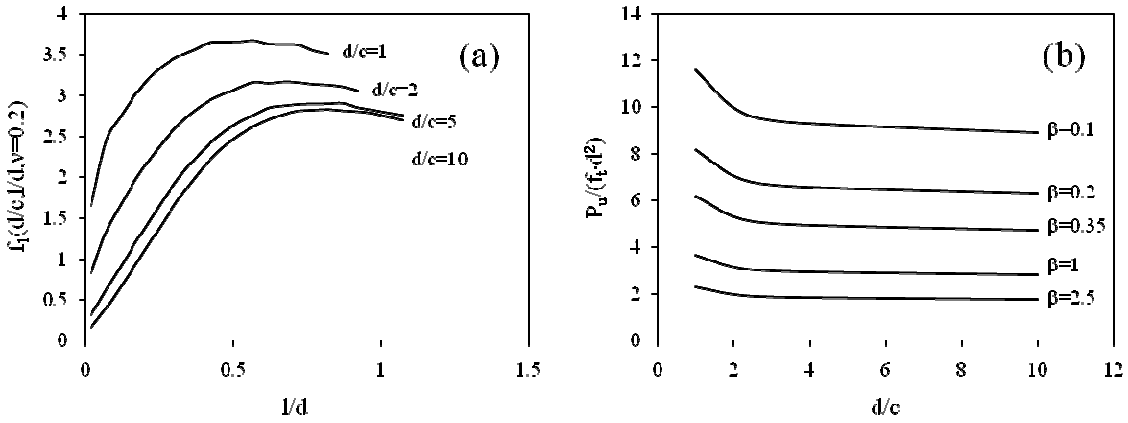

Fig. 2.3 – (a) Function f_1 as functions of crack length and embedment depth; (b) Ultimate normalized load as functions of embedment depth

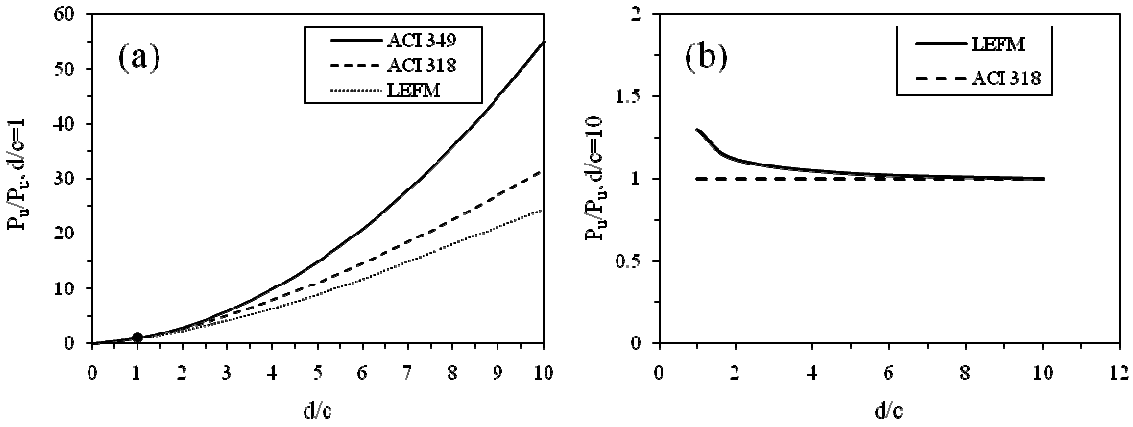

Fig. 2.4 – Ultimate load P_u normalized by the ultimate load for a headed anchor embedded at a normalized depth (a) $d/c = 1$; (b) $d/c = 10$

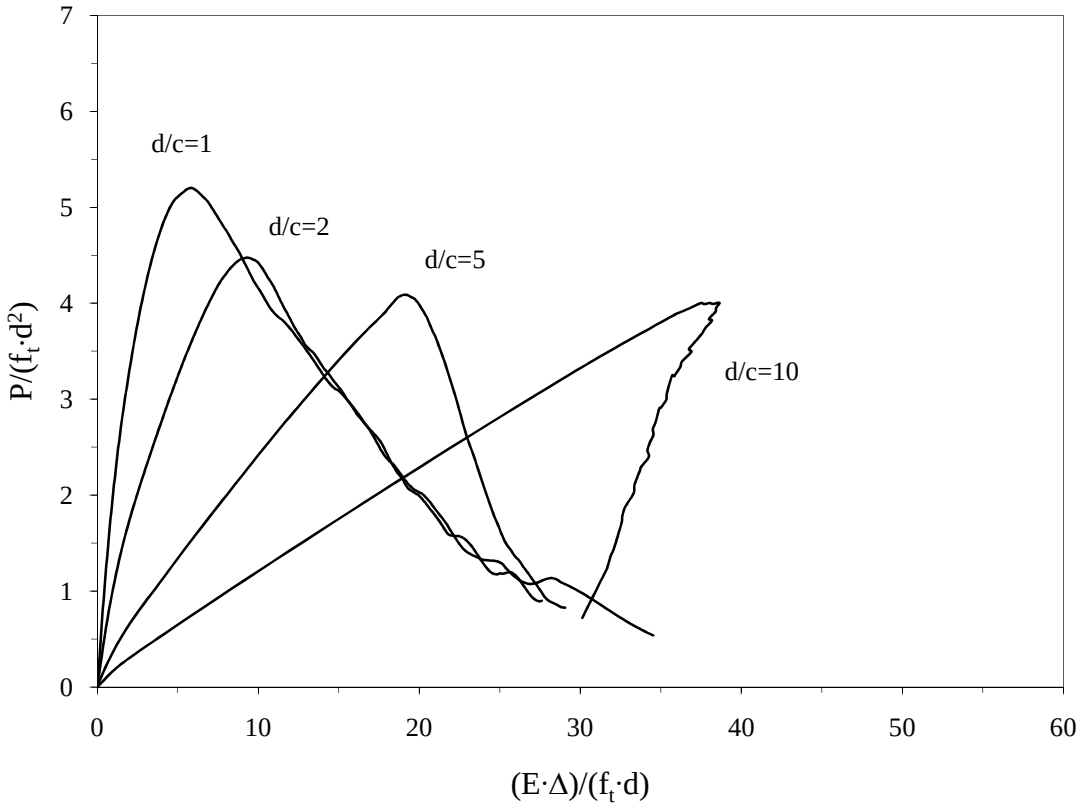

Fig. 2.5 – Load-displacement plots for unstressed concrete and $\beta = 0.5$

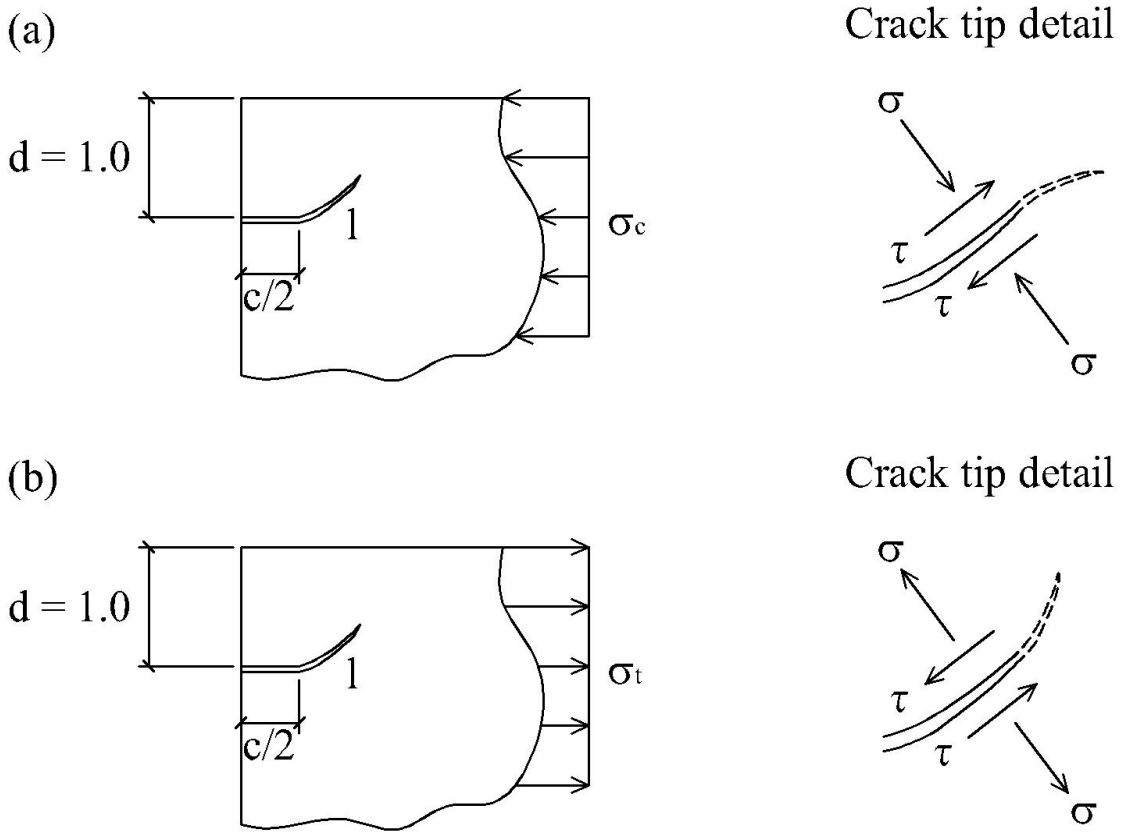

Fig. 2.6 – Close up view of the crack front for concrete matrix (a) under compression; (b) under tension

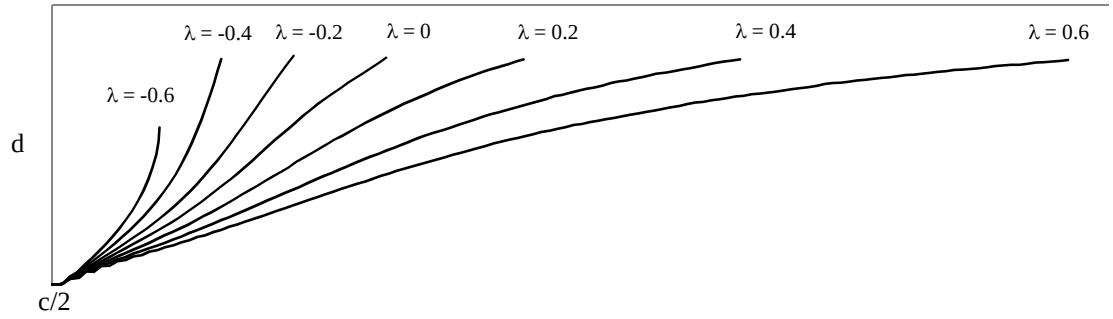

Fig. 2.7 – Crack paths as function of the applied stress ($\beta = 6.25$ and $d/c = 10$)

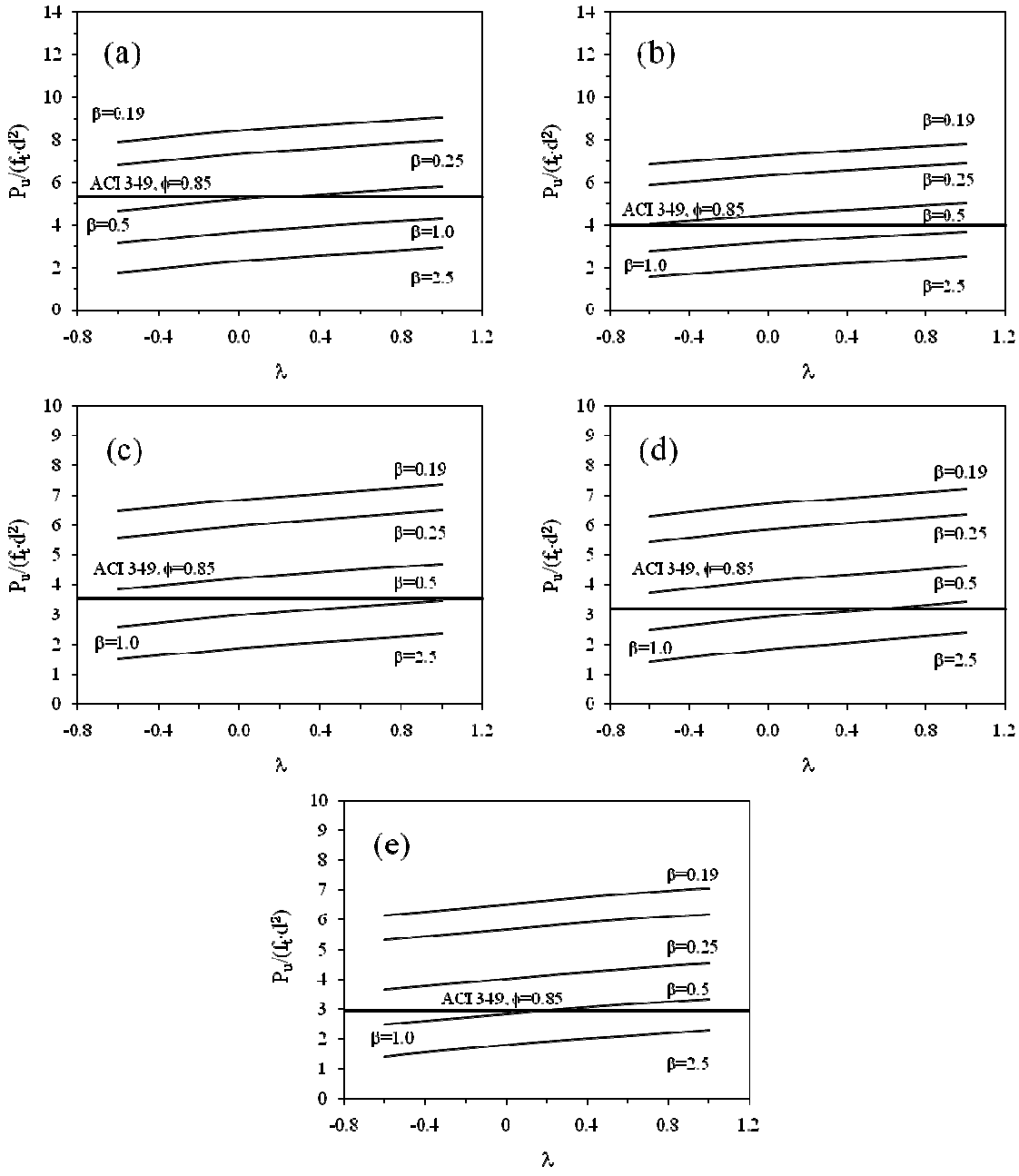

Fig. 2.8 – Ultimate dimensionless pullout load as functions of stress; (a) $d/c=1$; (b) $d/c=2$; (c) $d/c=3$; (d) $d/c=5$; (e) $d/c=10$

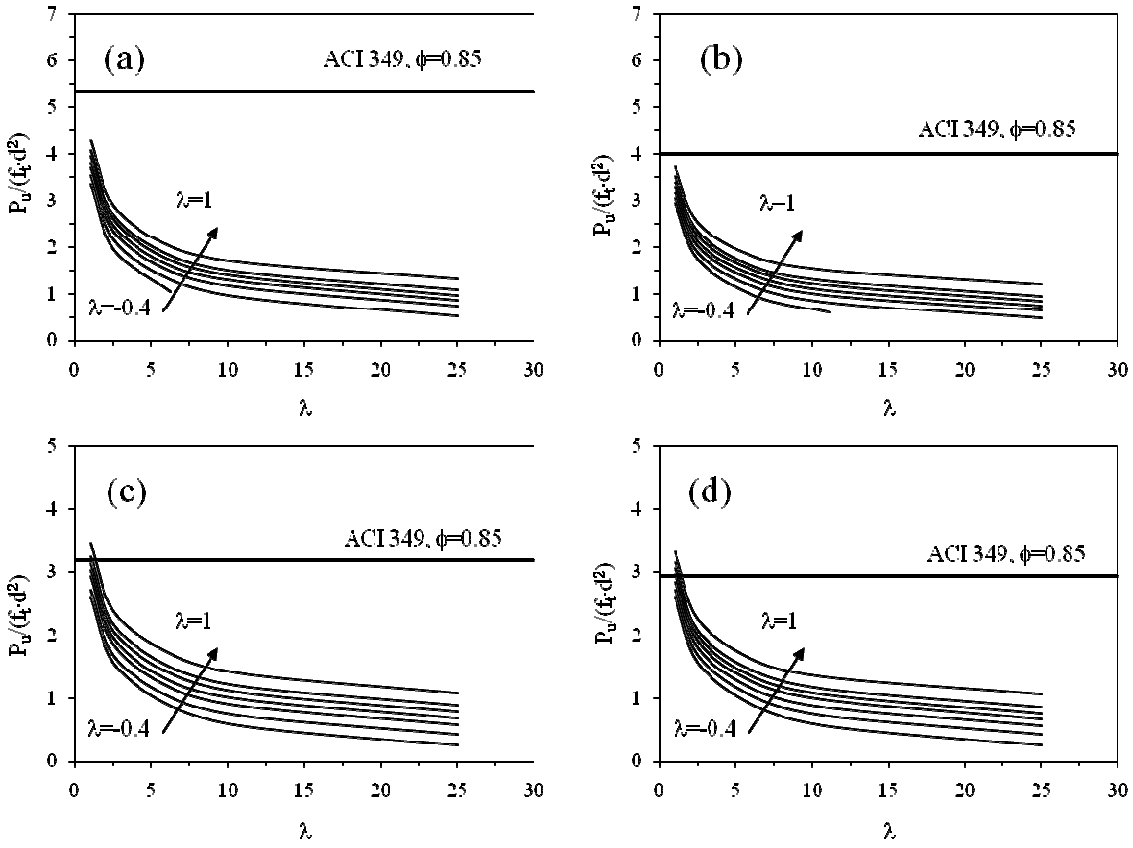

Fig. 2.9 – Ultimate dimensionless pullout load as functions of brittleness; (a) $d/c=1$; (b) $d/c=2$; (c) $d/c=5$; (d) $d/c=10$

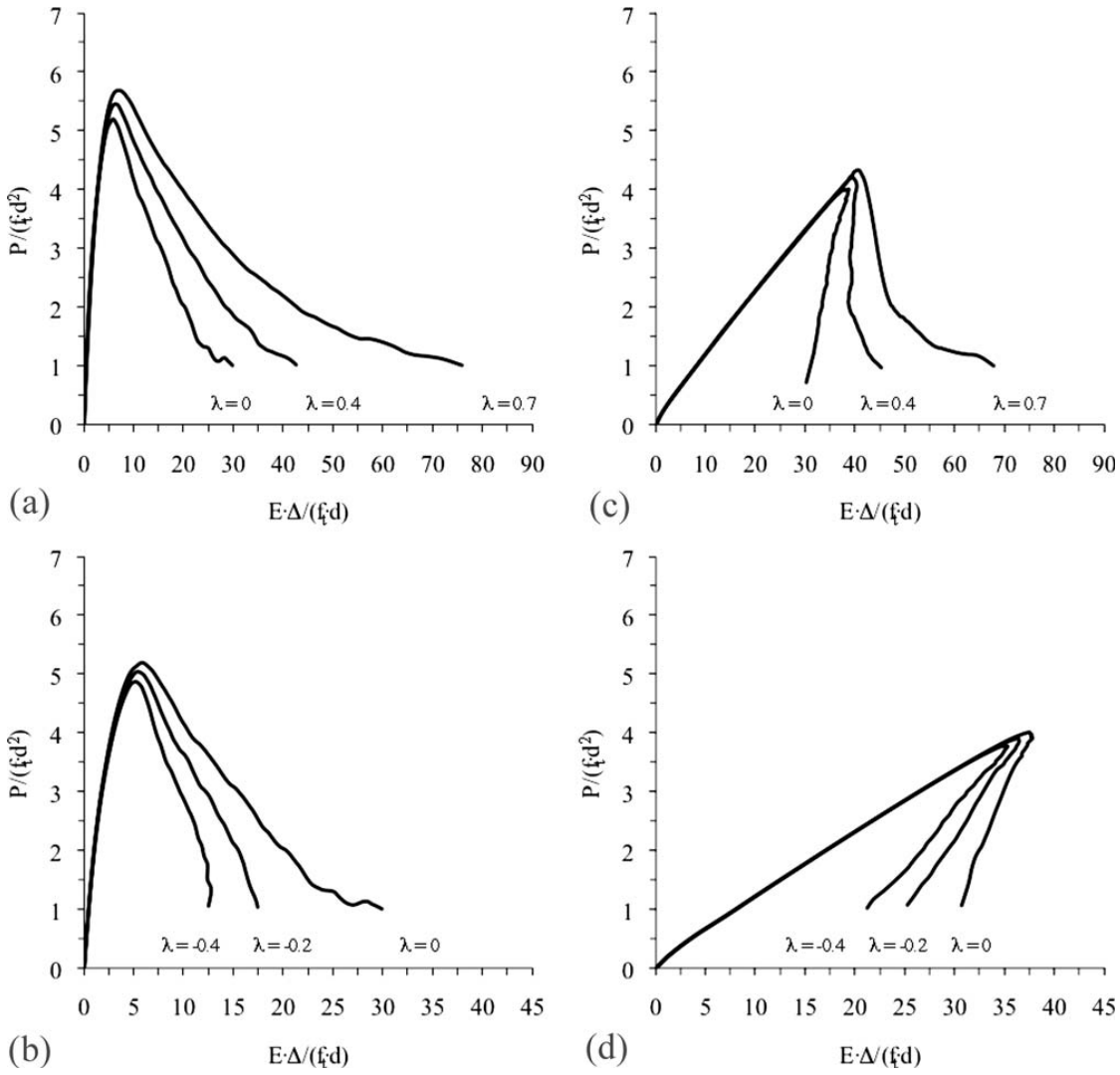

Fig. 2.10 – Load-displacement plots for values of $\lambda = 0$, $\lambda = 0.4$, $\lambda = 0.7$, $\lambda = -0.2$, $\lambda = -0.4$, $\beta = 0.5$, and $d/c = 1$

CHAPTER 3

EXPERIMENTAL PROGRAM, PART I

In this section the procedures and the experimental setup used to assess the predictions of the LEFM numerical simulations are described. In the first series of experiments, axi-symmetric pullout tests were performed using normal strength concrete as a matrix material. The aim of the investigation was to determine the effects of compressive prestress on the ultimate load carrying capacity of headed anchors and their load versus displacement behavior, therefore, only the embedment depths and the biaxial compression were changed. The first set of experiments was performed by varying the biaxial compression between zero (unconfined specimens, $\lambda = 0$) and a value approximately equal to the tensile strength of the concrete ($\lambda \approx 0.94$). The anchor embedment depth was varied to investigate its correlation with the ultimate load carrying capacity and the overall behavior of the system. Specifically, normalized embedment depths equal to $d/c = 1$ and $d/c = 2$ were investigated. In addition to the pullout tests, a laser scanner system was employed to determine the shape of the pullout failure cones and the relative fracture profiles.

3.1 Materials, Mix Proportions and Procedures

3.1.1 Concrete

The mix-components of the concrete were a Portland cement CEM I 52.5 R, according to ENV 197/1 European Standard, and a natural river aggregate (maximum

size of 25 mm). No super plasticizers were added. The concrete had an aggregate/cement ratio of 6.24 and a water/cement ratio of 0.7. The compressive strength of the mix was obtained from compression tests performed on cylinders with a diameter of 3.94 in. [100 mm] and a height of 7.87 in. [200 mm] and on cubes with a 5.9 in. [150 mm] side. The compression tests were completed between 21 and 35 days after the specimens were cast. The concrete properties were recorded and then averaged. Standard size cylinders (ASTM C31 [45] and C496/C496M [46]) were tested to obtain the Young's modulus and the uniaxial tensile strength of the material (Brazilian splitting test). After averaging, the obtained values were 3,408 ksi [23,500 MPa] and 417 psi [2.88 MPa], respectively. The mixture design and the averaged concrete properties at the time of the tests are reported in Table 3.1.

The specimens consisted of concrete blocks with the following dimensions: 39.37 x 39.37 x 7.87 in. [1 x 1 x 0.2 m] for "Type A", and 49.21 x 61.02 x 9.45 in [1.25 x 1.55 x 0.24 m] for "Type B". The larger specimens were cast to accommodate anchors with larger embedment depths. Four hooks were positioned at the corners to allow for the handling of the specimens.

3.1.2 Steel Headed Anchors

The concrete anchors had a stem diameter of 0.5 in. [12.7 mm] and a head diameter between 0.98 and 1 in. [25 to 25.4 mm]. They had an ultimate strength of 65 ksi [450 MPa] and a yield strength of 51 ksi [350 MPa]. The anchors were cast into the concrete specimens in a single cast. Wood formworks were used as a support for the

anchors during the casting process so that they could easily be positioned at different embedment depths (Fig. 3.1).

Four anchors were placed on the four corners of the each concrete specimen. Since the objective of the investigation was to determine the breakout capacity of the inserts and their load versus displacement behavior, their spacing and set up was chosen to avoid any interaction among the anchors, any free edge effects and, in turn, any undesired mode of failure (i.e., splitting, concrete blow-out, etc.). For "Type A" blocks, where only shallow anchors were cast, the anchor-to-anchor distance was equal to about 15.75 in. [40 cm] and the edge-to-anchor distance was equal to 11.81 in. [30 cm] in all directions. For "Type B" blocks, the anchor-to-anchor and the edge-to-anchor distances are shown in Fig. 3.2.

In the tests, two different nominal embedment depths were employed: 0.98 and 1.97 in. [25 and 50 mm]. These values were chosen to obtain embedment depth vs. head diameter ratios (namely, d/c) equal to 1 and 2, respectively. An additional embedment depth of 4.9 in. [125 mm] was only preliminarily considered. However, after a few tests, it was determined that the embedment depth was too large to avoid steel failure for the chosen anchors.

Due to the vibrating process and to settlements during the concrete curing process, the values of the embedment depths at the time of the tests were slightly different. Their measured values are reported in Table 3.2, where they are also compared to the nominal values.

3.2 Testing Apparatus for Pullout Tests

A representation of the testing machine employed in the pullout tests is shown in Fig. 3.3. The pullout load was applied by means of a hydraulic jack connected to a reaction frame. The reaction frame consisted of a steel structure, with the section shown in Fig. 3.3. The load was applied through a steel rod connected to the reaction frame at the top and to a special device that connected the anchor at the end.

The tests were load controlled and the relative displacements between the anchors and the upper surface of the concrete blocks were monitored by two LVDTs (±0.2 in. [±5 mm]) symmetrically positioned at a distance of 10.4 in. [264.2 mm] for short embedment depths and 15.2 in. [385 mm] for larger embedment depths from the axis of the anchor (Figs. 3.3 and 3.4). In all cases, all the data (load and displacement) were acquired with a data acquisition system.

The effect of confinement was simulated by applying bi-axial compression along the sides of the concrete specimens, in the directions orthogonal to the axis of the anchor. As shown in Figs. 3.5, the compression was applied by means of horizontally oriented hydraulic jacks inserted in a specially-built reaction frame.

The steel beams used to build the reaction frame were tied together in the two plane directions by using six special Diwidag tying bars. On the two sides of the specimens where the hydraulic jacks were acting, two additional steel beams were used to uniformly distribute the horizontal pressure. The opposite sides of the specimens were loaded by contrast through the reaction frame. To allow for a more uniform load distribution, a 0.4 in. [10 mm] layer of rubber was positioned between the specimens and the frame. While for “Type A” specimens one hydraulic jack per side was enough to

reach relatively high levels of confinement (Fig. 3.5), multiple hydraulic jacks per side (two) were needed to apply confinement for the “Type B” specimens (Fig. 3.5).

The pull-out tests were first performed in unconfined concrete for each embedment depth. Bi-axial compression was subsequently considered. The tests in confined concrete were performed considering three different amounts of compression: 5%, 7.5%, and 10% of the cylindrical compressive strength of the concrete measured at 21 days (3.9 ksi [26.9 MPa]). That is, 0.19 ksi [1.34 MPa], 0.29 ksi [2.02 MPa], and 0.39 ksi [2.69 MPa], respectively (details of the amount of force and relative stress applied to each specimen are shown in Table 3.2). The applied compression was constantly monitored before and after each pull-out test with standard manometers.

3.3 Testing Apparatus for Crack Profiles

A representation of the laser scanning machine used to detect the shape of the concrete cones obtained from the experimental investigation is shown in Fig. 3.6.

The system is composed of a laser scanner tool connected to an acquisition computer for the storage of the data. The laser is mounted on a horizontal steel guide member. This, in turn, is pinned down to a vertical guide. At the base of the vertical guide, a steel pedestal allows for the stability of the system. This assemblage allows movement and transportation of the laser in any suitable location. The laser can move in the horizontal and vertical directions according to the limits imposed by the two guides of a frame. The total in-plane area of action of the laser is represented by a square about 20 in. [500 mm] sided. The out of plane distance of a given object can be scanned only for a limited distance from the laser (about 1 to 1.5 in. [25.4 to 38 mm])

Complete crack profiles and cone shapes were successfully obtained for the anchors with smaller embedment depths ($d/c=1$). The limited range of action of the laser did not allow the measurements of the fracture cones with larger embedment depth. Despite the limits of the system, the procedure was considered very important in that the crack propagation angle of the shallower cones and the axial-symmetry of the failure surfaces were investigated.

3.4 Results

A total of 27 tests were performed in the first part of the experimental program. The variables in the tests were the embedment depth of the anchors, d, and the amount of bi-axial compression applied orthogonally to the axis of the anchors, σ_c. In this section, the experimental results are illustrated and discussed.

The results are shown in non-dimensional form. The normalization of the investigated variables involved the embedment depth of the anchors, d, the Young's modulus of the concrete (E =3,408 ksi [23,500 MPa]) and its tensile strength obtained from the Brazilian splitting test (f_t =417 psi [2.88 MPa]). Table 3.2 schematically shows the variables involved in each pullout test and the test setup.

It is noted that the normalization process involved the values of the effective embedment depths, d, reported in Table 3.2.

3.4.1 Load Carrying Capacity

The experimentally measured ultimate capacity data for unstressed and prestressed concrete are reported in Table 3.3. The failure mode (C for concrete cone

failure, S for yielding and rupture of the steel) is also reported. Figures 3.7a-b illustrate the dependence of the ultimate capacities on the applied prestress. Dimensional plots and values are reported in Appendix B.

It is observed that for the investigated embedment depths ($d/c = 1$ and $d/c = 2$) the capacity increases linearly with the applied prestress. Because of the lack of a design formula for prestressed concrete, a comparison with the actual ACI 318 Code provision and the ACI 349-89 formula could be approached only for the unconfined case ($\lambda = 0$). Fig. 3.8, where the experimental evidence is compared to the available predictions in a log-log scale plot, provides valuable information (The plotted predicted and experimentally obtained capacities are divided, as it is was done in Ozbolt *et al.* [23], by the area of a circle with radius equal to the embedment depth). First, for the embedment depths investigated, it is shown that the LEFM based prediction (CCD method) is quite accurate while the ACI 349-89 [5] equation represents a lower bound to the experimental data. Second, when compared to the case where no size effect is taken into account, the fact that the experimental results agree with the LEFM approach means that the size effect on the nominal pull-out strength is very strong.

3.4.2 Load versus Displacement Behavior

As part of the experimental investigation, load versus displacement curves were obtained for each pullout test. The displacement was monitored by two LVDTs positioned symmetrically with respect to the axis of the anchor. The distance between the LVDTs was larger for the pullout tests with $d/c = 2$. This choice was justified by the fact that the LVDTs should measure the displacements of the bolt with respect to the

uncracked concrete surface, and, in turn, avoid any contact with the conical failure surface. With respect to the axis of the anchor, the LVDTs were positioned at a distance of 10.4 in. [264.2 mm] for $d/c = 1$ and 15.2 in. [385 mm] for $d/c = 2$.

The experimentally measured load versus displacement curves for unstressed and prestressed concrete are included in Appendix B. The ultimate capacity and the displacement were normalized using the measured uniaxial tensile strength, f_t, (417 psi [2.88 MPa]) of the material, the measured Young's modulus, E, (3408 ksi [23500 MPa]), and nominal values of d =0.98 in. [24.89 mm] for $d/c = 1$ and d =1.96 in. [49.78 mm] for $d/c = 2$.

As explained in Chapter 2, the effects of prestress and tensile stresses on ductility were quantified using the work of fracture, *WOF*, defined as the area under the force-displacement curve. The load-point displacement, Δ, in the simulations was defined as the relative displacement between the top and the bottom surfaces of the discontinuity defining the anchor (Fig. 2.2). This displacement could not be measured in the experiments. Instead the displacement was measured by the two LVDTs positioned symmetrically with respect to the axis of the anchor (Fig. 3.4). In the subsequent discussion the comparison between the simulated and experimentally measured *WOF* is therefore qualitative.

Even though based on different definitions of the load point displacement, Δ, the load versus displacement experimental curves (Appendix B) provide valuable insights. When a confining prestress is applied the increase in dissipated energy in the post peak is large, while the increase in ultimate load is modest. This increase is the result of the significant increase in the length of crack propagation.

3.4.3 Fracture Cones and Crack Profiles

The fracture cone profiles for the specimens with embedment depth $d/c=1$ could be obtained using a laser scanner. The three dimensional fracture surfaces of selected concrete cones obtained by elaborating the acquired data are shown in Appendix B.

Two dimensional crack profiles were obtained by dividing the three dimensional surfaces in a series of straight lines passing through the head of the anchor. The results obtained for each concrete cone by this numerical procedure are shown in Appendix B.

Figs. 3.9a-d show the experimentally measured fracture profile envelopes for different levels of prestress. In the unconfined case, the fracture process starts from the edge of the anchor's head with an angle comprised between 20 and 55 degrees with respect to the horizontal free surface (Fig. 3.9a). When $\lambda=0.47$ (Fig. 3.9b), the fracture propagation angle decreases to values between 15 and 33 degrees. For a larger value of prestress ($\lambda=0.7$) the fracture propagation angle is further reduced and comprised between 10 and 30 degrees with respect to the horizontal line (Fig. 3.9c). For the highest prestress investigated ($\lambda=0.94$), the propagation angle is between 20 and 55 degrees, as observed for the unconfined case (Fig. 3.9d). In all the cases, the fracture angle steers horizontally at a depth equal to about 30% of the anchor's embedment depth. Beyond this point, the crack profiles follow a path inclined about 8 to 10 degrees with respect to the free surface (disc action, that is). The above observations reflect the analytical and numerical observations according to which, when a compressive stress is applied to the concrete matrix, the algebraic value of the mode II stress intensity factor at the

propagating crack front increases, steering the crack towards the direction of the applied stress.

Because of the limited range of action of the laser scanner, the fracture profiles for the specimens with embedment depth $d/c = 2$ could not be obtained. However, by visual inspection (Fig. 3.10), the same propagation direction and behavior as for the $d/c = 1$ case were observed (A more detailed visual inspection procedure was carried out in the second part of the experiments, discussed next).

The measured fracture propagation angles were also compared to the available predictions for the unstressed case. In the CCD method, the angle of propagation is assumed to be equal to 35 degrees with respect to the horizontal line, while according to the ACI 349-89 approach the angle should be considered equal to 45 degrees. In this experimental study, the angle of propagation is comprised between 20 and 55 degrees, which falls in the typical range of values assumed by the available formulas.

Table 3.1 – Experimental Part I: Material Properties [Units in ksi (MPa)]

Material	Property	Value
Concrete	28 days cylinder strength	4.73 (32.59)
	28 days cubic strength	5.26 (36.30)
	21 days cylinder strength	3.90 (26.90)
	21 days cubic strength	4.70 (32.40)
	Tensile strength, f_t	0.42 (2.88)
	Young's modulus	3,408 (23,500)
Steel	Yield strength, 0.2% offset, f_y	51 (350)
	Ultimate strength, f_u	65 (450)

Table 3.2 – Experimental Investigation Details and Parameters

Test	Nominal embedment depth, in. (mm)	Effective embedment depth, in. (mm)	Head diameter, in. (mm)	Max confinement, kip (kN)	Confining pressure, σ_c, ksi (MPa)
1	1.97 (50)	2.12 (53.85)	0.98 (25)	0 (0)	0 (0)
2	1.97 (50)	1.97 (50.04)	0.98 (25)	0 (0)	0 (0)
3	4.92 (125)	4.92 (125)	0.98 (25)	0 (0)	0 (0)
4	4.92 (125)	4.92 (125)	0.98 (25)	0 (0)	0 (0)
5	4.92 (125)	4.92 (125)	0.98 (25)	0 (0)	0 (0)
6	1.97 (50)	2.06 (52.32)	0.98 (25)	0 (0)	0 (0)
7	1.97 (50)	1.88 (47.75)	0.98 (25)	0 (0)	0 (0)
8	0.98 (25)	0.93 (23.62)	0.98 (25)	0 (0)	0 (0)
9	0.98 (25)	0.97 (24.64)	0.98 (25)	0 (0)	0 (0)
10	0.98 (25)	0.96 (24.38)	0.98 (25)	0 (0)	0 (0)
11	0.98 (25)	0.91 (23.11)	0.98 (25)	0 (0)	0 (0)
12	0.98 (25)	1.07 (27.18)	0.98 (25)	62 (276)	0.20 (1.34)
13	0.98 (25)	0.98 (24.89)	0.98 (25)	121 (538)	0.39 (2.69)
14	0.98 (25)	1.04 (26.42)	0.98 (25)	121 (538)	0.39 (2.69)
15	0.98 (25)	1.03 (26.16)	0.98 (25)	62 (276)	0.20 (1.34)
16	0.98 (25)	1.23 (31.24)	0.98 (25)	62 (276)	0.20 (1.34)
17	0.98 (25)	0.94 (23.88)	0.98 (25)	121 (538)	0.39 (2.69)
18	0.98 (25)	1.06 (26.92)	0.98 (25)	90 (400)	0.29 (2.02)
19	0.98 (25)	1.03 (26.16)	0.98 (25)	90 (400)	0.29 (2.02)
20	1.97 (50)	1.95 (49.53)	0.98 (25)	115 (512)	0.20 (1.34)
21	1.97 (50)	2.00 (50.80)	0.98 (25)	115 (512)	0.20 (1.34)
22	1.97 (50)	2.19 (55.63)	0.98 (25)	225 (1000)	0.39 (2.69)
23	1.97 (50)	1.92 (48.77)	0.98 (25)	225 (1000)	0.39 (2.69)
24	1.97 (50)	1.97 (50.04)	0.98 (25)	167 (743)	0.29 (2.02)
25	1.97 (50)	1.91 (48.51)	0.98 (25)	167 (743)	0.29 (2.02)
26	1.97 (50)	1.93 (49.02)	0.98 (25)	115 (512)	0.20 (1.34)
27	1.97 (50)	2.06 (52.32)	0.98 (25)	167 (743)	0.29 (2.02)

Table 3.3 – Ultimate Load and Failure Mode

Test	Failure mode	Ultimate load, kips (kN)
1	C	6.62 (29.43)
2	C	6.17 (27.45)
3	S	N/A
4	S	N/A
5	S	N/A
6	C	6.33 (28.17)
7	C	5.82 (25.89)
8	C	2.35 (10.45)
9	C	2.41 (10.74)
10	C	2.14 (9.53)
11	C	2.29 (10.19)
12	C	3.13 (13.92)
13	C	2.25 (10.01)
14	C	2.34 (10.40)
15	C	2.58 (11.49)
16	C	3.94 (17.53)
17	C	2.52 (11.21)
18	C	3.48 (15.50)
19	C	3.49 (15.53)
20	C	6.25 (27.80)
21	C	6.61 (29.39)
22	C	8.96 (39.88)
23	C	7.82 (34.77)
24	C	6.32 (28.10)
25	C	6.83 (30.38)
26	C	8.55 (38.01)
27	C	8.27 (36.77)

Fig. 3.1 – Headed anchors positions before casting the concrete matrix. Detail of the steel molds and the wood formworks used to support the anchors at a given embedment depth.

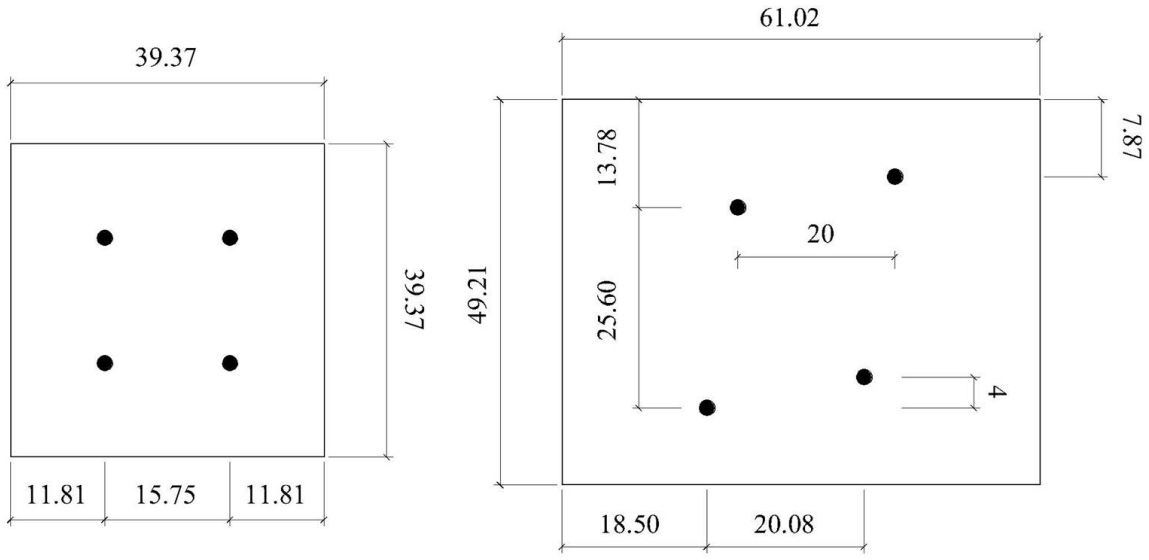

Fig. 3.2 – Position of the headed anchors according to their embedment depth (“Type A” specimen, left, and “Type B” specimen, right); measures in inches.

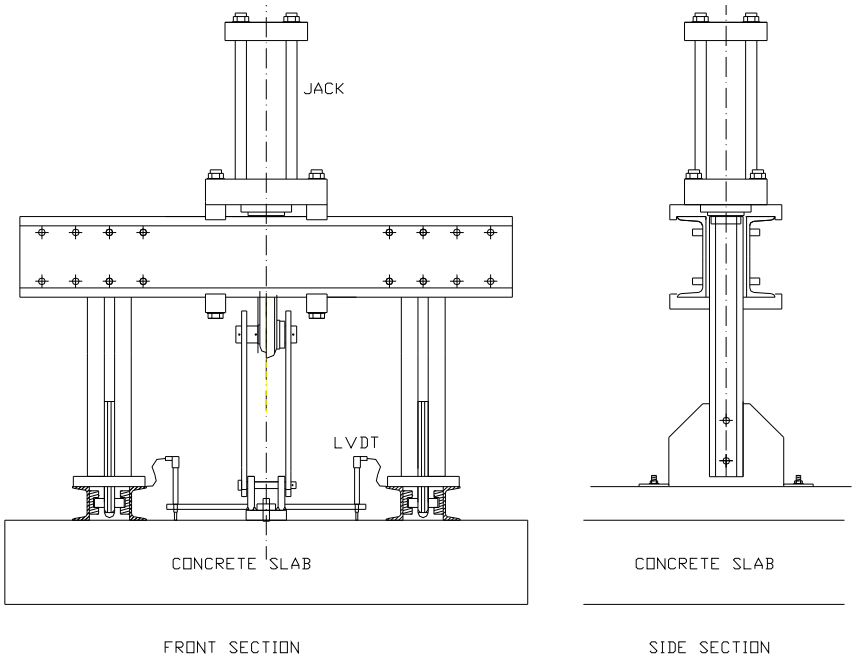

Fig. 3.3 – Testing machine used for the pullout experiments (front and side views) and location of the LVDTs

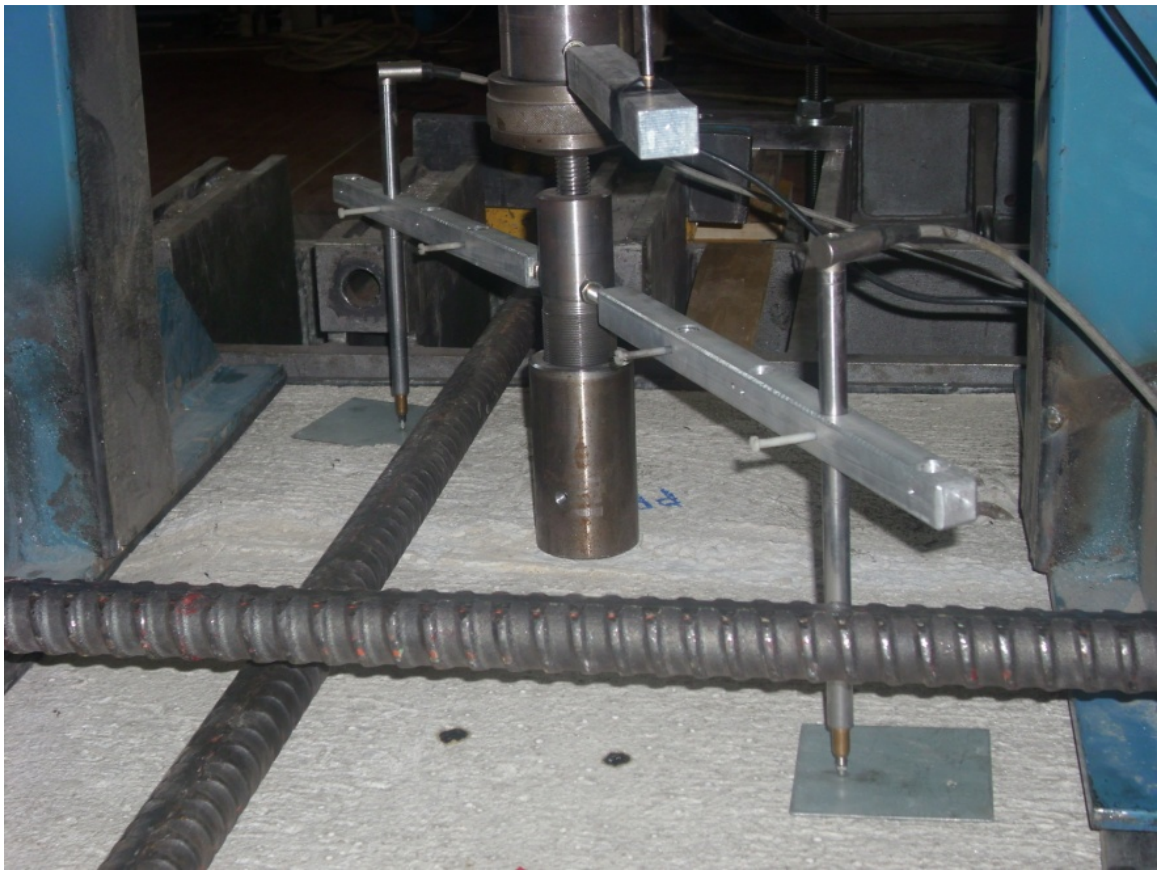

Fig. 3.4 – Position of the LVDTs during anchor's extraction

Fig. 3.5 – Built-in frame for the application of compressive prestress with two hydraulic jacks per side. Different stages of constructions (Clockwise, from top left): preparation of frame without concrete plate; frame with “Type A” specimen; frame with “Type B specimen; frame with “Type B” specimen and extracting machine.

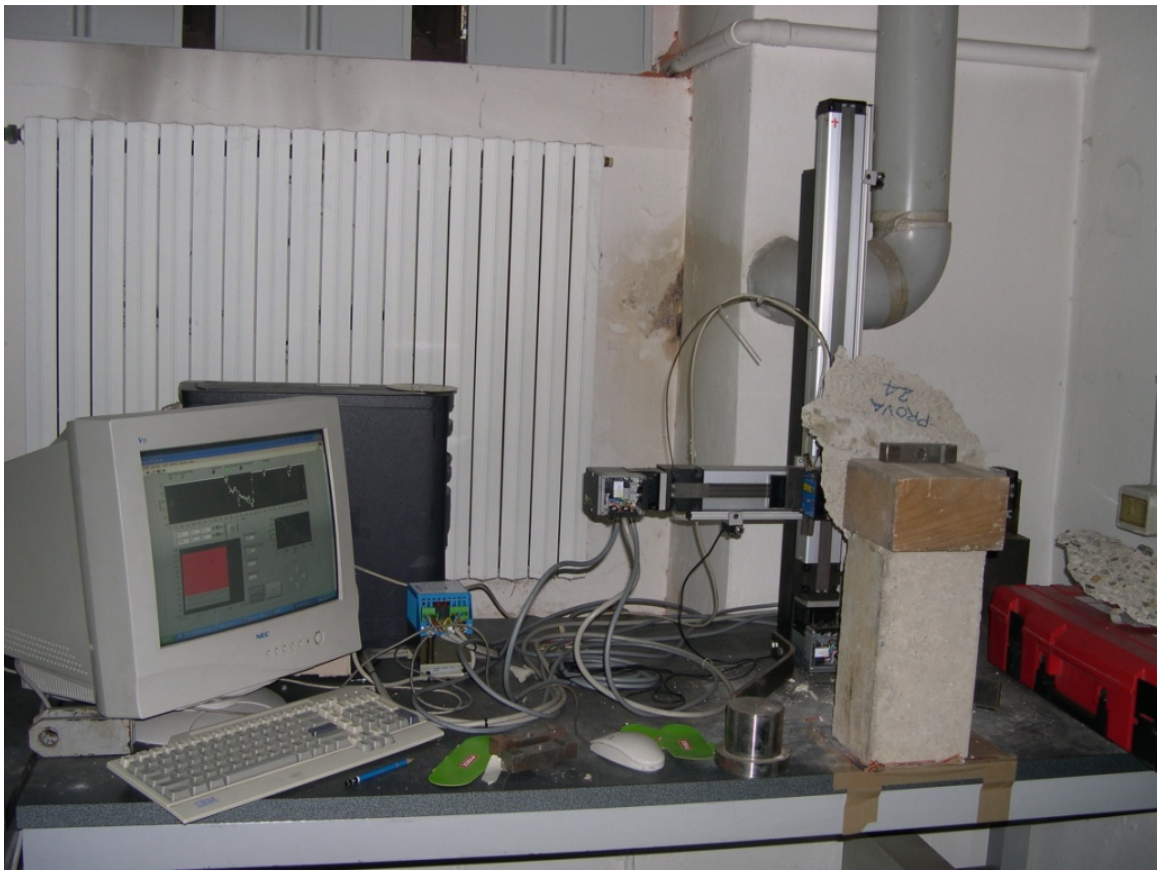

Fig. 3.6 – Testing apparatus for crack profiles (laser, frame, and data acquisition system)

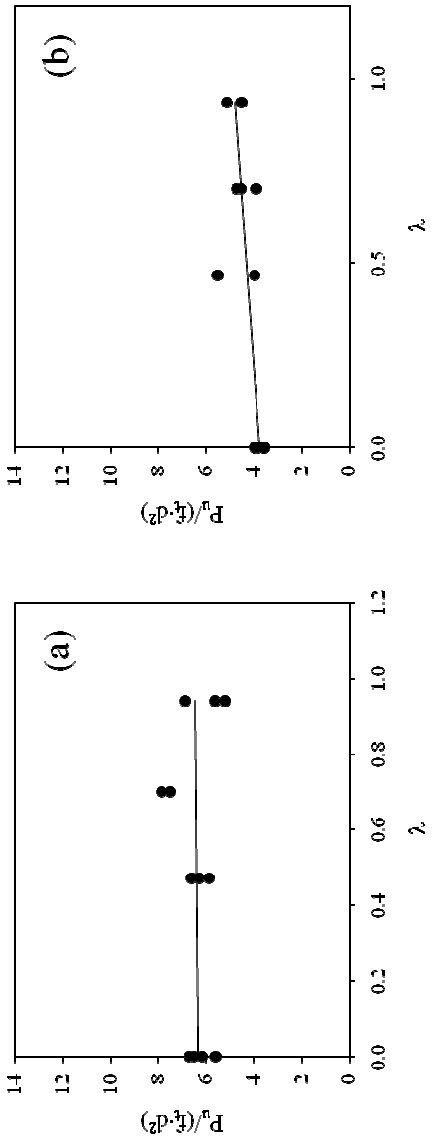

Fig. 3.7 – Normalized ultimate load carrying capacity as function of prestress; (a) $d/c = 1$; (b) $d/c = 2$

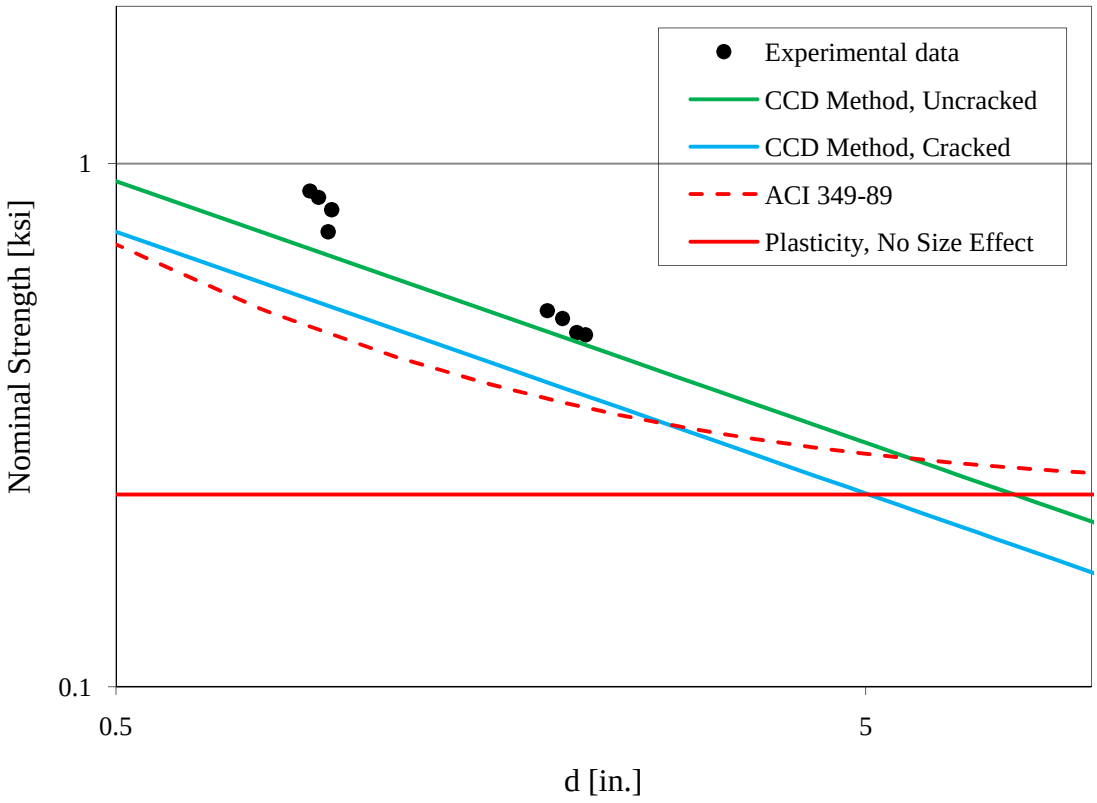

Fig. 3.8 – Log-log plot of nominal pullout strength as a function of the embedment depth for the embedment depths investigated; $\lambda = 0$

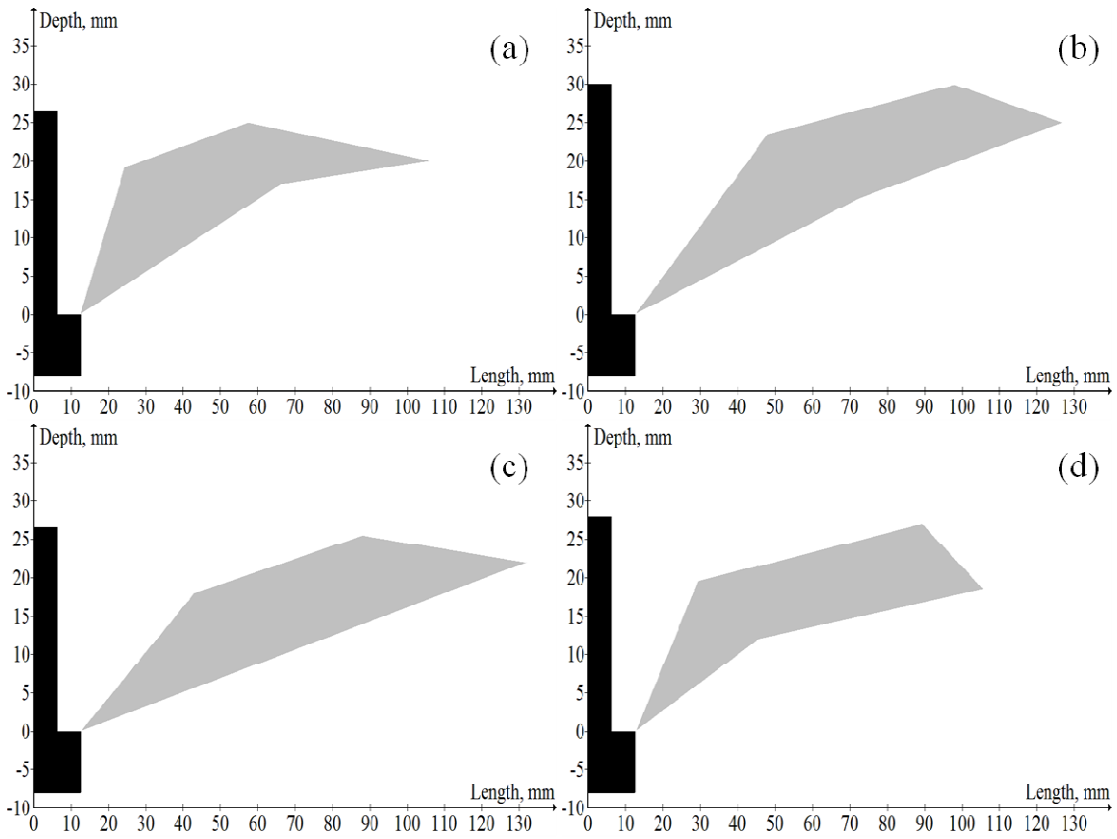

Fig. 3.9 – Envelopes of crack profiles; $d/c = 1$ and (a) $\lambda = 0$; (b) $\lambda = 0.47$; (c) $\lambda = 0.7$; (d) $\lambda = 0.94$

Fig. 3.10 – Crack profiles; $d/c = 2$ and (a) $\lambda = 0$; (b) $\lambda = 0.94$;

CHAPTER 4

EXPERIMENTAL PROGRAM, PART II

In order to reach larger values of prestress ($\lambda \approx 1.25$) and observe the behavior of headed anchors embedded at larger embedment depths ($d/c \approx 3$) a second series of pullout tests were performed using a relatively low strength concrete as a matrix material. The anchor embedment depth was varied to investigate its correlation with the ultimate load carrying capacity and the overall behavior of the system. Specifically, normalized embedment depths equal to $d/c = 0.75$, $d/c = 2$, and $d/c = 2.75$ were investigated.

4.1 Materials, Mix Proportions and Procedures

4.1.1 Concrete

The mix-components of the concrete were a Portland cement CEM I 52.5 R, according to ENV 197/1 European Standard, and a natural river aggregate (maximum size of 25 mm). No super plasticizers were added. The concrete had an aggregate/cement ratio of 6.24 and a water/cement ratio of 0.7. The compressive strength of the mix was obtained from compression tests performed on cubes with a 5.9 in. [150 mm] side. The compression tests were completed between 28 and 35 days after the specimens were cast. The concrete properties were recorded and then averaged. Standard size cylinders were tested to obtain the uniaxial tensile strength of the material (Brazilian splitting test). After averaging, a value of about 412 psi was obtained for the concrete uniaxial tensile strength, f_t. The Young's modulus of the material, E, was obtained from available

standard design formulas ($E = 57{,}000 \cdot \sqrt{f'_c}$, psi). The mixture design and the averaged concrete properties at the time of the tests are reported in Table 4.1.

The specimens consisted of concrete blocks with the following dimensions: 39.37 x 39.37 x 7.87 in. [1 x 1 x 0.2 m]. To allow the application of larger confining pressures, these dimensions were kept constant, independently of the embedment depth to investigate. Four hooks were positioned at the corners to allow for the handling of the specimens.

4.1.2 Steel Headed Anchors

The concrete anchors had a stem diameter of 0.5 in. [12.7 mm] and a head diameter between 0.98 and 1 in. [25 to 25.4 mm]. They had an ultimate strength of 65 ksi [450 MPa] and a yield characteristic strength of 51 ksi [350 MPa]. The anchors were cast into the concrete specimens in a single cast. As for the first experimental part, wood formworks were used as a support for the anchors during the casting process so that they could easily be positioned at different embedment depths.

In the tests, three different nominal embedment depths were employed: 0.71, 1.97, and 2.7 in. [18, 50, and 69 mm]. These values were preliminary chosen to obtain embedment depth vs. head diameter ratios (namely, d/c) equal to 0.75, 2, and 2.75, respectively.

Due to the vibrating process and to settlements during the concrete curing process, the values of the embedment depths at the time of the tests were slightly different. Their measured (effective) values are reported in Table 4.2, where they are also compared to the nominal values.

Four anchors were placed on the four corners of the each concrete specimen. Similarly to the first experimental set up, and based upon each anchor embedment depth, different edge-to-anchor and anchor-to-anchor distances were considered. For "Type C" blocks, where only shallow anchors were cast ($d/c = 0.75$), the anchor-to-anchor distance was equal to about 9.84 in. [25 cm] and the edge-to-anchor distance was equal to 9.84 in. [25 cm] in all directions. For "Type D" blocks, where only anchors with $d/c = 2$ were cast, the anchor-to-anchor and the edge-to-anchor distances were, again, equal to 9.84 in. [25 cm]. For "Type E" blocks, were anchors with $d/c = 0.75$ and $d/c = 2.75$ were cast simultaneously, the distances are shown in Fig. 4.1.

4.2 Testing Apparatus for Pullout Tests

The second part of the experimental program was carried out using the same testing machine and methodology described in Chapter 3.

4.3 Results

A total of 40 tests were performed in the second part of the experimental program. The variables in the tests were the embedment depth of the anchors, d, and the amount of bi-axial compression applied orthogonally to the axis of the anchors, σ_c. In this section, the experimental results are illustrated and discussed.

The results are shown in non-dimensional form. The normalization of the investigated variables involved the embedment depth of the anchors, d, the Young's modulus of the concrete (E =3,300 ksi [22,750 MPa]) and its tensile strength obtained

from the Brazilian splitting test (f_t =412 psi [2.84 MPa]). Table 4.2 schematically shows the variables involved in each pullout test and the test setup.

It is noted that the normalization process involved the values of the effective embedment depths, d, reported in Table 4.2. In fact, nominal embedment depths were difficult to achieve because some relaxation and settling movements of the anchors from the original position had occurred during the casting process of the concrete and the curing period.

4.3.1 Load Carrying Capacity

The experimentally measured ultimate capacity data for unstressed and prestressed concrete are reported in Table 4.3. The failure mode (C for concrete cone failure, S for yielding and rupture of the steel) is also reported. Figures 4.2a-c illustrate the dependence of the ultimate capacities on the applied prestress. Dimensional plots and values are reported in Appendix B.

As it was already shown in the first part of the experimental program, for the investigated embedment depths $d/c = 2$ and $d/c = 2.75$, the capacity increases linearly with the applied prestress. In the $d/c = 0.75$ case, however, the capacity does not increase with the prestress but seems to decrease. This result suggests that for very shallow anchors, other factors should be taken into account. First, the anchors are placed extremely close to the concrete surface and the assumptions of gradual transition and homogeneity of the material that are fundamental for the validity of a continuum-based approach are not correct. Second, the presence of aggregates and concrete in a very small, localized area between the head of the anchor and the free surface seem to suggest that

the microstructure of the embedding material might become an extremely important parameter to investigate. Finally, the presence of a steel member so close to the free surface might give rise to other phenomena together with the pullout failure, like high, quickly damaging stress concentrations and splitting failures. Some images of these anchors, illustrating the very shallow cone failure surfaces, are shown in Fig. 4.4.

A comparison with the ACI 318 Code provision and the obsolete ACI 349-89 formula could be approached only for the unconfined case ($\lambda = 0$). Fig. 4.3 compares the capacities predicted by the available design formulas and the capacities obtained from the experiments.

In a log-log scale, the experimental evidence is compared to the predictions based on LEFM (CCD method, cracked and uncracked concrete conditions) and plasticity (ACI 349-89 and plasticity without size effect). Once again, and except for $d/c = 0.75$, the experimental evidence agrees with the LEFM based design formulas showing that the size effect on the nominal pull-out strength is very strong.

4.3.2 Load versus Displacement Behavior

As part of the experimental investigation, load versus displacement curves were obtained for each pullout test. The displacement was monitored by two LVDTs positioned symmetrically with respect to the axis of the anchor. The distance between the LVDTs was larger for the larger embedment depths investigated.

The experimentally measured load versus displacement curves for unstressed and prestressed concrete are included in Appendix B. The ultimate capacity and the displacement were normalized using the measured uniaxial tensile strength, f_t, (412 psi

[2.84 MPa]) of the material, the Young's modulus, E, (3,300 ksi [22,750 MPa]), and nominal values of d=0.71 in. [18 mm] for $d/c = 0.75$, d=1.97 in. [50 mm] for $d/c = 2$, and d=2.70 in. [69 mm] for $d/c = 2.75$.

4.3.3 Fracture Cones and Crack Profiles

As it was previously described, crack propagation angles were experimentally determined by using a laser scanning machine. Because of the limited range of action of the laser, only crack profiles for the shallow anchors ($d/c = 1$) were obtained. To investigate the crack propagation angle and failure surfaces of the anchors embedded at $d/c = 2$, a very careful visual inspection was carried out.

By elaborating pictures of the specimens and by visually marking the crack profiles after rescaling them at real dimensions, the experimental crack patterns were obtained and are shown in Fig. 4.5. The same propagation directions and behavior as for the $d/c = 1$ case were observed.

Table 4.1 – Experimental Part II: Material Properties [Units in ksi (MPa)]

Material	Property	Value
Concrete	28 days cubic strength	4.05 (27.91)
	28 days cylinder strength	3.36 (23.17)
	Tensile strength, f_t	0.41 (2.84)
	Young's modulus	3,300 (22,750)
Steel	Yield strength, 0.2% offset, f_y	51 (350)
	Ultimate strength, f_u	65 (450)

Table 4.2 – Experimental Investigation Details and Parameters

Test	Nominal embedment depth, in. (mm)	Effective embedment depth, in. (mm)	Head diameter, in. (mm)	Max confinement, kip (kN)	Confining pressure, σ_c, ksi (MPa)
1	0.71 (18)	0.83 (21)	0.98 (25)	0 (0)	0 (0)
2	0.71 (18)	0.87 (22)	0.98 (25)	0 (0)	0 (0)
3	0.71 (18)	0.77 (20)	0.98 (25)	0 (0)	0 (0)
4	0.71 (18)	0.75 (19)	0.98 (25)	52 (232)	0.17 (1.16)
5	0.71 (18)	0.97 (25)	0.98 (25)	52 (232)	0.17 (1.16)
6	0.71 (18)	0.69 (18)	0.98 (25)	52 (232)	0.17 (1.16)
7	0.71 (18)	0.66 (17)	0.98 (25)	52 (232)	0.17 (1.16)
8	0.71 (18)	0.68 (17)	0.98 (25)	78 (347)	0.25 (1.74)
9	0.71 (18)	0.75 (19)	0.98 (25)	78 (347)	0.25 (1.74)
10	0.71 (18)	0.69 (18)	0.98 (25)	78 (347)	0.25 (1.74)
11	0.71 (18)	0.68 (17)	0.98 (25)	78 (347)	0.25 (1.74)
12	0.71 (18)	0.82 (21)	0.98 (25)	104 (463)	0.34 (2.32)
13	0.71 (18)	0.82 (21)	0.98 (25)	104 (463)	0.34 (2.32)
14	0.71 (18)	0.69 (18)	0.98 (25)	104 (463)	0.34 (2.32)
15	0.71 (18)	0.71 (18)	0.98 (25)	156 (695)	0.50 (3.47)
16	0.71 (18)	0.72 (18)	0.98 (25)	156 (695)	0.50 (3.47)
17	1.97 (50)	1.80 (46)	0.98 (25)	0 (0)	0 (0)
18	1.97 (50)	2.03 (52)	0.98 (25)	0 (0)	0 (0)
19	1.97 (50)	2.00 (51)	0.98 (25)	0 (0)	0 (0)
20	1.97 (50)	1.96 (50)	0.98 (25)	52 (232)	0.17 (1.16)
21	1.97 (50)	2.06 (52)	0.98 (25)	52 (232)	0.17 (1.16)
22	1.97 (50)	1.95 (50)	0.98 (25)	78 (347)	0.25 (1.74)
23	1.97 (50)	1.89 (48)	0.98 (25)	78 (347)	0.25 (1.74)
24	1.97 (50)	1.83 (46)	0.98 (25)	78 (347)	0.25 (1.74)
25	1.97 (50)	2.29 (58)	0.98 (25)	104 (463)	0.34 (2.32)
26	1.97 (50)	1.93 (49)	0.98 (25)	104 (463)	0.34 (2.32)
27	1.97 (50)	2.27 (58)	0.98 (25)	104 (463)	0.34 (2.32)
28	1.97 (50)	2.01 (51)	0.98 (25)	104 (463)	0.34 (2.32)
29	1.97 (50)	1.90 (48)	0.98 (25)	156 (695)	0.50 (3.47)
30	1.97 (50)	1.82 (46)	0.98 (25)	156 (695)	0.50 (3.47)
31	1.97 (50)	2.04 (52)	0.98 (25)	156 (695)	0.50 (3.47)
32	1.97 (50)	1.80 (46)	0.98 (25)	156 (695)	0.50 (3.47)
33	2.70 (69)	2.93 (74)	0.98 (25)	0 (0)	0 (0)
34	2.70 (69)	2.83 (72)	0.98 (25)	0 (0)	0 (0)
35	2.70 (69)	2.83 (72)	0.98 (25)	52 (232)	0.17 (1.16)

Test	Nominal embedment depth, in. (mm)	Effective embedment depth, in. (mm)	Head diameter, in. (mm)	Max confinement, kip (kN)	Confining pressure, σ_c, ksi (MPa)
36	2.70 (69)	2.60 (66)	0.98 (25)	52 (232)	0.17 (1.16)
37	2.70 (69)	2.62 (67)	0.98 (25)	78 (347)	0.25 (1.74)
38	2.70 (69)	2.60 (66)	0.98 (25)	78 (347)	0.25 (1.74)
39	2.70 (69)	2.62 (67)	0.98 (25)	78 (347)	0.25 (1.74)
40	2.70 (69)	2.62 (67)	0.98 (25)	104 (463)	0.34 (2.32)

Table 4.3 – Ultimate Load and Failure Mode

Test	Failure mode	Ultimate load, kips (kN)
1	C	1.06 (4.71)
2	C	1.44 (6.42)
3	S	1.01 (4.49)
4	S	0.76 (3.36)
5	S	2.10 (9.34)
6	C	1.24 (5.50)
7	C	0.65 (2.91)
8	C	0.90 (4.02)
9	C	1.17 (5.23)
10	C	1.40 (6.25)
11	C	0.86 (3.81)
12	C	1.02 (4.53)
13	C	0.95 (4.20)
14	C	1.13 (5.05)
15	C	0.72 (3.189)
16	C	0.69 (3.06)
17	C	4.77 (21.22)
18	C	5.26 (23.38)
19	C	5.08 (22.61)
20	C	5.35 (23.81)
21	C	4.80 (21.38)
22	C	4.83 (21.47)
23	C	5.27 (23.42)
24	C	4.87 (21.65)
25	C	7.51 (33.39)
26	C	5.12 (22.76)
27	C	7.55 (33.57)
28	C	6.24 (27.78)
29	C	4.85 (21.59)
30	C	6.91 (30.72)
31	C	6.91 (30.75)
32	C	6.29 (27.99)
33	C	9.29 (41.33)
34	C	8.85 (39.37)
35	C	8.82 (39.25)

Test	Failure mode	Ultimate load, kips (kN)
36	C	9.42 (41.89)
37	S	N/A
38	C	9.34 (41.53)
39	C	10.16 (45.22)
40	C	10.23 (45.49)

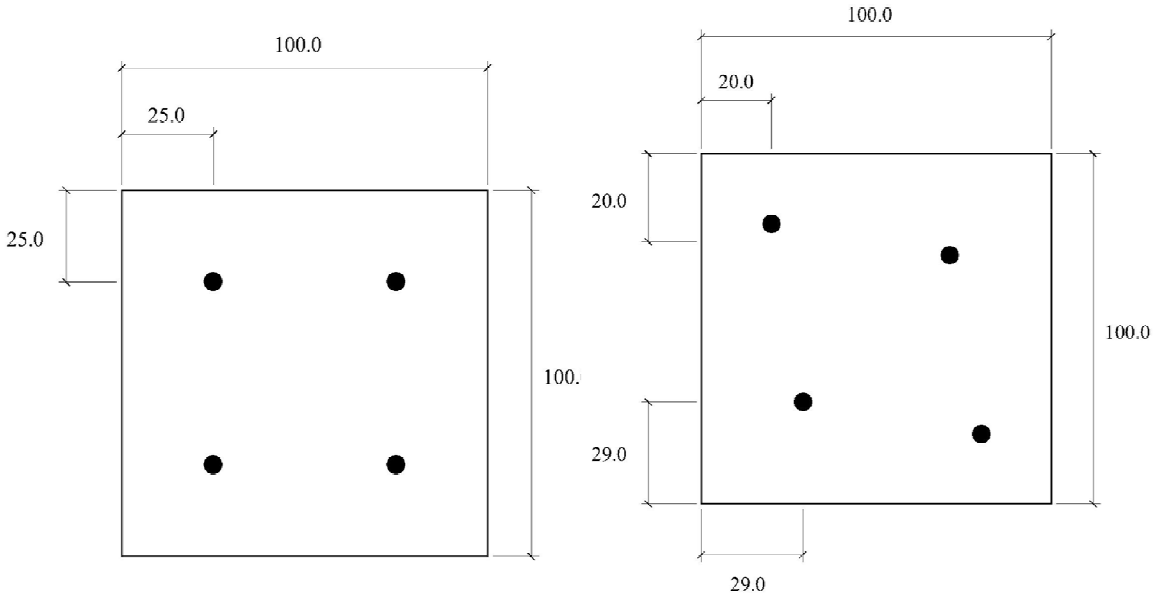

Fig. 4.1 – Position of the headed anchors according to their embedment depth (“Type C” and “Type D” specimens, left, and “Type E” specimen, right); measures in centimeters.

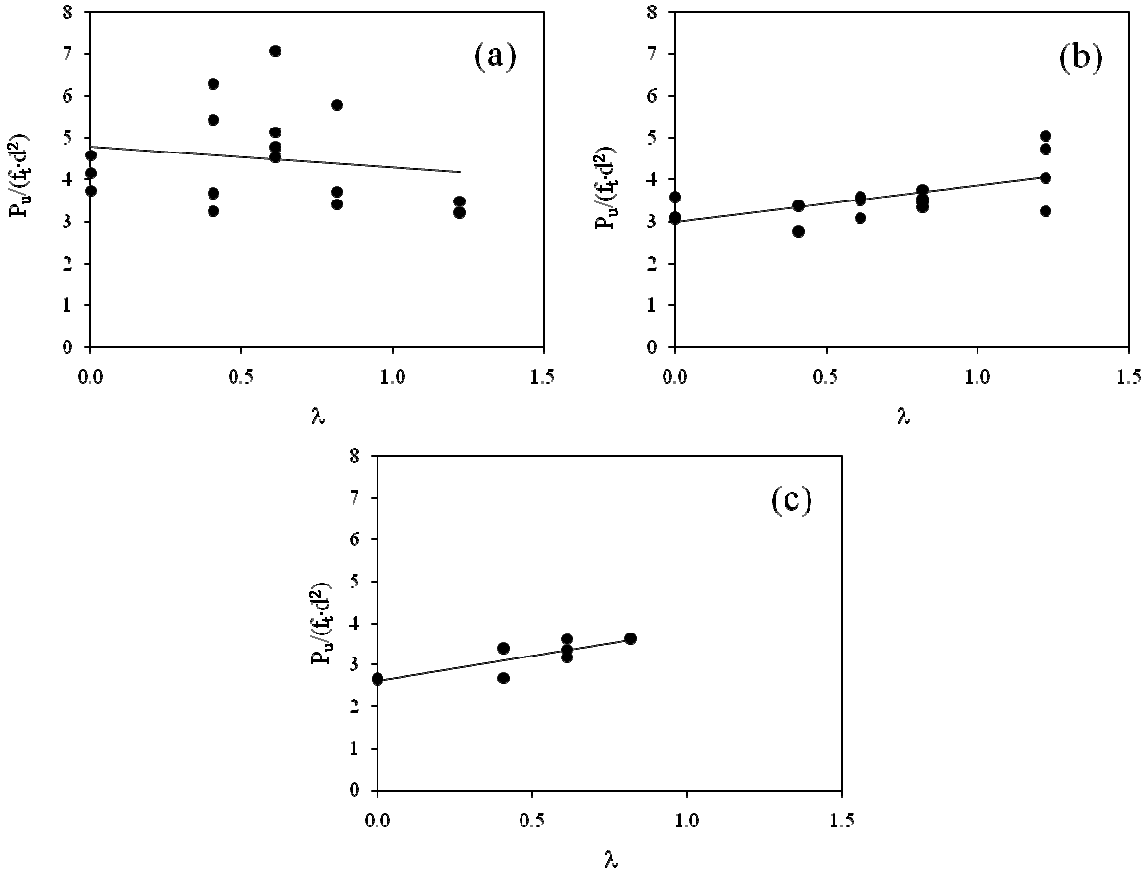

Fig. 4.2 – Normalized ultimate load carrying capacity as function of prestress; (a) $d/c = 0.75$; (b) $d/c = 2$; (c) $d/c = 2.75$;

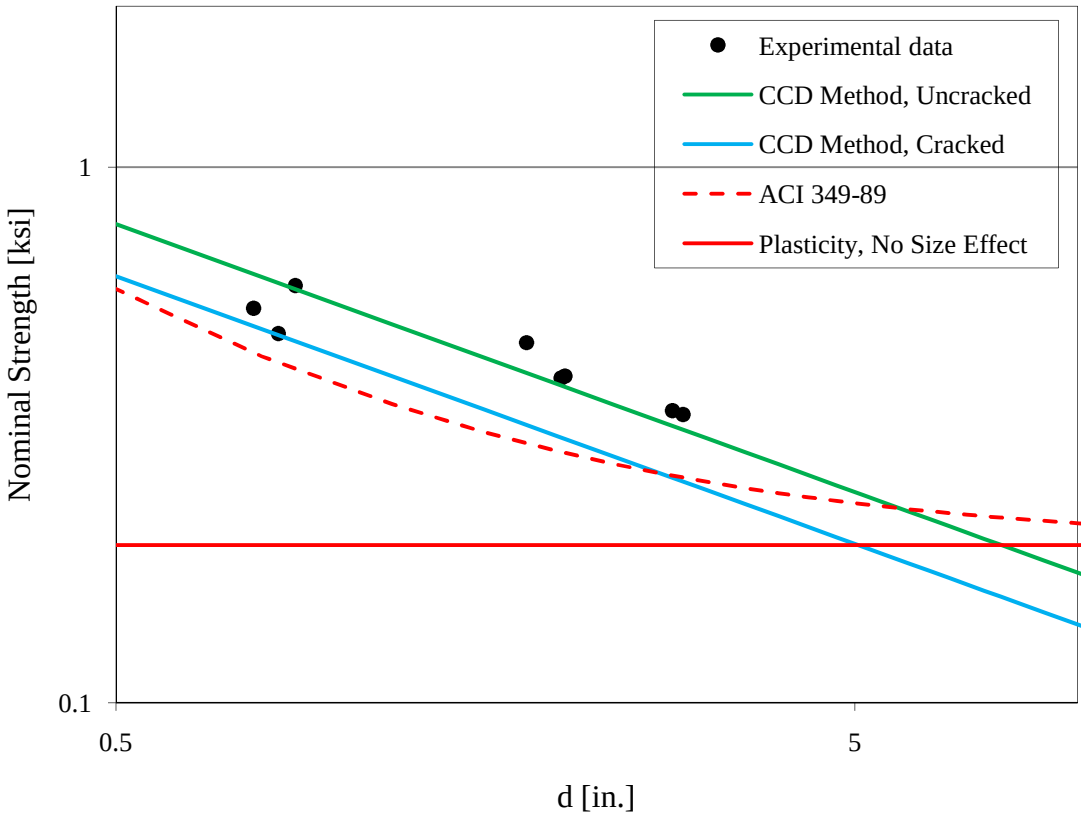

Fig. 4.3 – Log-log plot of nominal pullout strength as a function of the embedment depth for the embedment depths investigated; $\lambda = 0$

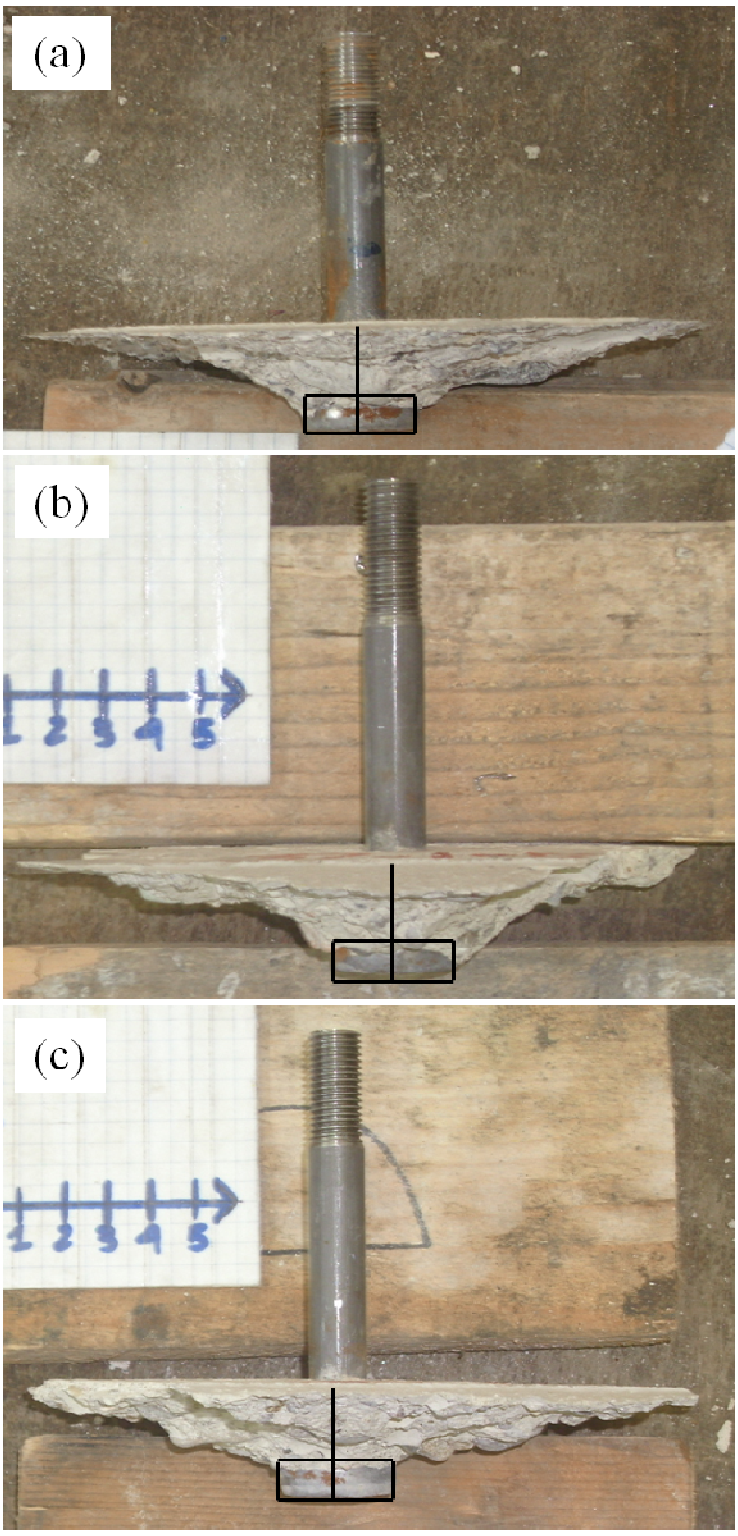

Fig. 4.4 – Example of shallow anchors ($d/c = 0.75$) experimental conical failure surface;

(a) $\lambda = 0.41$, (b) $\lambda = 0.61$, (c) $\lambda = 0.61$

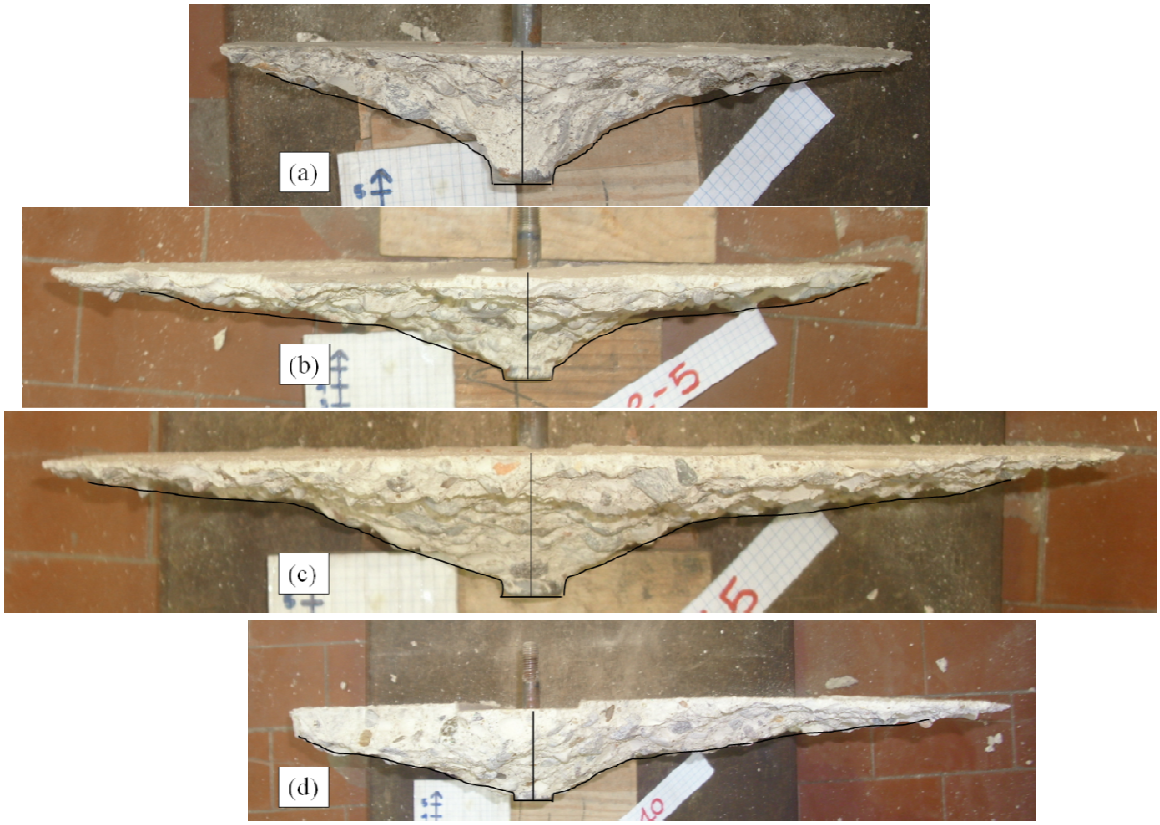

Fig. 4.5 – Visual inspection of failure propagation angle for $d/c = 2$; (a) $\lambda = 0$; (b) $\lambda = 0.41$; (c) $\lambda = 0.61$; (d) $\lambda = 0.82$

CHAPTER 5

NUMERICAL – EXPERIMENTAL COMPARISON

This chapter presents qualitative and quantitative comparisons between the experimental results and the LEFM predictions.

5.1 Comparison between LEFM and Experimental Part I

5.1.1 Quantitative Comparison

Load Carrying Capacity

The experimentally measured normalized ultimate capacity data for unstressed and prestressed concrete are shown in Figures. 5.1a-b. It is remarkable that the linear dependence on prestress predicted by LEFM (which neglects the presence of the process zone and size dependent fracture toughness) is consistent with the experimental results for the relatively shallow embedments tested in this study.

As aforementioned, the brittleness number was first introduced in the concrete community studies of edge-edge crack beams, where the characteristic length L in Eq. (2.1) is taken as the beam depth. Typical values of β for edge-edge crack beams therefore range between 2.5 and 10 (Bazant and Planas [37]; Carpinteri [38]). In this study we arbitrarily assign the embedment depth, d, as the characteristic dimension L in Eq. (2.1). Because of their arbitrary definition, the brittleness numbers discussed subsequently should not be directly related to those of previously reported beam-like specimens.

A comparison between the model's predictions and the experimental results can be achieved by determining a reference value of β. This involves the choice $\beta \approx 0.6$ that provides the best least-square fit to the data presented in Fig. 5.1b (trend line shown using dashed line). This value of brittleness is associated with a value of concrete fracture toughness ($K_{Ic} \approx 0.755 \ \ ksi\sqrt{in}$) that is well within the range of typical values for concrete (Between 0.18 and 1.26 $ksi\sqrt{in}$). Having decided to arbitrarily define L as the embedment depth, d, the experimental data in Fig. 5.1a ($d/c = 1$) is compared with the LEFM prediction associated with $\beta = 0.3$. It is observed that the experimental data is, as expected, slightly bounded from above with the LEFM prediction. Fig. 5.2, where the nominal strength is plotted in a log-log scale as function of brittleness, shows that, independently of the prestress, the experimental results always lie on the line indicating LEFM behavior. Once again, this corroborates previous experimental investigations and is consistent with Figs. 2.1 and 2.4b, according to which the concrete's size effect for this type of problems is the strongest possible.

Load versus Displacement Behavior

The effects of prestress and tensile stresses on ductility are quantified using the work of fracture, *WOF*, defined as the area under the force-displacement curve.

Even though qualitative and based on different definitions of the load-point displacement, Δ, the significant post-peak ductile behavior of the system and the increase in capacity and ductility with the applied compressive stress in the experiments is shown in Appendix B. For a value of $\beta = 0.5$ (Fig. 2.5), it is shown that the LEFM simulations only provide a lower bound solution to the ductility of the system and the size of the pull-

out cone. As previously mentioned, it is noted that our crack propagation simulations showed that as the crack approaches the free surface the convergence to zero force is very slow for large values of applied stress. Therefore the curves shown are truncated when the crack front reaches a distance from the free surface that is equal to ten percent of the embedment depth.

5.1.2 Qualitative Comparison

Crack Initiation Angles and Crack Paths

The outputs of the experimental investigations are compared to the LEFM predictions in Figs. 5. 3a-d for $d/c = 1$ (laser machine readings) and Fig. 5.4 for $d/c = 2$ (visual inspection).

It is shown that the experiments do not differ significantly from the numerical LEFM results (small differences can be observed for the unconfined case). Considering the simplicity of the finite element model and the fact that inhomogeneities and aggregates can give rise to very tortuous crack paths, LEFM does a good job of predicting the crack paths.

5.2 Comparison between LEFM and Experimental Part II

5.2.1 Quantitative Comparison

Load Carrying Capacity

The experimentally measured normalized ultimate capacity data for unstressed and prestressed concrete are shown in Figures 5.5a-c. Once again (except for the

shallower case of Fig. 5.5a), the linear dependence on prestress predicted by LEFM is consistent with the experimental results.

A comparison between the model's predictions and the experimental results can be achieved by determining a new reference value of β. This involves the choice $\beta \approx 1.13$ that provides the best least-square fit to the data presented in Fig. 5.5c (trend line shown using dashed line).

This value of brittleness is associated with a value of concrete fracture toughness ($K_{Ic} \approx 0.65 \ \ ksi\sqrt{in}$) that is, once again, well within the range of typical values for concrete (Between 0.18 and 1.26 $ksi\sqrt{in}$). Having decided to arbitrarily define L as the embedment depth, d , the experimental data in Fig. 5.5b ($d / c = 2$) is compared with the LEFM prediction associated with $\beta = 0.8$ and the experimental data in Fig. 5.5a ($d / c = 0.75$) is compared with the LEFM prediction associated with $\beta = 0.3.$ It is observed that the experimental data is, as expected, bounded from above with the LEFM prediction.

As shown in Fig. 5.6, and similarly to what was observed in the first part of the experimental program, the experimental data show to agree reasonably well with the LEFM predictions, independently of the prestress applied to the concrete matrix. This type of model represents a very good tool to determine the ultimate load carrying capacity of headed anchors embedded at depths $d / c \geq 1$. When very shallow embedment depths ($d / c = 0.75$) or very small values of β are considered, the LEFM solution becomes an unconservative upper bound. Whether nonlinear fracture mechanics can predict the capacity of the smallest embedment anchors is addressed in the next chapter.

5.3 Preliminary Conclusions

From the comparison between the results from two separate sets of experiments and the results from the LEFM simulations, a significant size effect on the concrete cone pullout failure strength is confirmed for embedment depths as small as $d/c = 1$.

Even though carried out with different materials (different values of β), the experimental results show consistency in that the LEFM predictions can accurately predict the linear dependence of the anchor capacity on the prestress.

The application of prestress values in the typical range ($\lambda \approx 0.5$) leads to a limited increase in capacity (about 10%) with respect to the unconfined case. The values of λ used in the experiments are in the range of values typically used in prestressed concrete applications. The small increase in capacity seems to indicate that the effects of prestress are beneficial, but not significantly affecting the behavior of headed anchors.

The crack paths (and the concrete failure cones) experimentally obtained by using a scanner ($d/c = 1$) or by visual inspection ($d/c = 2$), show to agree significantly well with the LEFM predictions.

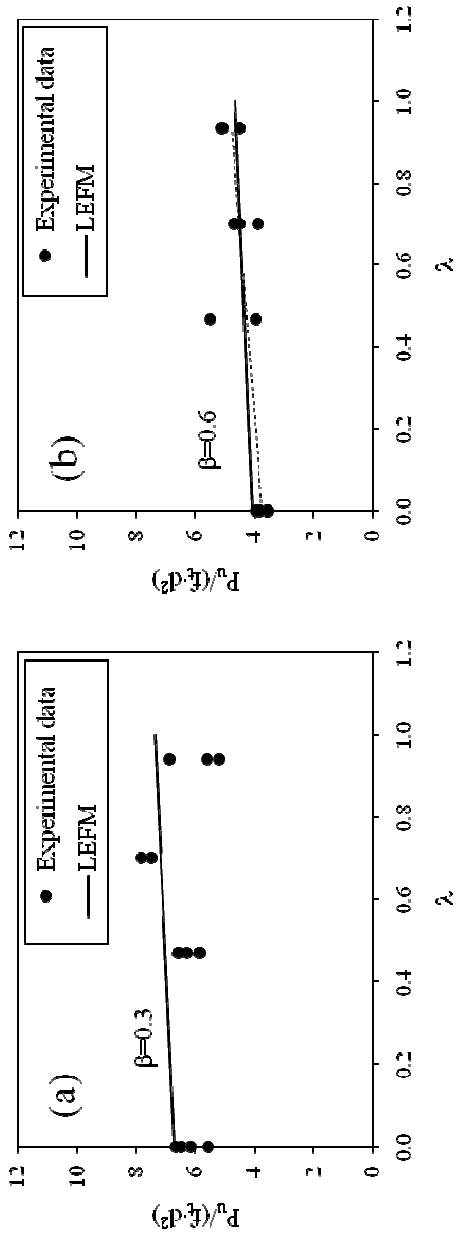

Fig. 5.1 – Ultimate dimensionless pullout load as functions of stress; (a) $d/c = 1$; (b) $d/c = 2$

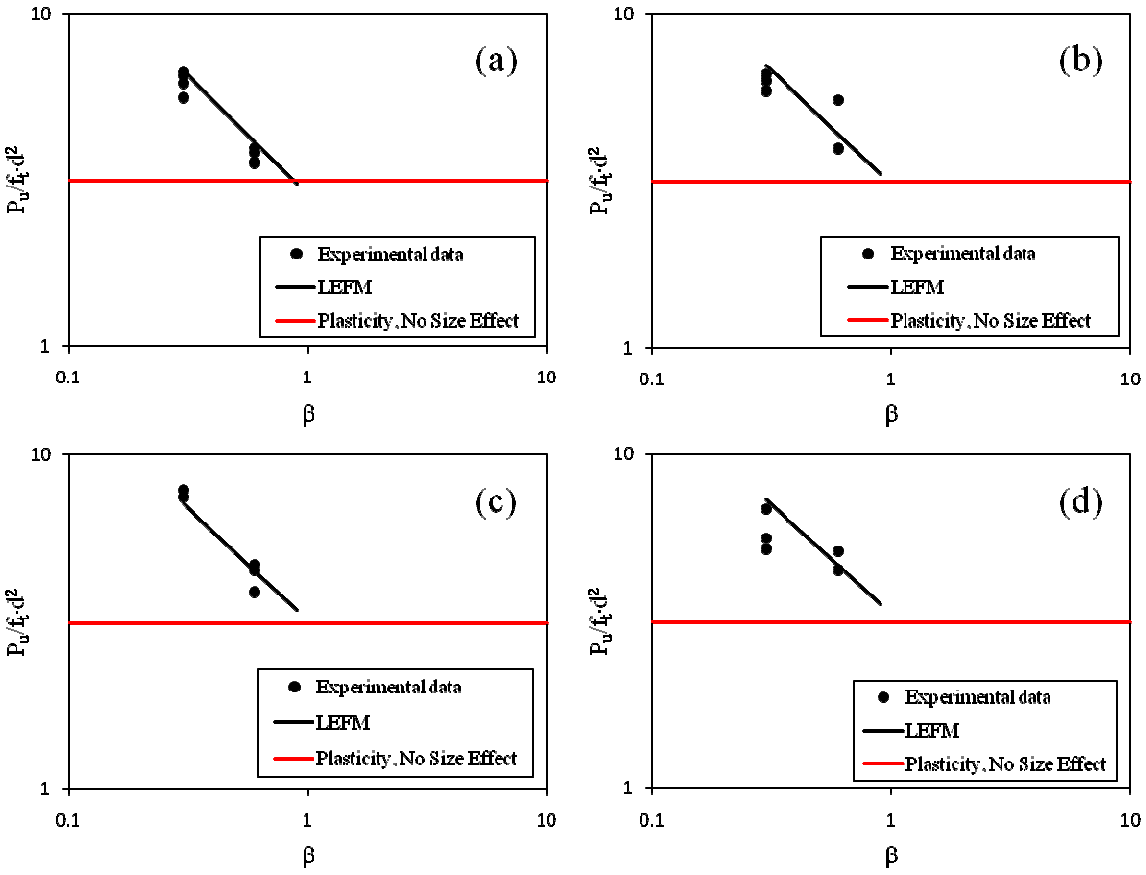

Fig. 5.2 – Log-log scale plot of the brittle-to-ductile transition for the pullout failure strength: comparison between experimental data and theoretical bounds; (a) $\lambda = 0$; (b) $\lambda = 0.47$; (c) $\lambda = 0.7$; (d) $\lambda = 0.94$

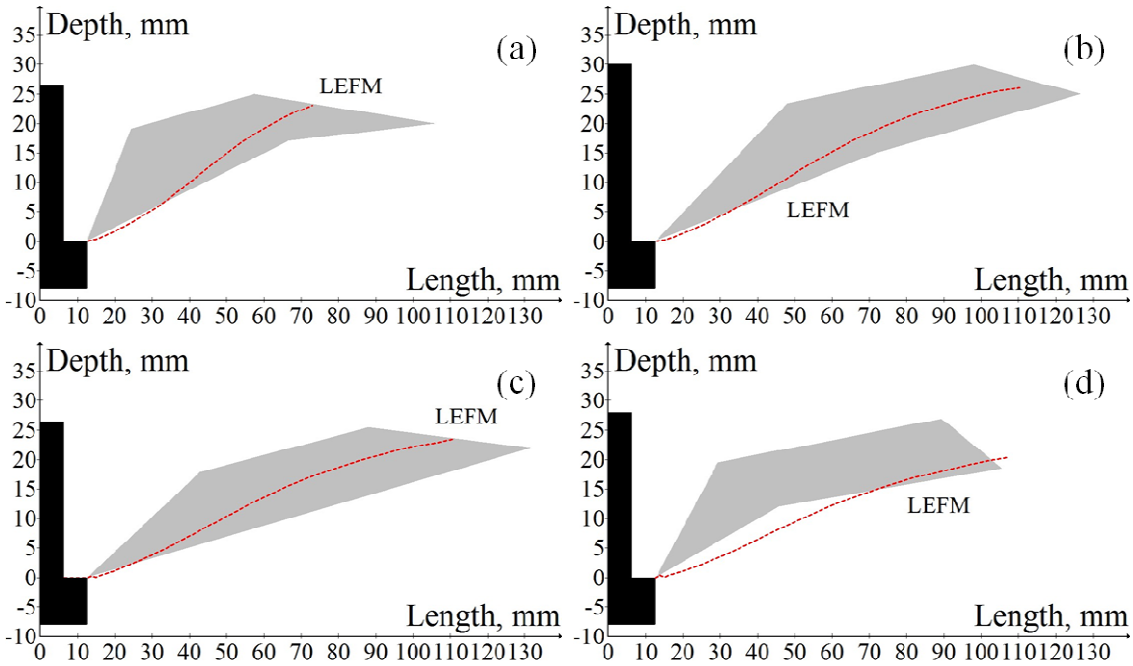

Fig. 5.3 – Comparison of crack profiles from experiments and LEFM simulations (red dashed line); $d/c = 1$ and (a) $\lambda = 0$; (b) $\lambda = 0.47$; (c) $\lambda = 0.7$; (d) $\lambda = 0.94$

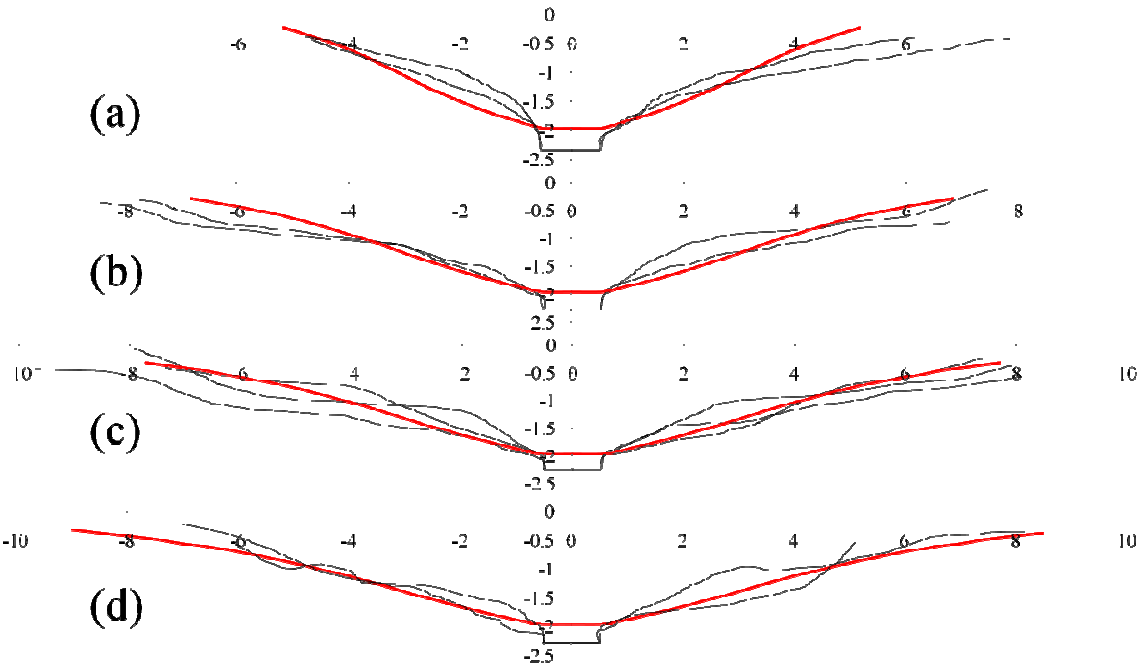

Fig. 5.4 – Comparison between LEFM predictions (continuous red lines) and experimental crack propagation patterns; (a) $\lambda = 0$; (b) $\lambda = 0.41$; (c) $\lambda = 0.61$; (d) $\lambda = 0.82$ (Note: pictures not in scale)

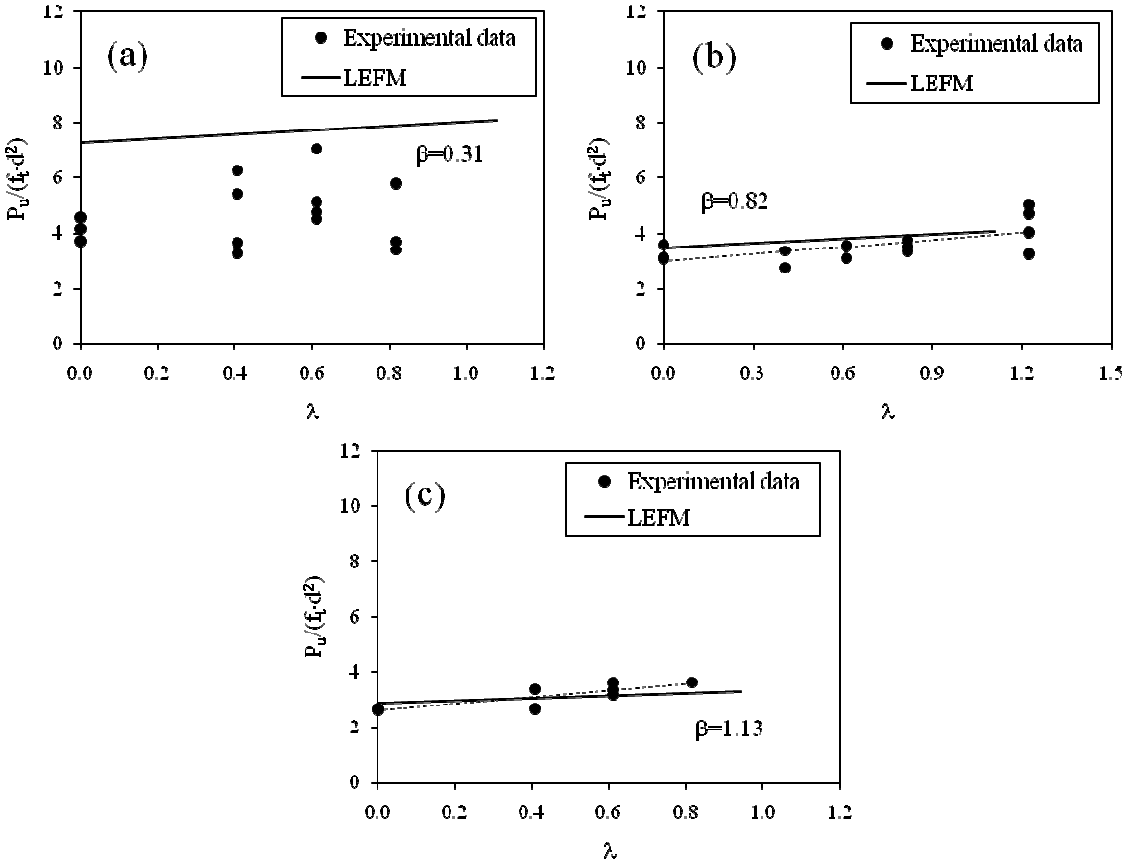

Fig. 5.5 – Ultimate dimensionless pullout load as functions of prestress; (a) $d/c = 0.75$; (b) $d/c = 2$; (c) $d/c = 2.75$

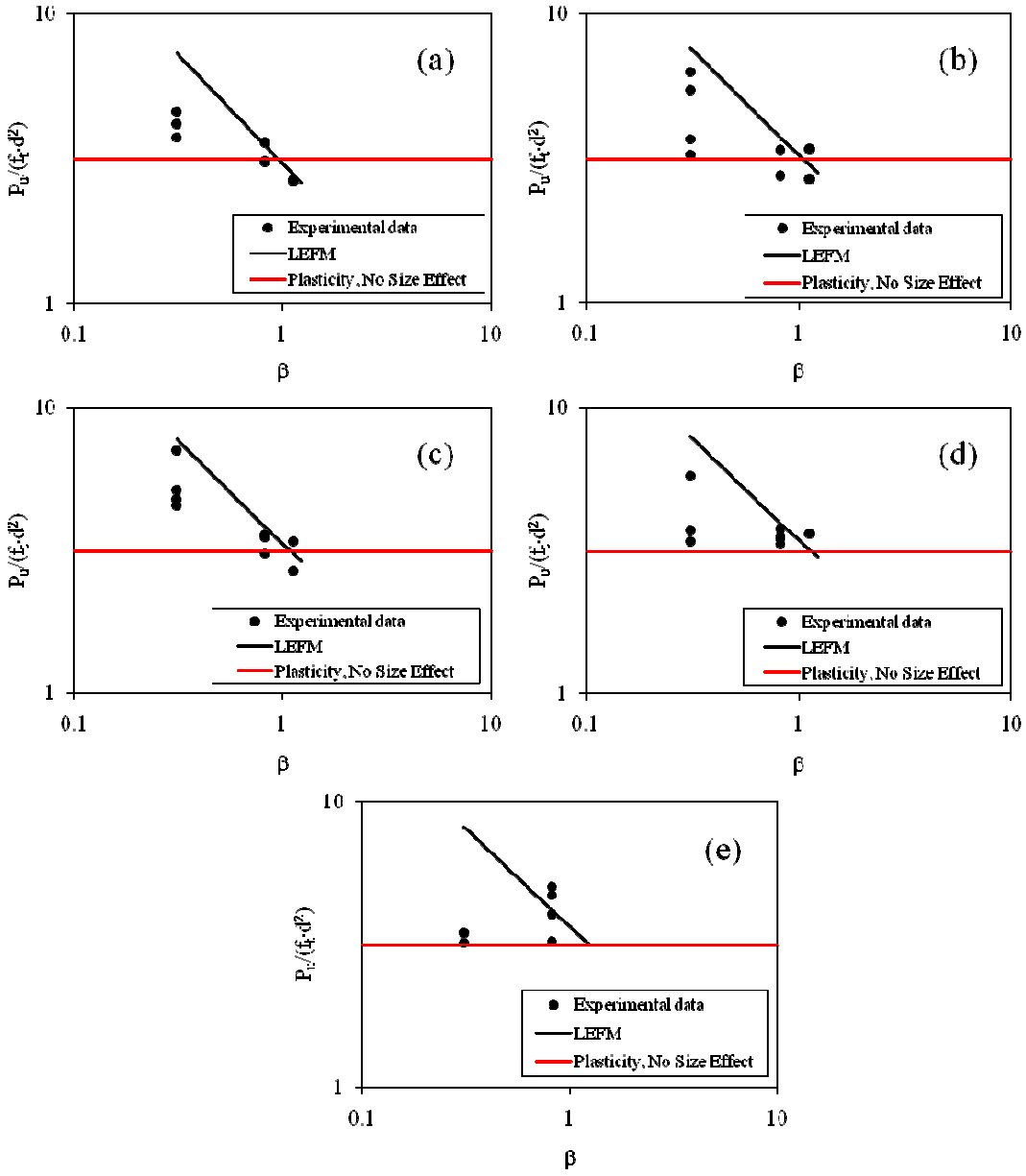

Fig. 5.6 – Log-log scale plot of the brittle-to-ductile transition for the pullout failure strength: comparison between experimental data and theoretical bounds; (a) $\lambda = 0$; (b) $\lambda = 0.41$; (c) $\lambda = 0.61$; (d) $\lambda = 0.82$; (e) $\lambda = 1.22$

CHAPTER 6

NONLINEAR FRACTURE MECHANICS MODELING OF EXPERIMENTS

The results presented in the previous chapters showed that LEFM cannot predict the ultimate load capacities of headed anchors embedded at embedment depths $d/c < 1$. There are two possible explanations. The first, and most probable, is that for such shallow embedments the fracture occurs within a region whose size is approximately equal to that of the aggregates, so that a deterministic continuum theory does not apply. Nevertheless, this chapter explores the possibility that the behavior of the shallow anchors could be characterized by nonlinear fracture mechanics.

6.1 The Fracture Process Zone for Concrete and Concrete-like Materials

Concrete is a heterogeneous material consisting of aggregate and cement in various ratios; it is a cement-based composite. The front of a crack propagating within such materials is surrounded by a process zone within which a significant amount of microcracking and other inelastic deformations occurs. Furthermore, because cracks in these materials are tortuous, aggregate (mechanical) interlock occurs between opposing crack surfaces. The fracture behavior of these cohesive materials is greatly influenced by the size of the process zone, within which a significant amount of externally provided energy is dissipated.

The process zone has a thickness of approximately a few aggregate diameters. The energy dissipation mechanisms occurring within this localization band introduces an

internal length scale and a quasi-brittle behavior characterized by strain softening in the post-peak regime of a load displacement trace. (Shah *et al.* [47]).

In addition to other factors (for further details, refer to Bazant and Planas [37], Shah *et al.* [47]), the fracture process zone in concrete materials is responsible for the so called effect of size that has been widely investigated in the last decades. Experimental investigations, in fact, have shown that the normalized strength of concrete usually decreases with increasing specimen size. This phenomenon is related to the ratio between the size of the fracture process zone and a given characteristic size of the specimen (beam depth, distance from a notch tip to the further edge of a specimen, embedment depth of an anchor, etc.). From an energetic point of view, when the fracture process zone is small compared to the size of the structure, the energy supplied to the system is employed to create new crack surfaces. However, when the fracture process zone is significantly large, more energy will be spent to overcome the resisting and toughening mechanisms between the crack faces. This is the reason for the reduction in strength with increasing size in concrete structures.

When a fracture process zone surrounds the tip of a crack, application of LEFM concepts could be significantly erroneous. This is because the toughening mechanisms happening along the process zone might lead to fracture toughness values much larger than the one obtained by simply considering a linear behavior of the material. Therefore, principles of nonlinear fracture mechanics and its numerical implementation will be presented next.

6.2 The Cohesive Crack Model in Mode I

A physical model was originally developed by Dugdale [48] to take into account for plastic deformations and behavior in front of a cohesive crack tip. Dugdale developed his mode-I model by observing the behavior of thin steel sheets, which are associated with a plastic zone whose thickness is of the order of the thickness of the sheet. As schematically shown in Fig. 6.1, by enforcing that the stress singularity at the tip of the process zone (ρ) needs be equal to zero to render the stresses finite (and equal to the yield stress of the material, σ_y), he applied the principle of superposition of two elastic crack solutions to determine the length of the process zone for a given value of applied loading (σ_{FF}), and postulated that the crack extends when the crack opening displacement at the trail end of the process zone reaches a critical material value (critical opening displacement, COD_c). Following this reasoning, the length of the process zone can be expressed as follows

$$\frac{\rho}{a} = \sec\left(\frac{\pi \cdot \sigma_{FF}}{2 \cdot \sigma_y}\right) - 1 \tag{6.1}$$

and the critical opening displacement as

$$COD_c = \delta_{tip} = \frac{8 \cdot \sigma_y \cdot a}{\pi \cdot E} \cdot \log\left[\sec\left(\frac{\pi \cdot \sigma_{FF}}{2 \cdot \sigma_y}\right)\right] \tag{6.2}$$

Subsequently, numerous investigators proposed models to represent the fracture zone effects in other materials (ceramics, concrete, etc.). For concrete like materials, Hillerborg *et al.* [49] developed the so-called “fictitious crack” model in mode I. In this model, the process zone is modeled as an extension of the actual crack subjected to a closing pressure dependent on the crack opening displacements. The effective crack

length is obtained by summing the portion of the crack that is stress (traction) free and the zone within which the mechanical interlock and microcracking occur (process zone). Figure 6.2 shows this concept schematically. The tip of the fracture process zone is referred to as “fictitious crack tip”. The cohesive stresses are represented by a monotonic decreasing function of the crack opening displacement (COD). The area under the softening stress vs. displacement curve is commonly referred to as the fracture energy, G_f.

Being a material property by definition, the softening function expressing stresses in function of COD is the key parameter of the fictitious crack model. More specifically, three properties of the softening curve are important: the value of the tensile strength of the material (f_t), the value of the cohesive fracture energy (G_f), and the shape of the softening curve. In the present study, and in general for concrete-like materials, the process zone stress distribution can be modeled using a linear function as follows:

$$\sigma = f_t \cdot (1 - \frac{COD}{COD_c}) \tag{6.3}$$

where f_t is the uniaxial tensile strength of the material, and COD_c is the critical crack opening displacement, which represents the separation between stress free crack and the process zone. Other softening functions with different shapes (bi-linear or exponential softening) were developed in the past decades because they were shown to better match experimental data.

Experimental tests (Hillerborg *et al.* [49]) were carried out to test the fictitious crack model and it was shown that this approach provides realistic and accurate description of the fracture phenomenon. Since then, non-linear fracture mechanics

approaches (Hillerborg [50, 51], Ingraffea [52], etc.) have been developed analytically and numerically (mainly by means of the finite element method) to describe the fracture of cement-based materials.

In the finite element method, successful investigations have involved both the smeared crack and the discrete crack approaches. In particular, when the discrete crack approach is used, the cohesive forces acting along the crack faces and the cohesive part of the crack have been efficiently modeled by using interface elements. This is the case of FRANC2D [42], where interface elements can be placed between the crack faces and different types of linear and nonlinear (softening) cohesive constitutive laws can be easily implemented. The software allows the use of singular or nonsingular crack tip finite elements. In the ACI 446 [53] report (Shah *et al.* [47]), the advantages of using the discrete crack model with singular elements and interface elements have been described. In the document, it is stated that interface elements represent the natural way to describe the physics and the nature of the cohesion between crack faces and that, by using such elements, the number of degrees of freedom involved in the solution of the problem is significantly minimized.

When dealing with cohesive crack problems, a stability (or equilibrium) condition is necessary to compute the size of the process zone. Originally, Hillerborg *et al.* [49] and Peterson [54] proposed that the stress at the fictitious crack tip should be equal to the tensile strength of the material. Other criteria were based on Dugdale's first approach and focused on the search for the condition of zero singularity at the crack tip (Ingraffea and Saouma [55]). Furthermore, because of the finite nature of the stresses along the process zone and ahead of the fictitious crack tip, another criterion was developed by Bittencourt

et al. [56], according to which equilibrium is represented by the condition of maximum smoothness of the fictitious crack tip opening profile. This condition is usually referred to as the “zero gradient” crack opening profile.

6.3 The Cohesive Crack Model in Mixed Mode

The applicability of the cohesive crack model to more common mixed mode conditions has been the focus of several investigations in the last decades. In the case of a Mode I crack problem, the cohesive closing pressure is always orthogonal to the crack faces. Furthermore, being developed in a pure Mode I condition, the crack path is always known a priori and when the condition of instability is reached, the crack will propagate straight ahead. When a mixed mode geometry or loading condition is to be modeled, however, the crack trajectory is not known a priori and the stresses along the process zone have normal and tangential components. Similarly to the normal stresses, the behavior and the distribution of the shear stresses (τ) are related to the crack sliding displacement (CSD).

As for the mode I problems, in some cases the propagation condition relies on a strength criterion (Hillerborg *et al.* [49], Peterson [54], Gerstle *et al.* [57], Bocca *et al.* [58], [59], [60]). When this criterion is used, a very fine mesh at the crack tip is required to obtain an accurate estimate of the principal stresses (Bocca *et al.* [58], Gerstle *et al.* [57]).

Ingraffea and Saouma [55], Ingraffea *et al.* [61], Wawrzynek and Ingraffea [62], and Hellier *et al.* [63] employed a strategy of cancellation or near-cancellation of the singularity to solve the mixed mode crack propagation problem. By iterating on the load

or the crack length, crack stability was sought by determining the condition for which the stress intensity factors were equal to zero or to some residual values. Even though the mesh dependency was avoided, this method sometimes failed to predict accurately the critical load because the singular elements at the crack tip perturbed the stress field in the cohesive zone and ahead of the fictitious crack tip.

Another approach to the mixed mode problem was proposed at first by Xie and Gerstle [64]. In their investigations, they implemented an energy based finite element approach by generalizing previously developed techniques (Parks [65], Hellen [66]). In essence, by using the principle of conservation of energy, the crack propagation condition is considered to be the condition of minimum potential energy for the whole boundary value problem. In addition to the numerical implementation of this criterion, Xie developed an algorithm for the automatic remeshing and propagation of a discrete cohesive crack. Numerical simulations showed that the experimental behavior could be captured with high accuracy even when the mesh size was not significantly refined.

In mixed mode problems, besides determining the critical condition for crack propagation, a condition for the direction of crack propagation needs to be established. Even though developed for LEFM, the maximum hoop stress criterion (Erdogan and Shih [67]) is still a reasonable model to determine the directionality of propagation for crack including cohesive behavior.

The finite element models to simulate the discrete cohesive crack in the pullout problem are presented next. They are based on the predefined LEFM crack path approach. A case study completed using the automatic crack propagation approach will be also described.

6.4 Pullout Investigation: The Predefined Crack Path Approach

Linear elastic fracture mechanics (LEFM) has proven its worth to predict the mixed mode crack paths, even for complex trajectories (Bittencourt *et al.* [56], Galvez *et al.* [68, 69], and Cendon *et al.* [70]). Furthermore, it has been shown that even for complex mixed mode problems, the mixed mode II fracture energy (G_f^{II}) only slightly influences the crack growth and the overall load versus displacement behavior of concrete specimens.

As a support for the previous remarks, in the experimental program carried out for the present investigation, the LEFM predictions of the crack trajectories showed to be in good agreement with the experimental evidence (Figs. 5.3 and 5.4). Small differences could be observed for the unconfined case, where the experimentally obtained concrete cones presented a slightly steeper initial failure angle. Following this reasoning, the LEFM predictions were used as predetermined crack paths. The LEFM trajectories were obtained by using the same values of the brittleness numbers, β, that were previously used to calibrate the experimental data. In each simulation, the crack propagation direction was established by using the maximum hoop stress criterion. The crack trajectories employed in the present study are shown in Figs. 6.3 (Experimental part I) and 6.4 (Experimental part II). After cohesive elements were inserted along the predefined crack paths, results in terms of ultimate load carrying capacity and load versus displacement behavior were obtained by changing the cohesive constitutive law.

6.4.1 Calibration of Experiments: Part I

For the calibration of the first part of the experiments, a linear softening constitutive law (Eq. 6.3) in mode I was used to describe the behavior of the cohesive elements along the LEFM predetermined crack paths (Fig. 6.3). A maximum tensile strength equal to 400 psi (2.77 MPa) and a maximum critical crack opening displacement of 0.001 in. (26 μm) were considered (Fig. 6.5a). Frictional stresses were neglected. By using these parameters, the value of the cohesive fracture energy, G_f, is equal to about 0.2 lb/in. (35 N/m). Fracture properties of the concrete employed in the experiments were not investigated; however, a characteristic length of the fracture process zone could be defined as follows (Shah *et al.* [47]):

$$l_{ch} = \frac{E \cdot G_f}{f_t^{\,2}} \tag{6.4}$$

For concrete, the value of l_{ch} ranges between 4 in. (100 mm) and 16 in. (400 mm). With the properties used in the numerical model (E, G_f, f_t), $l_{ch} \approx 4in.$, that is within the above given range.

It is noted that the value of the fracture energy is relatively low if compared to values available in the literature. CEB [27] recommends, for the type of concrete and aggregate size used, values of G_f of about 60 or 70 N/m. However, the suggestion comes for concretes where the water/cement ratio is around 0.3-0.4 and where the cohesive law is usually specified as a softening bi-linear function. For these reasons, it is not surprising (Wittmann *et al.* [71]) to find very low values of G_f for concretes cast with high water/cement ratios.

Load Carrying Capacity

The ultimate load carrying capacities obtained from the analyses including nonlinear cohesive elements are shown in Fig. 6.6, where the experimentally obtained ultimate load carrying capacities were normalized using the measured uniaxial tensile strength of the material (f_t =417 psi [2.88 MPa]) and the relative embedment depth, d . The calibration of the softening constitutive law for the cohesive elements was carried out by assuming that the NLFM predictions should coincide with the LEFM predictions when considering large embedment depths ($d/c = 2$).

Valuable information can be derived from Fig. 6.6. First, from a quantitative point of view, for $d/c = 2$, the NLFM results are identical to the LEFM predictions. By using the same fracture energy, for the embedment $d/c = 1$, it is shown that NLFM is capable of capturing the experimental behavior slightly better than LEFM. Nevertheless, LEFM still represents a very close upper bound to the real behavior. From a qualitative point of view, the linear dependence of the ultimate load carrying capacity on the prestress is confirmed to be linear, even when cohesive elements are introduced along the crack faces.

As shown in Fig. 6.7, where the experimental data is compared to the LEFM, NLFM, and plasticity-based predictions in a log-log scale plot, the closeness of the LEFM and NLFM behavior validates the fact that the concrete's size effect for headed anchors is the strongest possible ($d^{1.5}$ -dependence), and that LEFM is a very accurate tool to investigate their behavior.

A comparison with the experimental data and the available design formulas for the unstressed case ($\lambda = 0$) is also shown in Fig. 6.8. Here, the CCD-method design

formula [Eq. 1.3] was evaluated using values of the constant k_c for cracked and uncracked concrete (24 and 30, respectively). It appears that the fracture mechanics based approach mimics quite well the experimental evidence, and that the CCD-method only provides a lower bound solution (conservative) when shallow anchors are investigated. This supports the fact that the non-dimensional function, $f_1\left(\frac{l}{d},\frac{d}{c},\nu\right)$, introduced in Eq. 2.2, is indeed a weak function of the embedment depth. The CCD-method and the LEFM approaches, nevertheless, give identical results for relatively large embedment depths.

Load versus Displacement Behavior

The load versus displacement behavior obtained from the numerical simulations is shown in appendix B. As for the LEFM case, it is noted that these curves only represent a lower bound solution when compared to the real behavior. It is concluded that, while the discrete crack model can predict quite accurately the load capacities of headed anchors, it might not be a suitable tool to capture the overall load versus displacement behavior of the system. In the future, further investigations should be dedicated to this aspect.

6.4.2 Calibration of Experiments: Part II

For the calibration of the second part of the experiments, as was done in the first part, a linear softening constitutive law in mode I (Eq. 6.3) was used to describe the behavior of the cohesive elements positioned along the LEFM predetermined crack paths (Fig. 6.4). A maximum tensile strength equal to 300 psi (2.1 MPa) and a maximum critical crack opening displacement of 0.001 in. (26 μm) were considered (Fig. 6.5b). Frictional stresses were neglected. By using these parameters, the value of the cohesive

fracture energy, G_f, is equal to about 0.15 lb/in. (27 N/m). This choice is representative of a value of $l_{ch} \approx 3in.$ (Eq. 6.4), that is smaller than the typical range of values for concrete (4 to 16 in.). However, as previously explained, the use of a linear softening relation and the high w/c ratio used to cast the concrete are most likely the reasons for having to use small values of G_f.

Load Carrying Capacity

The ultimate load carrying capacities obtained from the analyses are shown in Fig. 6.9, where the ultimate load carrying capacities were normalized using the experimentally measured uniaxial tensile strength of the material (f_t=412 psi [2.85 MPa]) and the measured embedment depth, d.

As expected (Figs. 6.9b and 6.9c), NLFM and LEFM provide identical results for relatively large embedment depths ($d/c = 2$ and $d/c = 2.75$), while for $d/c = 0.75$ they both provide an upper bound solution to the experimental behavior (Fig. 6.9a).

The ductile-to-brittle transition for the pullout failure strength is illustrated in Fig. 6.10, where experimental and numerical normalized capacities are plotted in a log-log scale diagram with respect to the brittleness number. For shallow anchors, the predictions from LEFM and NLFM represent an upper bound, while the plasticity based approach represents a lower bound. None of the approaches is capable of mimicking the experimental behavior.

Fig. 6.11 illustrates, for the unstressed case, the comparison between the actual design code provisions and the finite element model results. The results for the shallower investigated case are still bounded from below if compared to the ACI 349-89 formula.

The fact that for extremely shallow anchors neither LEFM nor NLFM can provide an accurate solution illustrates the limits of the currently used finite element model; as a consequence, other factors (material heterogeneities, stress concentrations, etc.) should be taken into account when looking at the experimental behavior of these inserts. Some images of these anchors, illustrating the very shallow cone failure surfaces, were shown in Fig. 4.4.

6.4.3 A Case Study: The Automatic Crack Propagation Approach

A series of finite element models using cohesive elements and based on an incremental type approach were carried out. As explained above, when incremental analyses are approached, two conditions need to be sought:

- A criterion to determine the load required to extend the crack;
- A criterion to establish the crack propagation direction;

The load required to extend the crack was determined by using the "cancellation near singularity" criterion. According to the displacement correlation technique (Barsoum [43]), the mode I (K_I) and mode II (K_{II}) stress intensity factors can be expressed in terms of the crack tip nodal displacements as follows

$$K_I = \frac{G}{\kappa+1}\cdot\sqrt{\frac{2\pi}{L_Q}}\cdot\left[4\cdot\left(v'_B - v'_D\right) - \left(v'_C - v'_E\right)\right] \tag{6.5}$$

and

$$K_{II} = \frac{G}{\kappa+1}\cdot\sqrt{\frac{2\pi}{L_Q}}\cdot\left[4\cdot\left(u'_B - u'_D\right) - \left(u'_C - u'_E\right)\right] \tag{6.6}$$

where G is the shear modulus, $\kappa = (3-4\nu)$ for axisymmetry and plane strain problems, ν is the Poisson's ratio, L_Q is the length of the quarter-point element along the crack face, and u', v' are the local displacements along and normal to the crack axis (Fig. 6.12).

In the present simulations, the crack extension condition was sought by determining the load for which the stress intensity factors at the crack tip were equal to zero or to some residual values. When present, the residual singularities were set to zero by using a certain combination of the crack tip nodal displacements (multipoint constraints).

The maximum hoop stress criterion was used to determine the propagation direction of the crack front. When singularities are taken into account (LEFM), the stresses near a crack tip can be expressed in polar coordinates as a combination of the stress intensity factors (Barsoum [43])

$$\sigma_{\vartheta\vartheta} = \frac{1}{\sqrt{2\pi r}}\cos\left(\frac{1}{2}\vartheta\right)\left[K_I\cos^2\left(\frac{1}{2}\vartheta\right) - \frac{3}{2}K_{II}\sin(\vartheta)\right] \tag{6.7}$$

And

$$\tau_{r\vartheta} = \frac{1}{2\sqrt{2\pi r}}\cos\left(\frac{1}{2}\vartheta\right)\left[K_I\sin(\vartheta) + K_{II}\left((3\cos(\vartheta)-1\right)\right] \tag{6.8}$$

The maximum of $\sigma_{\vartheta\vartheta}$ happens when $\tau_{r\vartheta}$ is zero, and consequently, the crack propagation angle, ϑ, can be expressed as

$$\vartheta = 2\tan^{-1}\left[\frac{1}{4}\frac{K_I}{K_{II}} \pm \frac{1}{4}\sqrt{\left(\frac{K_I}{K_{II}}\right)^2 + 8}\right] \tag{6.9}$$

In the case of a cohesive crack, Eq. 6.9 becomes meaningless. Nonetheless, the stresses (finite) ahead of the fictitious crack tip are still useful to determine the crack propagation direction.

In the present study, to accurately take into account for the correct stress distribution in front of the crack tip, the maximum hoop stress, $\sigma_{\vartheta\vartheta}$, was computed for different radii, r_i, around the fictitious crack tip (Fig. 6.13). The crack propagation angle, $\vartheta_{average}$, was then obtained by averaging among the computed propagation directions as

$$\vartheta_{average} = \frac{\vartheta(r_1) + \vartheta(r_2) + \vartheta(r_3)}{3} \tag{6.10}$$

This case study was carried out in the attempt to calibrate the experimental investigations involving the embedment depth $d/c = 1$ (Experiments, part I). The constitute law used to describe the behavior of the cohesive elements was identical to the one used for the predetermined crack path approach (Linear softening, i.e., Fig. 6.5a).

The results are shown in Figs. 6.14 and 6.15. It can be observed that when cohesive elements are used to carry out incremental analyses, the fracture profiles and the ultimate load-carrying capacities are very similar to the ones obtained by using cohesive elements along the predetermined LEFM crack trajectories. Nevertheless, this validates the predefined crack approach described above and the results from several other investigations (Bittencourt *et al.* [56], Galvez *et al.* [68, 69], and Cendon *et al.* [70]).

6.5 Observations

The results from the finite element analyses including elements of the cohesive type highlight the following:

- The concrete's size effect in headed anchors applications is the strongest possible, even when very shallow embedment depths are investigated ($d/c=1$). This is supported by the closeness between the results from NLFM and LEFM predictions;
- For anchors very close to the concrete surface ($d/c=0.75$), the type of failure does not change (conical surface). However, the predictions from LEFM and NLFM become an upper bound, while the plasticity-based approach remains a lower bound. Further investigation is required for this type of anchors and embedment depths. The fact that the embedment depth is smaller than the maximum aggregate size might suggest that a continuum-based theory is not suitable to investigate the problem.
- Crack pattern predictions obtained from NLFM incremental analyses are very close to the experimental and LEFM predictions. This supports the predefined crack approach and previous investigations;
- In the unstressed case, it is shown that the non-dimensional function, $f_1\left(\frac{l}{d},\frac{d}{c},\nu\right)$, introduced in Eq. 2.2, is indeed a weak function of the embedment depth. It follows that the actual CCD method, for all embedments, is always conservative;
- The application of prestress, as preliminary observed in the previous LEFM investigations, allows for an increase in the anchors' capacity. When a value of $\lambda=1$ is considered, the increase in capacity from the numerical investigations is of the order of 12 to 17% with respect to the unconfined case, while the experimental evidence shows that the increase in capacity can be as high as 20-25%. This observation corroborates the fact that, except for the cases mentioned

above ($d/c \leq 1$), the model presented here is efficient in that it provides a conservative (design) approach.

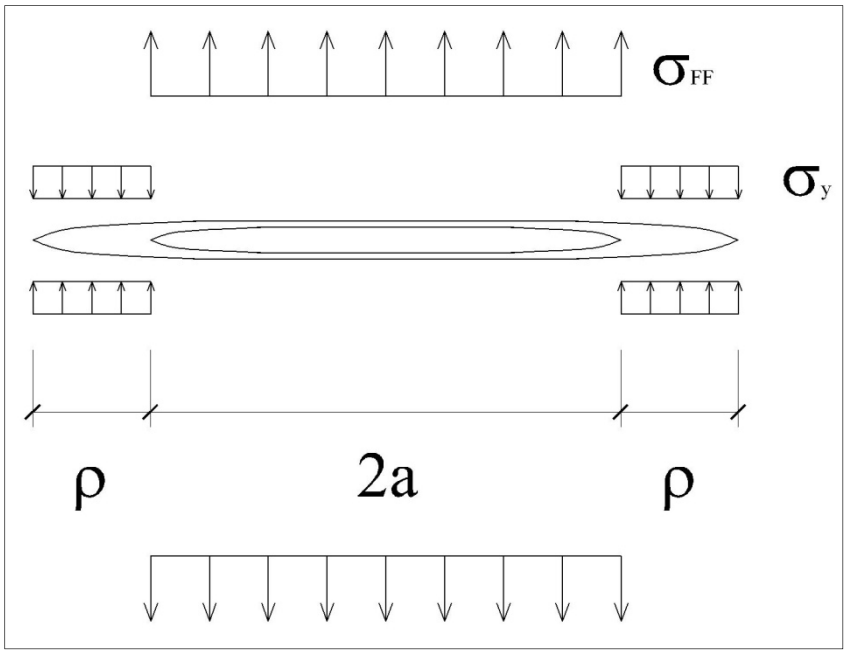

Fig. 6.1 – Dugdale's mode I crack

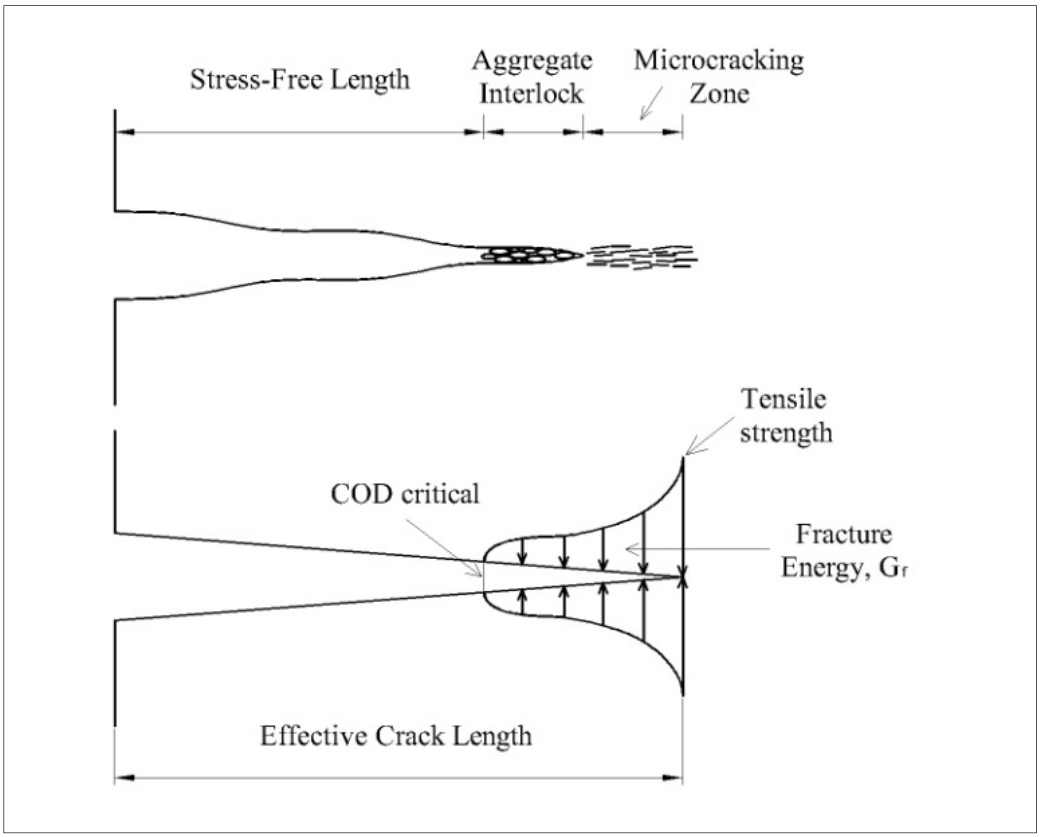

Fig. 6.2 – Fictitious crack model

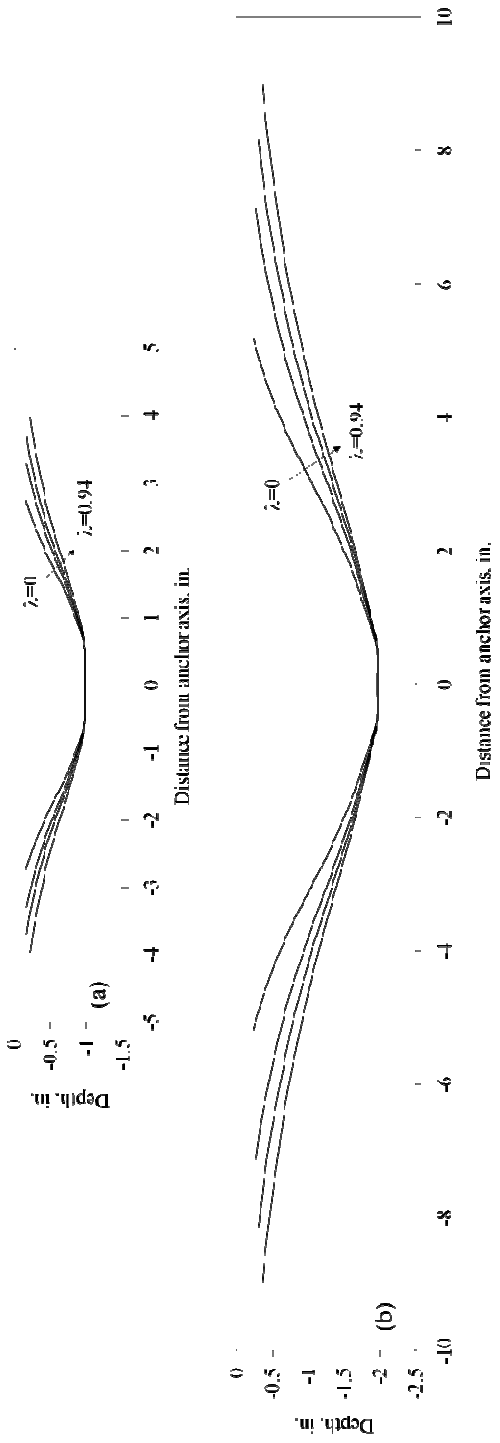

Fig. 6.3 – Predetermined LEFM crack profiles used for the NLFM simulations (Experiments part I); (a) $d/c = 1$ and $\beta = 0.3$; (b) $d/c = 2$ and $\beta = 0.6$

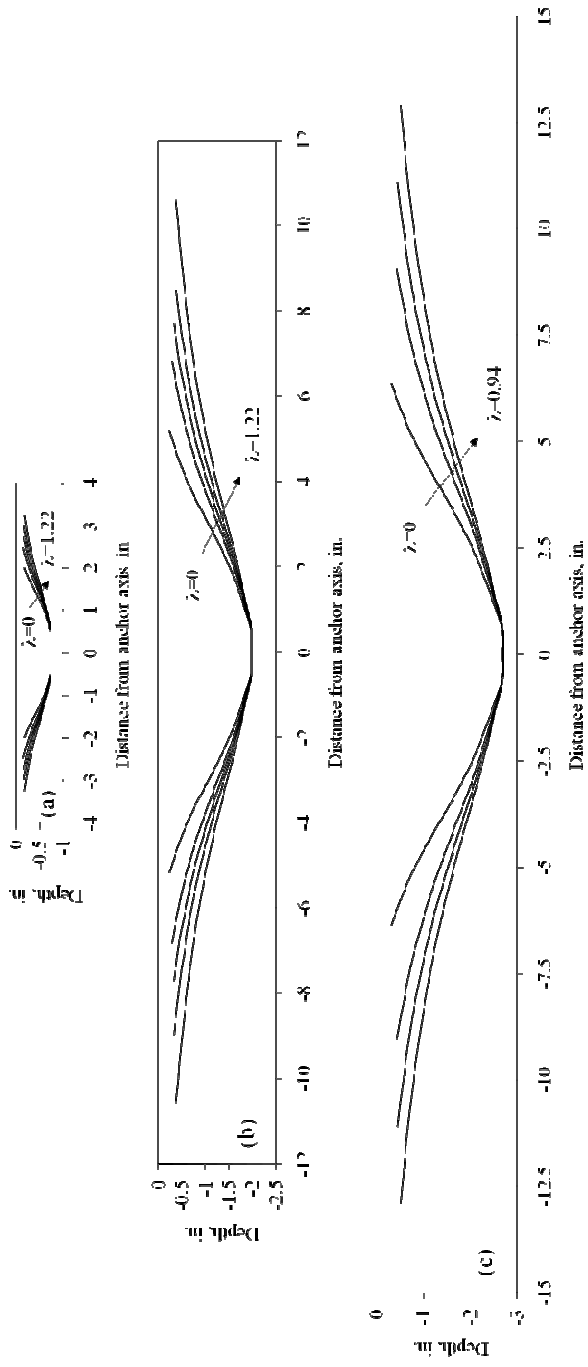

Fig. 6.4 – Predetermined LEFM crack profiles used for the NLFM simulations (Experiments part II); (a) $d/c = 0.75$ and $\beta = 0.31$; (b) $d/c = 2$ and $\beta = 0.82$; (c) $d/c = 2.75$ and $\beta = 1.13$

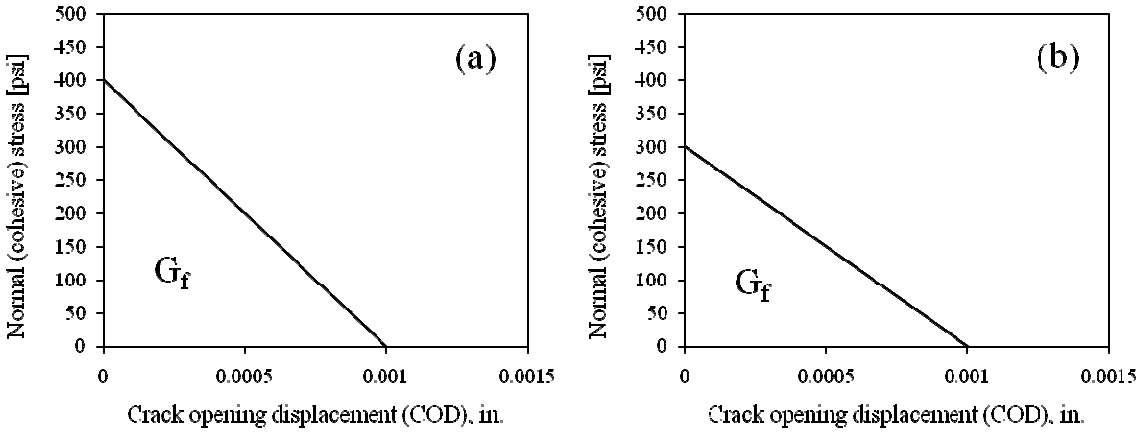

Fig. 6.5 – Constitutive law used for cohesive elements along LEFM predetermined crack paths; (a) Experiments part I; (b) Experiments part II

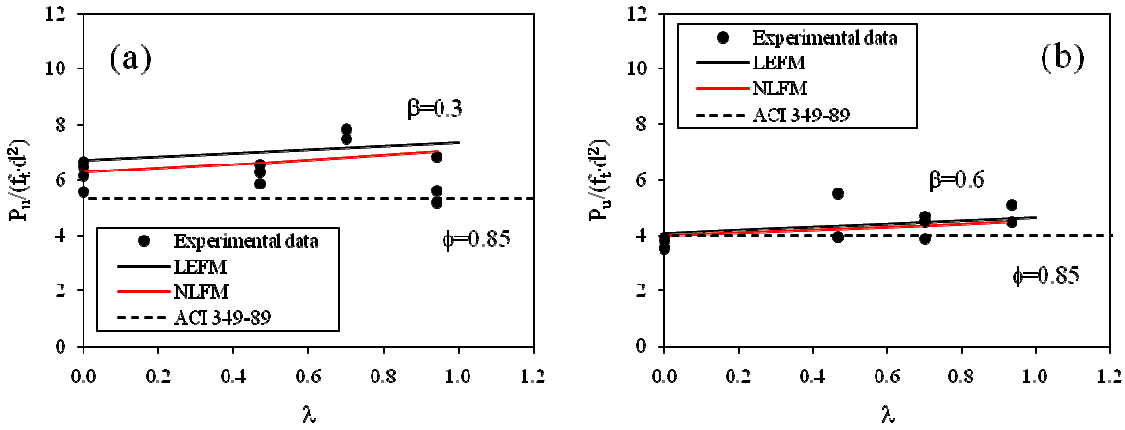

Fig. 6.6 – Normalized ultimate load carrying capacities as function of prestress;

Experiments, Part I; (a) $d/c=1$; (b) $d/c=2$

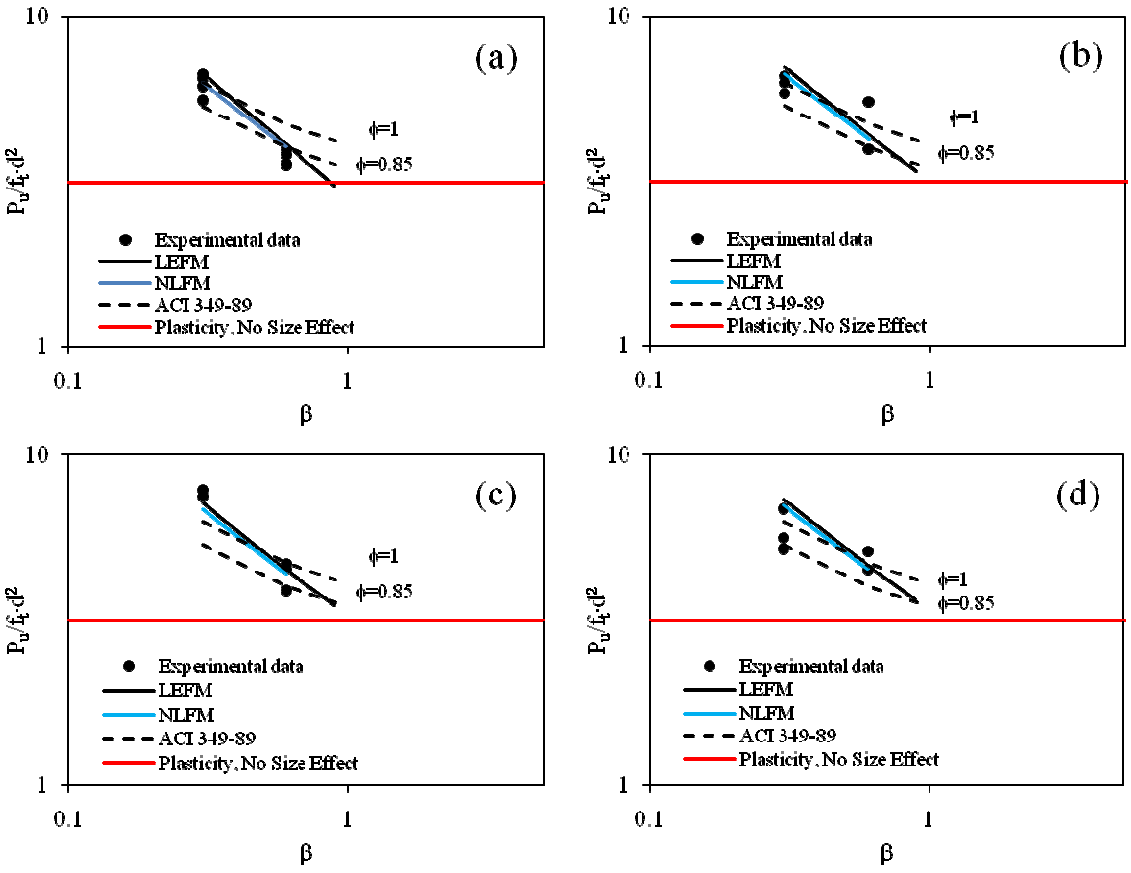

Fig. 6.7 – Log-log scale plot of the brittle-to-ductile transition for the pullout failure strength: comparison between experimental data and theoretical bounds (LEFM, NLFM, and Plasticity); (a) $\lambda = 0$; (b) $\lambda = 0.47$; (c) $\lambda = 0.7$; (d) $\lambda = 0.94$

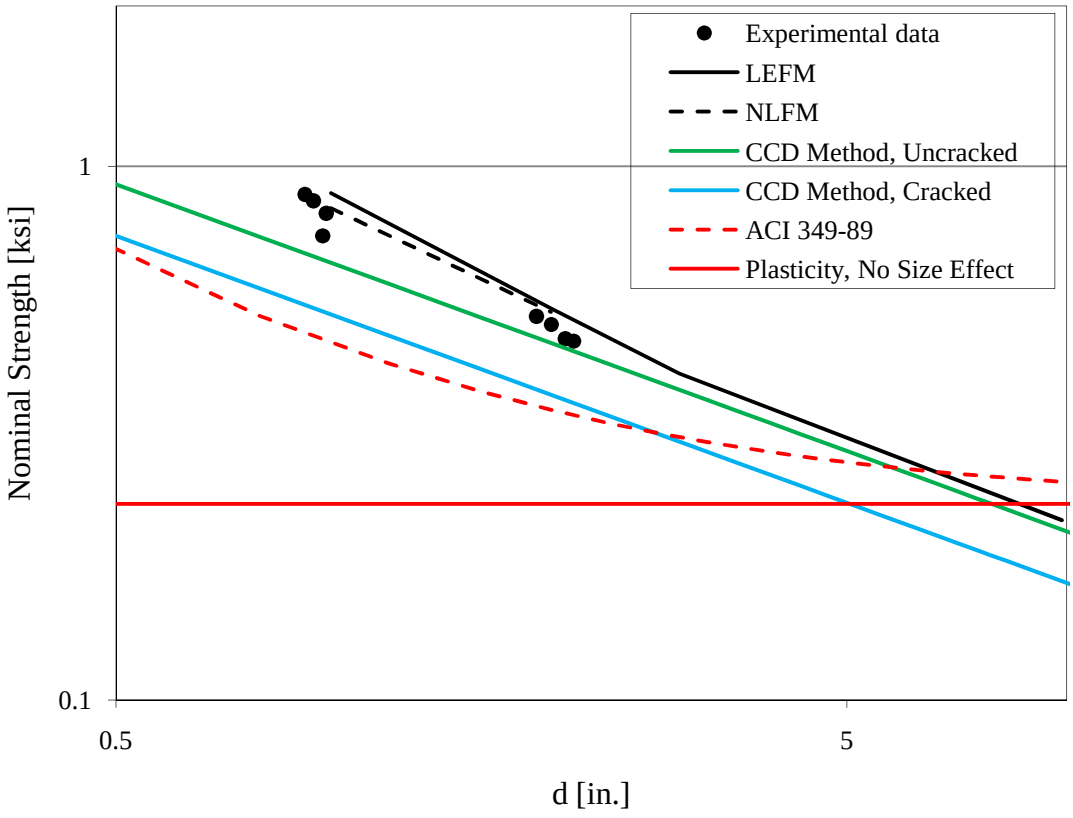

Fig. 6.8 – Log-log plot of nominal pullout strength as a function of the embedment depth for the embedment depths investigated: comparison of available design formulas and finite element model predictions; $\lambda = 0$

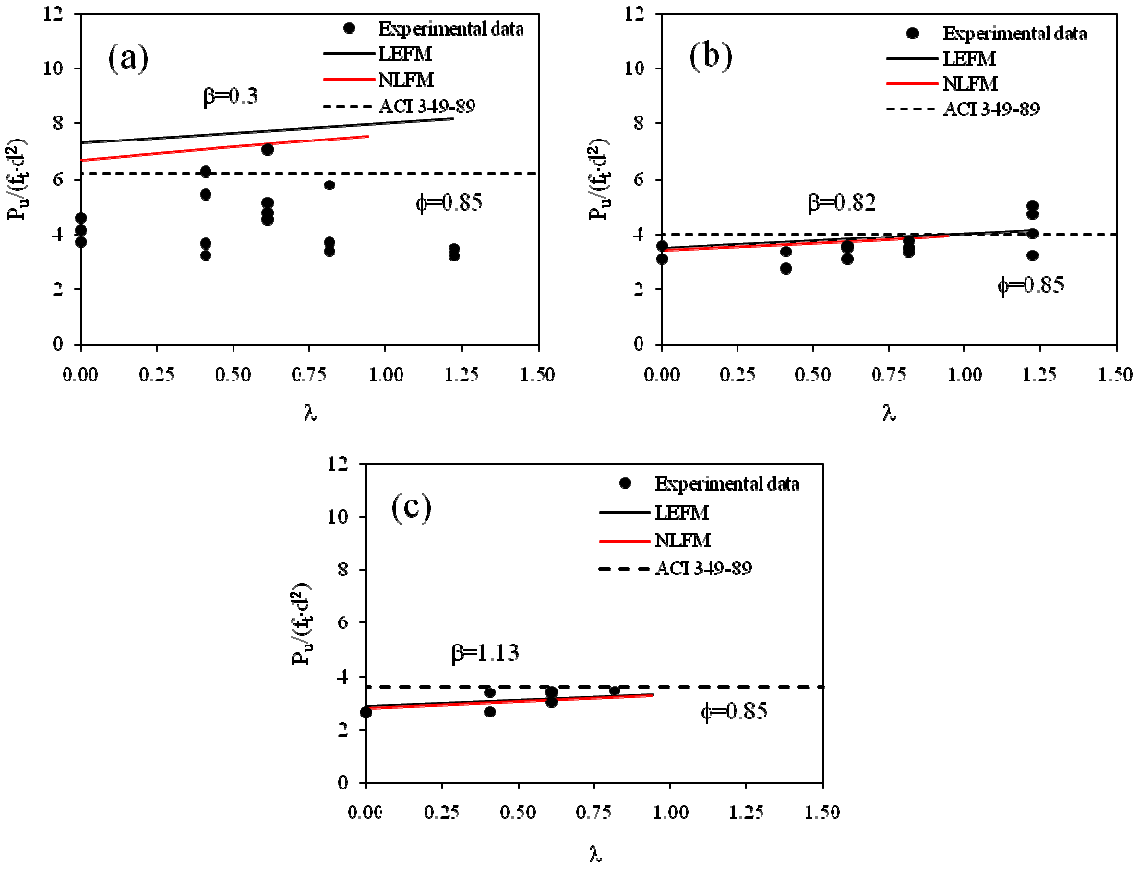

Fig. 6.9 – Normalized ultimate load carrying capacities as function of prestress; Experiments, Part II; (a) $d/c = 0.75$; (b) $d/c = 2$; (c) $d/c = 2.75$

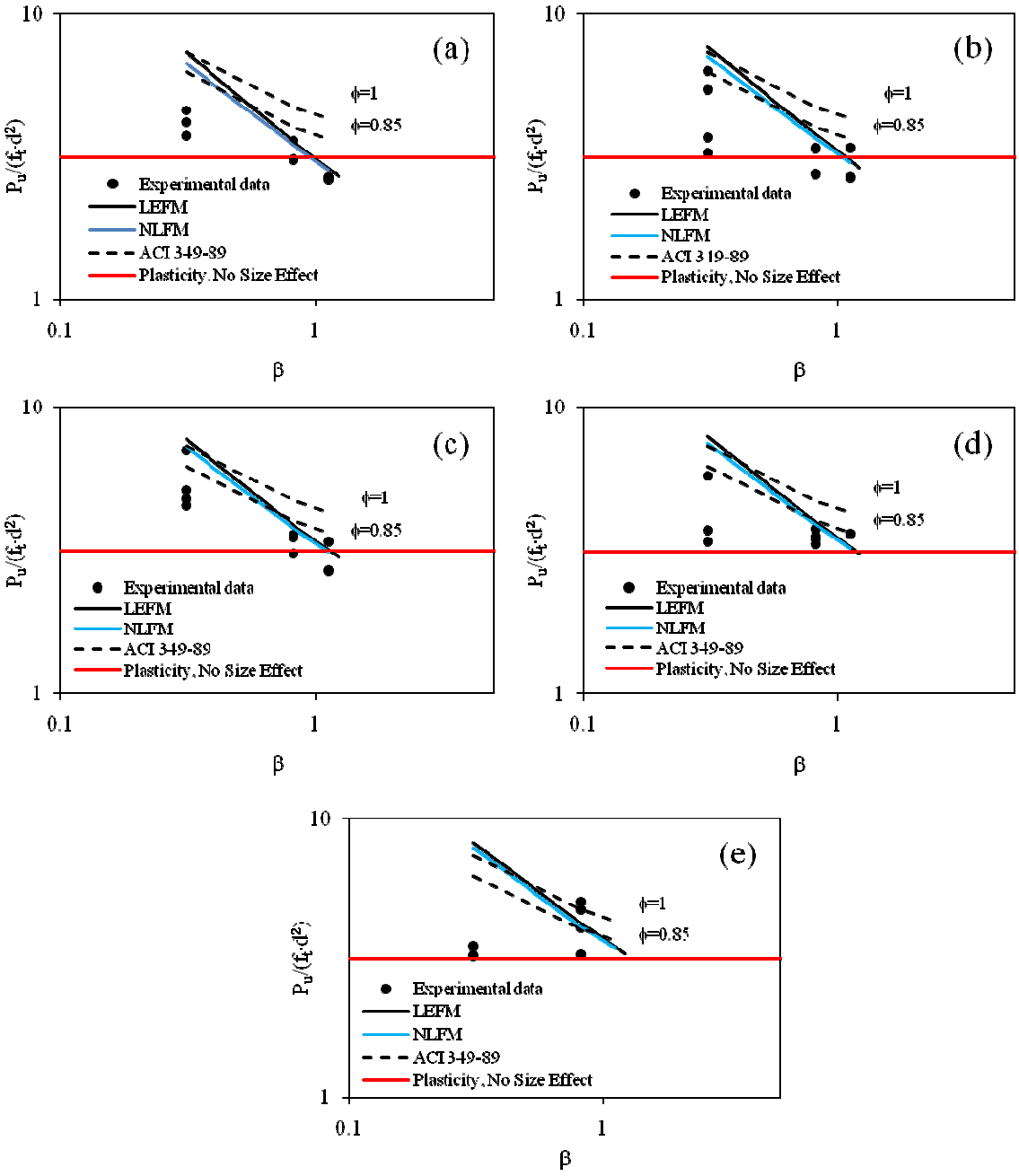

Fig. 6.10 – Log-log scale plot of the brittle-to-ductile transition for the pullout failure strength: comparison between experimental data and theoretical bounds (LEFM, NLFM, and Plasticity); (a) $\lambda = 0$; (b) $\lambda = 0.41$; (c) $\lambda = 0.61$; (d) $\lambda = 0.81$; (e) $\lambda = 1.22$

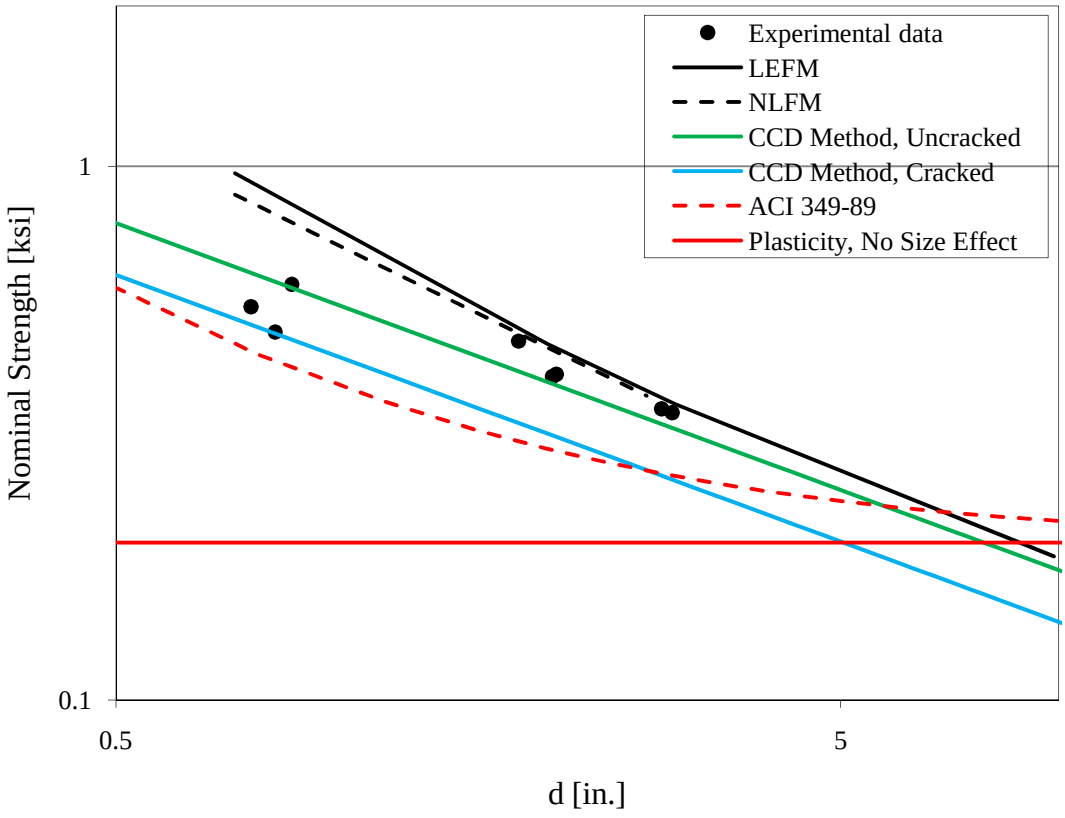

Fig. 6.11 – Log-log plot of nominal pullout strength as a function of the embedment depth for the embedment depths investigated: comparison of available design formulas and finite element model predictions; $\lambda = 0$

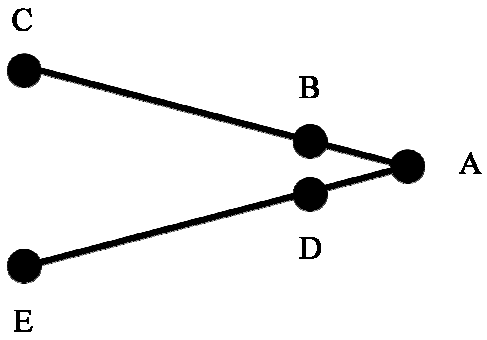

Fig. 6.12 – Nodal lettering for stress intensity factors computation (ABCDE, crack tip nodes; BD, quarter-point nodes; A, crack tip

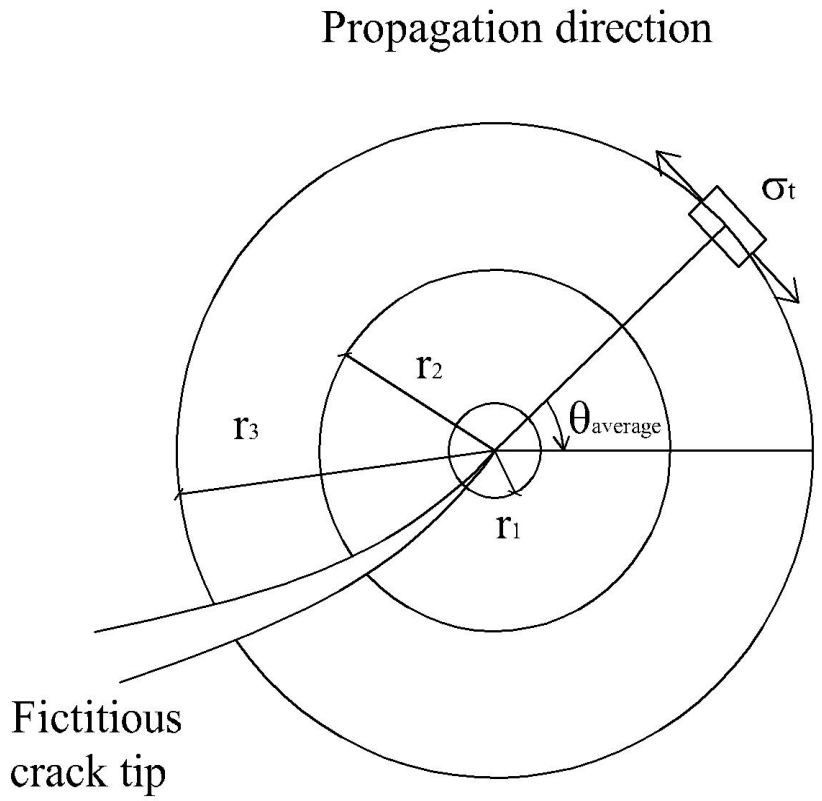

Fig. 6.13 – Computation of the crack propagation direction by the use of the maximum hoop stress criterion

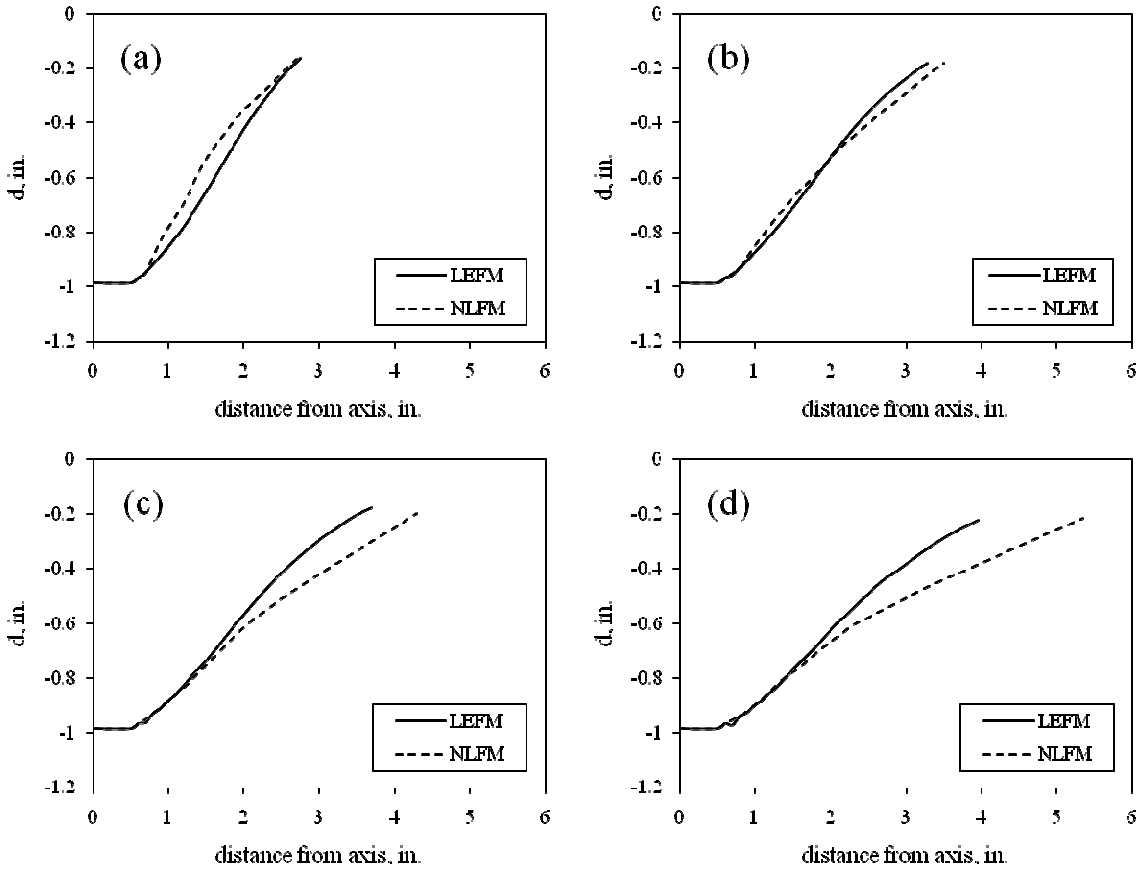

Fig. 6.14 – Comparison between LEFM and NLFM fracture profile predictions;

Experimental part I; $d/c = 1$ and (a) $\lambda = 0$, (b) $\lambda = 0.47$, (c) $\lambda = 0.7$, (d) $\lambda = 0.94$

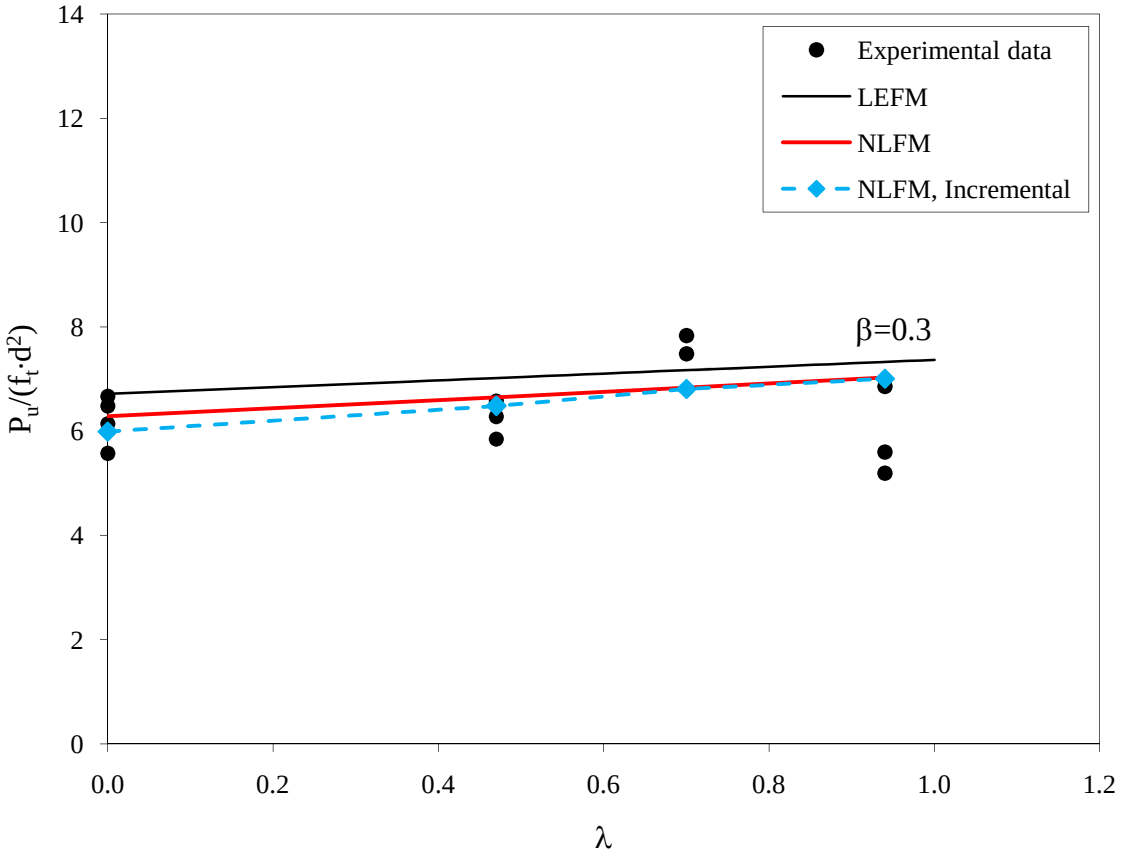

Fig. 6.15 – Normalized ultimate load carrying capacities as function of prestress: comparison of results obtained from NLFM incremental analyses and NLFM with cohesive elements along predefined crack trajectories; Experiments, Part I; $d/c = 1$

CHAPTER 7

DESIGN RECOMMENDATIONS, CONCLUSIONS AND SUGGESTIONS FOR FUTURE RESEARCH

7.1 Design Recommendations

The actual design code provisions to predict the capacity of headed anchors embedded in an unstressed concrete matrix can be expressed as

$$P_{u,CCD} = k_c \cdot \sqrt{f'_c} \cdot d^{3/2} \tag{7.1}$$

where k_c is taken equal to 30 for uncracked concrete and 24 for cracked concrete. A formula that takes into account for the presence of compressive stresses can be formulated by combining Eqs. 7.1 and 2.11, to give the following

$$P_u = k_c \cdot \sqrt{f'_c} \cdot d^{3/2} + 0.53\sigma_c d^2 \tag{7.2}$$

For $1 \le d/c \le 2.75$ and $0 \le \lambda \le 1.2$, an accurate fit of the LEFM predictions and the experimental evidence to the proposed Eq. 7.2 leads to the following, more practical, design formula

$$P_u = (k_c + 0.015 \cdot \sigma_c) \cdot \sqrt{f'_c} \cdot d^{3/2} \tag{7.3}$$

Where P_u is expressed in lb, and σ_c, f'_c are expressed in psi.

Being based on Eqs. 7.1 and 7.2, the proposed formula for the capacity of headed anchors in a compressively stressed concrete matrix represents a conservative approach and a lower bound for shallow anchors.

7.2 Conclusions

In the present study a fracture mechanics approach was applied to investigate the pullout capacities of headed anchors embedded in a prestressed (tension and compression) matrix material. From the results if this investigation, the following conclusions can be drawn:

- For all the embedment depths investigated, excluding the very shallow case $d/c = 0.75$, linear elastic fracture mechanics represents a very accurate approach to predict the capacities of headed anchors embedded in unstressed and stressed concrete matrices. The introduction of toughening mechanisms and non-linear deformations in the vicinity of the crack tip (nonlinear elastic fracture mechanics) provides results very similar, if not coincident, to the linear case. This means that crack propagation and ultimate load capacities are governed by the strongest possible concrete's effect of size. This validates all the previous studies according to which the correct dependence of the anchor's capacity on the embedment depth is $d^{3/2}$, shows that LEFM is valid for all length scales up to $d/c = 1$ and no transition between plasticity and LEFM exist;
- When compressive stresses are applied to the concrete matrix, the numerical models conservatively predict an increase in anchors' capacities equal to about 10% with respect to the unconfined case for typical practical values of $\lambda \approx 0.5$, suggesting that the effect of prestress is beneficial and that the actual code provisions (based on the CCD method) might be accordingly modified (Eq. 7.3);

- When tensile stresses are applied to the concrete matrix, the capacities of the anchors decrease. Depending upon the values of the brittleness number, β, the decrease in capacity is between 12 to 20% when $\lambda \approx -1$. This corroborates the necessity to use a reduced k_c factor in the CCD based formula (Eq. 7.1) to take (conservatively) into account for a reduction of capacity of about 25% in cracked concrete;
- When extremely shallow embedment depths are considered ($d/c = 0.75$), the fracture occurs within a region whose size is approximately equal to that of the aggregates, so that a deterministic continuum theory does not seem to be applicable;
- The fact that ACI 318 and ACI 349 provide a lower bound for $d/c \leq 2$ suggests that the effects shown in this study might have been empirically observed by others;
- The application of compressive biaxial stresses to the concrete matrix represents a completely novel field of investigation. It is noted that, because of geometric and stability issues of the concrete matrix, one of the major limits is that very large compressive loads (in this study, up to about 230 kips) are generally required to reach relatively small values of stress.
- Fracture mechanics is a very useful tool and show its applicability to problems primarily governed by the propagation of finite cracks. In addition to this, the present study demonstrates that a very simple two-dimensional axisymmetric discrete crack finite element model is capable of capturing the experimental evidence (especially in terms of ultimate load carrying capacities);

7.3 Future Research

Based on the results obtained in this study, the following recommendations are proposed:

- In the attempt to validate the proposed design formula and observe its applicability to more practical applications (i.e., small edge distances, group of anchors, shear loads, cyclic loads, etc.) more tests are recommended;
- Experimental tests involving the application of tensile stresses without keeping the predetermined crack widths constant are recommended to investigate the real effect of tension fields on the anchors' capacities (i.e., bending tests with anchors located in the tension zone);
- The two-dimensional axisymmetric finite element model showed its limits in capturing the experimentally obtained load-versus displacement curves. A more accurate test setup were the load point displacement, Δ, is measured at the anchors' head location is suggested. Other factors that include radial cracking and bending of the concrete surface during the pullout tests should be considered. Eventually, a more refined three-dimensional finite element model including radial cracking and concrete smeared cracking behavior should be considered;
- Additional testing is recommended for the investigation of the very shallow case where $d/c = 0.75$. Specifically, experiments involving the use of a larger value of d are recommended. In addition, analytical studies to investigate the effect of prestress and the possible surface instabilities that might arise when dealing with such shallow anchors are suggested.

REFERENCES

1. Eligehausen, R., Mallée, R., Silva, J., (2006). "Anchorage in concrete construction." Ernst and Sohn publishers.

2. Asmus, J., Eligehausen, R., (2001). "Design Method for Splitting Failure Mode of Fastenings." *Connections between steel and concrete: Stuttgart, Germany, 10-12 September 2001*, Edited by R. Eligehausen, Vol. 1, 80-90.

3. Asmus, J., Ozbolt, J., (2001). "Numerical and Experimental Investigations of the Splitting Failure Mode of Fastenings." *Connections between steel and concrete: Stuttgart, Germany, 10-12 September 2001*, Edited by R. Eligehausen, Vol. 1, 625-636.

4. Jensen, B., C., Braestrup, H., W., (1983). "Lok-tests determine the compressive strength of concrete." *Nordisk Betong*, Stockholm, Sweden, No. 2, 9-11.

5. ACI Committee 349, (1989). "Code requirements for nuclear safety." *Appendix B, Steel embedments, Manual of Concrete Practice, Part IV, ACI #349.1R*, American Concrete Institute, Detroit.

6. Eligehausen, R., Fuchs, W., and Mayer, B. (1987). "Loadbearing behavior of anchors fastenings in tension, Part 1." *Betonwerk und Ferigteil Technik*, No. 12, 826-832.

7. Eligehausen, R., and Fuchs, W., (1988). “Loadbearing behavior of anchor fastenings under shear, combined tension and shear or flexural loading.” *Betonwerk und Ferigteil Technik,* No. 2, 48-56.

8. Stone, W., C., and Carino, N. J., (1983). “Deformation and failure in large-scale pull-out tests.” *ACI Structural Journal,* Vol. 80, No. 6, 501-513.

9. Krenchel, H., and Shah, S., P., (1985). “Fracture analysis of the pullout test.” *Materials and Structures,* Vol. 18, No. 108, 439-446.

10. Klinger, R., E., Mendonca, J., A., (1982). “Tensile capacity of short anchor bolts and welded studs: a literature review.” *ACI Structural Journal,* Vol. 79, No. 27, 270-279.

11. Elfgren, L. (1998). “Round robin analyses and tests of anchor bolts in concrete structures.” *RILEM Technical Committee 90-FMA, Fracture mechanics of concrete applications*, RILEM.

12. Farrow, C., B., Klinger, R. E., (1995). “Tensile capacity of anchors with partial or overlapping failure surfaces: evaluation of existing formulas on an LRFD basis.” *ACI Structural Journal,* Vol. 92, No. 6, 698-710.

13. Farrow, C., B., Frigui, I., Klinger, R. E., (1996). “Tensile capacity of single anchors in concrete: evaluation of existing formulas on an LRFD basis.” *ACI Structural Journal*, Vol. 91, No. 2, 128-137.

14. Prestressed Concrete Institute (1999). “PCI Design Handbook.” 5th Edition, Chicago, Illinois.

15. Shaikh, A., F., and Yi, W., (1985). “In-place strength of welded headed studs.” *PCI Journal*, Vol. 30, No. 2, 56-81.

16. Ballarini, R., Shah, S., P., and Keer, L., M., (1985). “Failure characteristics of short anchor bolts embedded in a brittle material.” *Royal Society*, Proc., London, A404, 35-54.

17. Ballarini, R., Keer, L., M., Shah, S., P., (1987). “An analytical model for the pull-out of rigid anchors.” *International Journal of Fracture*, Vol. 33, No. 2, 75-94.

18. Bazant, Z., P., and Sener, S., (1988). “Size effect in pullout tests.” *ACI Materials Journal*, Vol. 85, 347-351.

19. Eligehausen, R., and Ozbolt, J., (1990). “Size effect in anchorage behavior.” In *Fracture behavior and design of materials and structures*, Vol. 2, Edited by D. Firrao,

Engineering Materials Advisory Services Ltd. (EMAS), Warley, West Mindlands, U.K., 721-727.

20. Ozbolt, J., Eligehausen, R., (1992). "Fastening elements in concrete structures – numerical solutions." *Fracture of Concrete and Rock*, Proc., 2nd International Conference, H. P. Rossmanith, ed. E&FN Spon, London, 527-547.

21. Bazant, Z., P., Ozbolt, J., and Eligehausen, R., (1994). "Fracture size effect: review of evidence for concrete structures." *ASCE Journal of Structural Engineering*, Vol. 120, 2377-2398.

22. Eligehausen, R., Sawade, G., (1989). "Analysis of anchorage behaviour (literature review)." *Fracture mechanics of concrete structures: from theory to applications*, Edited by L. Elfgren, Chapman & Hall, London, 263-280.

23. Ozbolt, J., Eligehausen, R., Reinhardt, H., W., (1999). "Size effect on the concrete cone pull-out load." *International Journal of Fracture*, Vol. 95, No. 1-4, 391-404.

24. Eligehausen, R. and Ožbolt, J. (1992). "Size effect in concrete structures." Edited by A. Carpinteri, *Application of Fracture Mechanics to Reinforced Concrete*, Elsevier Applied Science, Torino, Italy, 17-44.

25. Fuchs, W., Eligehausen, R., Breen, J., E., (1995). “Concrete capacity design (CCD) approach for fastening to concrete.” *ACI Structural Journal*, Vol. 92, No. 1, 73-94.

26. ACI Committee 318, (2002). “Building code requirements for structural concrete (ACI 318-02) and Commentary (318R-02).” *Appendix D, Anchoring to concrete*, American Concrete Institute, Farmington Hills, Michigan.

27. CEB, (1997). “Design of fastenings in concrete, design guide.” Comité Euro-International du Beton, Thomas Telford Services Ltd., London.

28. ACI Committee 318, (2008). “Building code requirements for structural concrete (ACI 318-08) and Commentary (318R-08).” *Appendix D, Anchoring to concrete*, American Concrete Institute, Farmington Hills, Michigan.

29. ACI Committee 349, (2006). “Code requirements for nuclear safety related concrete structures (ACI 349-06) and Commentary (349R-06).” *Appendix D, Anchoring to concrete*, American Concrete Institute, Farmington Hills, Michigan.

30. Lee, N., H., Kim, K., S., Bang, C., J., and Park, K., R. (2007). “Tensile headed anchors with large diameter and deep embedment in concrete.” *ACI Structural Journal*, Vol. 104, No. 4, 479-486.

31. Primavera, E., J., Pinelli, J., P., and Kalajian, E., H., (1997). “Tensile behavior of cast-in-place and undercut anchors in high-strength concrete.” *ACI Structural Journal*, Vol. 94, No. 5, 583-594.

32. Cattaneo, S., (2007). “Wedge-type expansion anchors in high-performance concrete.” *ACI Structural Journal*, Vol. 104, No. 2, 191-198.

33. Eligehausen, R., Balogh, T., (1995). “Behavior of fasteners loaded in tension in cracked reinforced concrete.” *ACI Structural Journal*, Vol. 92, No. 3, 365-379.

34. Eligehausen, R., Mattis, L., Wollmershauser, R., Hoehler, M., (2004). “Testing anchors in cracked concrete.” *Concrete International*, Vol. 26, No. 7, 66-71.

35. Baran, E., Schultz, A., E., French, C., E., (2006). “Tension tests on cast-in-place inserts: The influence of reinforcement and prestress.” *PCI Journal*, Vol. 51, No. 5, 88-108.

36. Cherepanov, G., P., (1979). “Mechanics of brittle fracture.” McGraw-Hill, New York.

37. Bazant, Z., P., Planas, J., (1998). “Fracture and size effect in concrete and other quasibrittle materials.” CRC Press.

38. Carpinteri, A., (1982). “Notch sensitivity in fracture testing of aggregate materials.” *Engineering Fracture Mechanics*, Vol. 16, No. 4, 467-481.

39. Elfgren, L., Ohlsson, U., (1992). “Anchor bolts modeled with fracture mechanics.” In *Application of fracture mechanics to reinforced concrete*, Edited by A. Carpinteri, Elsevier Applied Science, London, 267-283.

40. Irwin, G., R., (1957). “Analysis of stresses and strains near the end of a crack traversing a plate.” *Journal of Applied Mechanics*, Vol. 24, 361–364.

41. Vogel, A., Ballarini, R., (1999). “Ultimate load capacities of plane and axisymmetric headed anchors.” *Journal of Engineering Mechanics*, Vol. 125, No. 11, 1276-1279.

42. FRANC-2D, (1997). Cornell Fracture Group Home Page, Cornell University, Ithaca, NY. Available at: http://www.cfg.cornell.edu/software/franc2d_casca.htm

43. Barsoum, R., S., (1976). “On the use of isoparametric finite elements in linear fracture mechanics.” *International Journal for Numerical Methods in Engineering*, Vol. 10, No. 1, 25-37.

44. Broek, D., (1986). “Elementary engineering fracture mechanics.” Martinus Nijhoff Publishers.

45. ASTM C31 / C31M (2002). “Standard Practice for Making and Curing Concrete Test Specimens in the Field.” *ASTM International*, West Conshohocken, PA.

46. ASTM C496 / C496M (1996). “Standard Test Method for Splitting Tensile Strength of Cylindrical Concrete Specimens.” *ASTM International*, West Conshohocken, PA.

47 Shah, S., P., Swartz, S., E., Ouyang, C., (1995). “Fracture mechanics of concrete: applications of fracture mechanics to concrete, rock, and other quasi-brittle materials.” John Wiley & Sons, New York.

48. Dugdale, D., S., (1960). “Yielding of steel sheets containing slits.” *Journal of mechanics and physics of solids*, Vol. 8, 100-108.

49. Hillerborg, A., Modeer, M., and Petersson, P., E., (1976). “Analysis of crack formation and crack growth in concrete by means of fracture mechanics and finite elements.” *Cement and Concrete Research*, Vol. 6, 773-782.

50. Hillerborg, A., (1985). “The theoretical basis of a method to determine the fracture energy G_f of concrete.” *Materials and Structures*, Vol. 18, 291-296.

51. Hillerborg, A., (1985). “Numerical methods to simulate softening and fracture of concrete.” In *Fracture Mechanics of Concrete: Structural Application and Numerical*

Calculation, Edited by Shih, G., C. and Di Tommasi, A., Martinus Nijhoff, Dordrecht, 141-170.

52. Ingraffea, A., R., (1977). "Discrete fracture propagation in rock: laboratory tests and finite element analysis." Doctoral thesis, University of Colorado, Boulder, CO.

53. ACI Committee 446, (1997). "Finite element analysis of fracture in concrete structures." and "Active report (446.3R-97)." American Concrete Institute, Farmington Hills, Michigan.

54. Peterson, P., E., (1981). "Crack growth and development of fracture zone in plain concrete and similar materials." Report No. TVBM-1006, Division of Building Materials, Lund Institute of Technology, Lund, Sweden.

55. Ingraffea, A., R., Saouma, V., (1984). "Numerical modeling of fracture propagation in reinforced and plain concrete." In *Fracture Mechanics of Concrete: Structural Application and Numerical Calculation*, Edited by Shih, G., C. and Di Tommasi, A., Martinus Nijhoff, Dordrecht, 171-225.

56. Bittencourt, T., N., Ingraffea, A., R., and Llorca, J., (1992). "Simulation of arbitrary, cohesive crack propagation." In *Fracture Mechanics of Concrete Structures*, Edited by Bazant, Z., P., Elsevier Applied Science, London, 339-350.

57. Gerstle, W., H., Partha, P., D., Prasad, N., N., V., Rahulkumar, P, and Ming., X. (1992). “Crack growth in flexural members – A fracture mechanics approach.” *ACI Structural Journal*, Vol. 89, No. 6, 617-625.

58. Bocca, P., Carpinteri, A., and Valente, S., (1991). “Mixed mode fracture of concrete.” *International Journal of Solids and Structures,* Vol. 27, 1139-1153.

59. Bocca, P., Carpinteri, A., and Valente, S., (1990). “Size effect in the mixed mode crack propagation: softening and snap-back instabilities.” *Engineering Fracture Mechanics*, Vol. 35, 159-170.

60. Bocca, P., Carpinteri, A., and Valente, S., (1992). “Fracture mechanics evaluation of anchorage bearing capacity in concrete.” In *Application of Fracture Mechanics to Reinforced Concrete*, Edited by Carpinteri, A., Elsevier Applied Science, London, 231-265.

61. Ingraffea, A., R., Linsbauer, H., and Rossmanith, H. (1989). “Computer simulation of cracking in large arch dam – Downstream side cracking.” In *Fracture of Concrete and Rock*, Edited by Shah, S., P., and Swartz, S., E., Springer-Verlag, New York, 334-342.

62. Wawrzynek, P., A., and Ingraffea, A., R., (1987). “Interactive finite element analysis of fracture processes: an integrated approach.” *Theoretical and Applied Fracture Mechanics*, Vol. 8, 137-150.

63. Hellier, A., K., Sansalone, M, Ingraffea, A., R., Carino, N., J., and Stone, W., C., (1987). “Finite element analysis of the pull-out test using a nonlinear discrete cracking approach.” *Cement, Concrete and Aggregates*, (ASTM), Vol. 9, No. 1, 20-29.

64. Xie., M., and Gerstle, W., (1995). “Energy-based cohesive crack propagation modeling.” *ASCE Journal of Engineering Mechanics*, Vol. 121, No. 2, 1349-1358.

65. Parks, D., M., (1974). “A stiffness derivative finite element technique for determination of crack tip stress intensity factors.” *International Journal of Fracture*, Vol. 10, No. 4, 487-502.

66. Hellen, T., K., (1975). “On the method of virtual crack extension.” *International Journal of Numerical Methods in Engineering*, Vol. 9, No. 1, 187-207.

67. Erdogan, F., and Shih, G., C., (1963). “On the crack extension in plate under in plane loading and transverse shear.’ *Journal of Basic Engineering*, Vol. 85, No. 4, 519-527.

68. Galvez, J., C., Elices, M., Guinea, G., V., Planas, J., (1998). “Mixed mode fracture of concrete under proportional and nonproportional loading.” *International Journal of Fracture*, Vol. 94, No. 3, 267-284.

69. Galvez, J., C., Cervenka, J., Cendon, D., A., Saouma, V., (2002). “A discrete crack approach to normal/shear cracking of concrete.” *Cement and Concrete Research*, Vol. 32, No. 10, 1567-1585.

70. Cendon, D., A., Galvez, J., C., Elices, M., Planas, J., (2000). “Modelling the fracture of concrete under mixed loading.” *International Journal of Fracture*, Vol. 103, No. 3, 293-310.

71. Wittmann, F., H., Roelfstra, P., E., Mihashi, H., (1987). “Influence of age of loading, water-cement ratio and rate of loading on fracture energy of concrete.” *Materials and Structures/Materiaux et Construction*, Vol. 20, No. 2, 103-110.

72. Inglis, C., E., (1913). “Stresses in a plate due to the presence of cracks and sharp corners.” *Transactions of the Institute of Naval Architects*, Vol. 55, pp. 219-241.

73. Irwin, G., R., (1948). “Fracture dynamics.” *Fracturing of Metals*, American Society for Metals, Cleveland, OH, pp. 147-166.

74. Irwin, G., R., (1957). “Analysis of stresses and strains near the end of a crack traversing a plate.” *Journal of Applied Mechanics*, Vol. 24, pp. 361-364.

75. Irwin, G., R. (1956). “Onset of fast crack propagation in high strength steel and aluminum alloys.” *Sagamore Research Conference Proceedings*, Vol. 2, pp. 289-305.

76. Anderson, T., L., (2005). “Fracture mechanics: fundamentals and applications.” Taylor and Francis, Boca Raton, FL.

77. Hussain, M., A., Pu, S., L., and Underwood, J., (1974). “Strain energy release rate for a crack under combined mode I and mode II.” *ASTM-STP-560*, pp. 2-28.

78. Sih, G., C., (1974). “Strain energy density factor applied to mixed mode fracture.” *International Journal of Fracture*, Vol. 10, No. 3, pp. 305-322.

APPENDIX A

A1.1 LEFM Concepts

Fracture mechanics is the branch of mechanics dedicated to the study of crack propagation in materials and structures. Most structures are not perfect but instead contain some defects. The presence of initial flaws such as cracks and voids, and their associated stress concentration effects, may cause a structure to fail under loads much smaller than the ones the structure was designed for, even for materials that are still in the elastic range. Clearly, the case is particularly alarming in large concrete structures, for human and environmental reasons.

The first formula developed to describe the stress field at the tip of an elliptical flaw in an infinite solid subjected to a uniform stress field was developed by Inglis [72] as

$$\sigma = \sigma_0 \cdot (1 + 2\frac{a}{b}) \tag{A1.1}$$

where σ is the stress at the tip of the flaw, σ_0 is the far field stress, and a, b are the axes of the ellipse (Fig. A1.1).

When the aspect ratio of the ellipse vanishes it was observed that stresses become singular at the tip of a crack. Irwin [73] noted that a real material cannot sustain an infinite stress and some yielding needs to occur in a zone near the crack tip. The region that yields is referred to as the process zone and accounts for other types of irreversible deformations such as microcracking, phase transformation, etc. that occur in other types of materials. If the process zone is small compared to other characteristic dimensions of the structure such as the crack length, the depth of a beam, or the depth of an anchor bolt,

small scale yielding (SSY) conditions hold and therefore despite the nonlinear effects in the immediate vicinity of the crack front, crack extension and stability are both dictated by the singular elastic stress field surrounding the process zone (Fig. A1.2).

In the case of an infinitely wide, cracked plate with crack length of $2a$ (note that the plates in Fig. A1.1 and A1.3 are identical when $a >> b$), the stress distribution is given by (Irwin [74])

$$\sigma(r) = \frac{K_I}{\sqrt{2\pi r}} \tag{A1.2}$$

where the coefficient K_I is called the opening-mode stress intensity factor. The stress distribution varies with $\frac{1}{\sqrt{r}}$, regardless of geometry and loading of the specimen. The details of the geometry and loading are reflected in K_I, which is found by solving the boundary value problem. Then crack extension is assumed when

$$K_I = K_{Ic} = \sigma\sqrt{\pi a} \tag{A1.3}$$

where the fracture toughness K_{Ic} is a material constant. The value of K_{Ic} can be related to the elastic strain energy released during crack propagation through the Irwin [75] relation

$$K_{Ic} = \sqrt{G_{Ic} E'} \tag{A1.4}$$

where $E = E'$ for plane stress.

In three dimensional problems, the deformation and stress field in the proximity of a crack tip are usually decomposed into three different modes (of loading): mode I is the opening or tension mode, mode II is the sliding or in-plane shear mode, mode III is the tearing or anti-plane shear mode. For 2D problems, the mode III condition does not

exist, and the formulations of the mode I and II stress intensity factors can be used for crack propagation and stability. In this latter case, the elastic stress distribution near a crack tip is shown in Table A1.1 (Anderson [76]).

A1.2 LEFM and The Finite Element Method

The numerical methods based on the finite element method (FEM) are generally classifieds into two groups: the “smeared crack approach” and the “discrete crack approach”. In the first method, the fracture is represented in a distributed manner and a large number of (theoretically) distributed “cracks” is distributed across the finite elements. The propagation of the cracks is usually simulated by reducing the stiffness and strength of the elements. The constitutive laws are non linear and cause difficulties and instabilities. The system of equations may become ill-posed, localization instabilities and spurious mesh sensitivity might also appear. Many nonlocal continuum models have been developed so far, but none gives a general solution to the problem.

The discrete approach is preferred when there is one main crack in the structure, which is the case represented by the pull-out type failure of headed anchors. In 2D problems, the LEFM concepts necessary to accomplish the discrete crack modeling are the stress intensity factors and the mixed mode interaction theories. FRANC-2D [42], a program that possesses automatic remeshing capabilities, has been implemented to solve discrete crack problems with finite elements and has been used in this study.

Among the methods developed to compute the stress intensity factors using the finite element method, the displacement correlation technique (Barsoum [43]) is most widely used. The basic idea of this method is to correlate the displacements at specific

locations with analytical solutions that are expressed in terms of the stress intensity factors. Special purpose elements (quarter-point singular elements) need to be used at the tip of a crack to accomplish the objective.

The theoretical displacement field for the opening mode around a crack tip (Fig. A1.4) is given as

$$u = \frac{K_I}{\mu}\left[\frac{r}{2\pi}\right]^{1/2} \cos\frac{\theta}{2}\left[1 - 2\nu + \sin^2\frac{\theta}{2}\right] \tag{A1.5}$$

for the horizontal displacements and

$$v = \frac{K_I}{\mu}\left[\frac{r}{2\pi}\right]^{1/2} \sin\frac{\theta}{2}\left[2 - 2\nu - \cos^2\frac{\theta}{2}\right] \tag{A1.6}$$

for the vertical displacements.

Setting $r = r_{a-b}$ and $\theta = 180$, it follows that along the crack surfaces

$$v_{b-a} = \frac{K_I}{\mu}\left[\frac{r_{a-b}}{2\pi}\right]^{1/2} (2 - 2\nu) \tag{A1.7}$$

If quarter-point finite elements are used to compute SIFs, a correlation between the displacements and the SIFs can be derived.

Using the relative shape functions, the displacements along the crack edges *abc* and *aed* (Fig. A1.4) become

$$v_{upper} = v_a + (-3v_a + 4v_b - v_c)\sqrt{\frac{r}{l}} + (2v_a - 4v_b + 2v_c)\frac{r}{l} \tag{A1.8}$$

along r_{a-b-c}, and

$$v_{lower} = v_a + (-3v_a + 4v_d - v_e)\sqrt{\frac{r}{l}} + (2v_a - 4v_d + 2v_e)\frac{r}{l} \tag{A1.9}$$

along r_{a-d-e}.

Subtracting (A1.8) from (A1.9), it follows that

$$v_{upper} - v_{lower} = \left[4(v_b - v_d) + (v_e - v_c)\right]\sqrt{\frac{r}{l}} + \left[4(v_b - v_d) + 2(v_c - v_e)\right]\frac{r}{l} \qquad \text{(A1.10)}$$

Solving equation (A1.6) for $\theta = 180(r_{a-b-c})$ and for $\theta = -180(r_{a-d-e})$, subtracting to obtain $v_{upper} - v_{lower}$, and equating the resulting expression to equation (A1.10), gives the following

$$K_I = \frac{\mu\sqrt{2\pi}}{\sqrt{r_{a-b-c}}(2-2\nu)}\left[4(v_b - v_d) + (v_e - v_c)\right] \qquad \text{(A1.11)}$$

for plane stress conditions. The same can be applied to plane stress and axisymmetry conditions, as well as for the in plane sliding mode.

Among all the available mixed-mode interaction theories, three of them (Erdogan and Shih [67], Hussain [77], and Sih [78]) have shown to be in good agreement with experimental evidence. In the present research, the maximum circumferential stress theory (Erdogan and Shih [67]) was used.

In this case, the crack is assumed to propagate in the direction for which the circumferential stress around the crack tip, $\sigma_{\vartheta\vartheta}$, is maximum. Expressing the stresses ahead of the crack tip as

$$\sigma_{\vartheta\vartheta} = \frac{1}{\sqrt{2\pi r}}\cos\left(\frac{1}{2}\vartheta\right)\left[K_I\cos^2\left(\frac{1}{2}\vartheta\right) - \frac{3}{2}K_{II}\sin(\vartheta)\right] \qquad \text{(A1.12)}$$

and

$$\tau_{r\vartheta} = \frac{1}{2\sqrt{2\pi r}}\cos\left(\frac{1}{2}\vartheta\right)\left[K_I\sin(\vartheta) + K_{II}\left((3\cos(\vartheta) - 1)\right]\right. \qquad \text{(A1.13)}$$

The maximum of $\sigma_{\vartheta\vartheta}$ corresponds to the direction which renders $\tau_{r\vartheta}$ zero, and consequently, the crack propagation angle, ϑ, can be expressed as

$$\vartheta = 2\tan^{-1}\left[\frac{1}{4}\frac{K_I}{K_{II}} \pm \frac{1}{4}\sqrt{\left(\frac{K_I}{K_{II}}\right)^2 + 8}\right] \tag{A1.14}$$

If it is assumed that the crack extension takes place when $\sigma_{\vartheta\vartheta}(\vartheta)$ has the same value as an equivalent mode I case, where $K = K_{Ic}$ and $\vartheta = 0$, then the following

$$K_{Ic} = K_I \cos^3\left(\frac{\vartheta}{2}\right) - 3K_{II}\cos^2\left(\frac{\vartheta}{2}\right)\sin\left(\frac{\vartheta}{2}\right) \tag{A1.15}$$

represents the condition for crack extension. It is worth observing that this criterion, to first order, implies the condition of local symmetry and that the crack initiation is locally under mode I conditions.

Table A1.1 – Stress Fields Ahead of a Crack Tip for Mode I and Mode II Conditions (Note that r is the radial distance from the crack tip, ϑ is the angle with respect to a line parallel to the crack, and K_I and K_{II} are the Mode I and Mode II stress intensity factors

σ_{xx}	$\frac{K_I}{\sqrt{2\pi r}}\cos\left(\frac{\vartheta}{2}\right)\left[1-\sin\left(\frac{\vartheta}{2}\right)\sin\left(\frac{3\vartheta}{2}\right)\right]$	$-\frac{K_{II}}{\sqrt{2\pi r}}\sin\left(\frac{\vartheta}{2}\right)\left[2+\cos\left(\frac{\vartheta}{2}\right)\cos\left(\frac{3\vartheta}{2}\right)\right]$
σ_{yy}	$\frac{K_I}{\sqrt{2\pi r}}\cos\left(\frac{\vartheta}{2}\right)\left[1+\sin\left(\frac{\vartheta}{2}\right)\sin\left(\frac{3\vartheta}{2}\right)\right]$	$\frac{K_{II}}{\sqrt{2\pi r}}\sin\left(\frac{\vartheta}{2}\right)\cos\left(\frac{\vartheta}{2}\right)\cos\left(\frac{3\vartheta}{2}\right)$
τ_{xy}	$\frac{K_I}{\sqrt{2\pi r}}\cos\left(\frac{\vartheta}{2}\right)\sin\left(\frac{\vartheta}{2}\right)\cos\left(\frac{3\vartheta}{2}\right)$	$\frac{K_{II}}{\sqrt{2\pi r}}\cos\left(\frac{\vartheta}{2}\right)\left[1-\sin\left(\frac{\vartheta}{2}\right)\sin\left(\frac{3\vartheta}{2}\right)\right]$
σ_{zz}	0 (Plane stress) $\nu(\sigma_{xx}+\sigma_{yy})$ (Plane strain)	0 (Plane stress) $\nu(\sigma_{xx}+\sigma_{yy})$ (Plane strain)
τ_{xz} and τ_{yz}	0	0

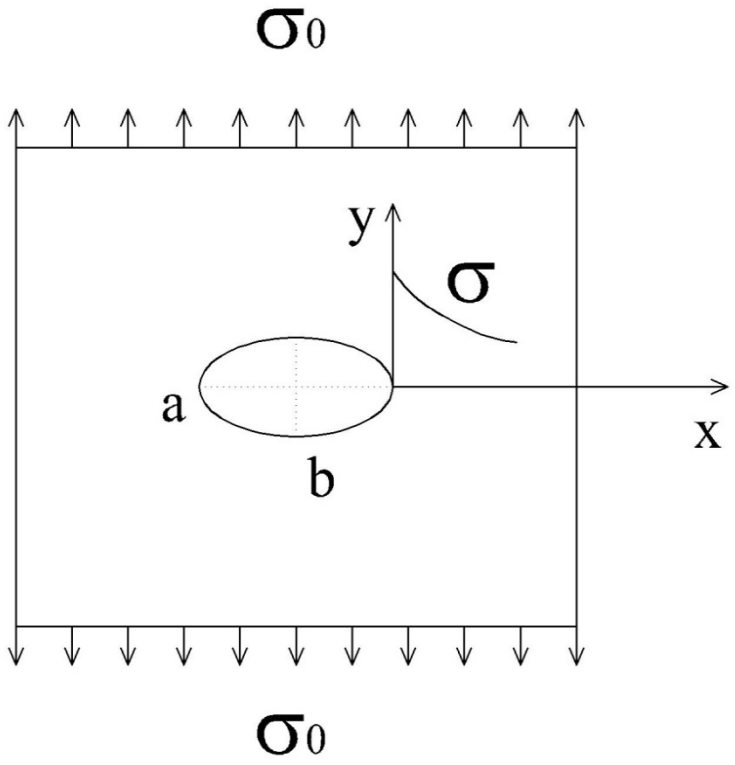

Fig. A1.1 – Ellipsoidal discontinuity in an infinite plate

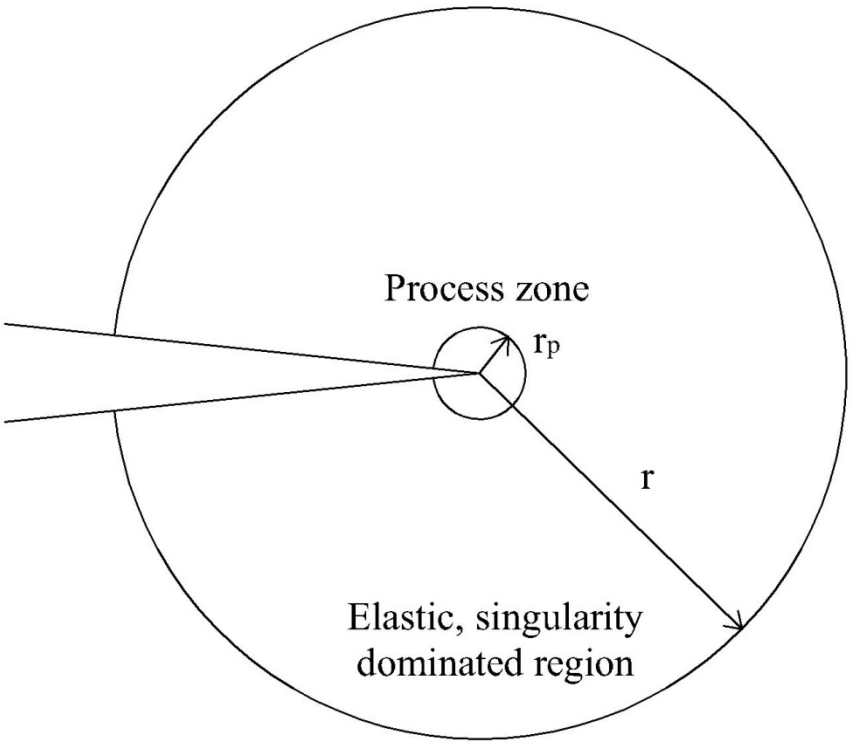

Fig. A1.2 – LEFM fundamental concept

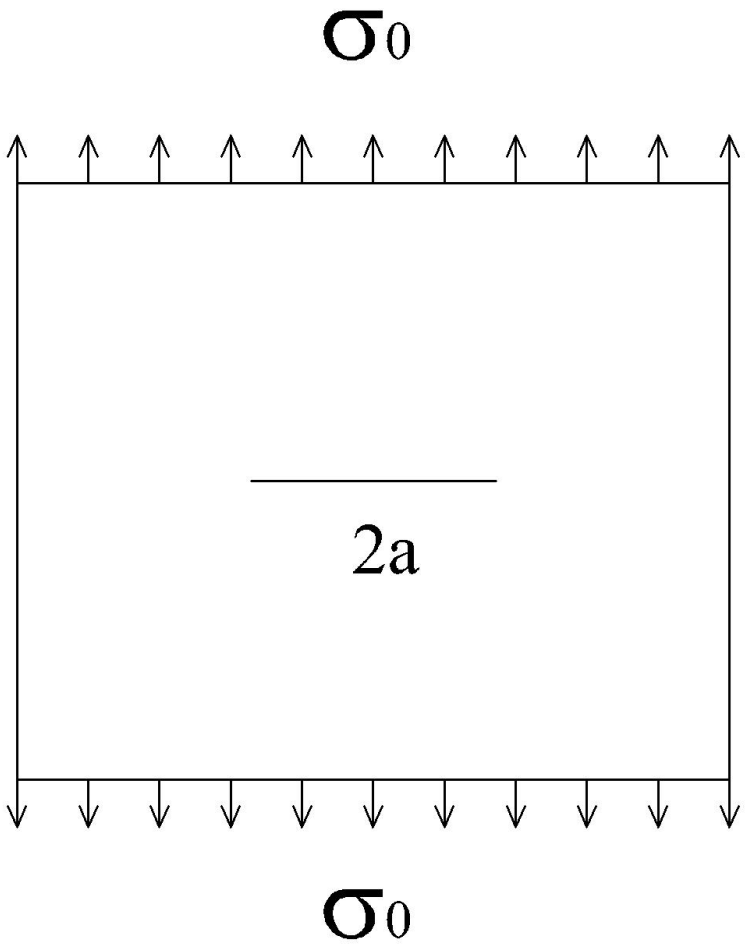

Fig. A1.3 – Cracked infinite plate

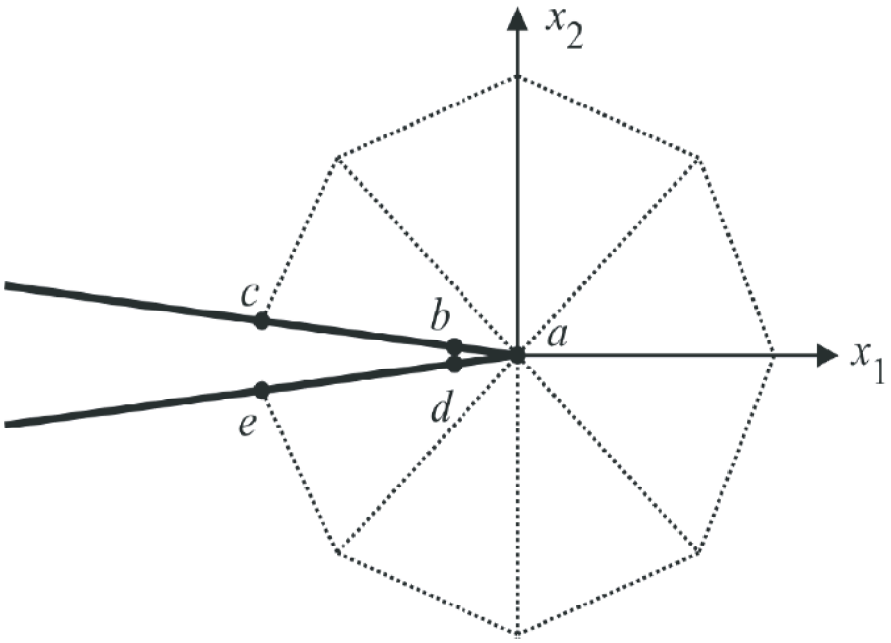

Fig. A1.4 – Crack tip detail including finite singular elements

APPENDIX B

In this Appendix, the experimental results in terms of ultimate load capacities, load versus displacement curves, and crack profiles are shown. Results are expressed in dimensional and non dimensional forms.

B1.1 Experiments: Part I

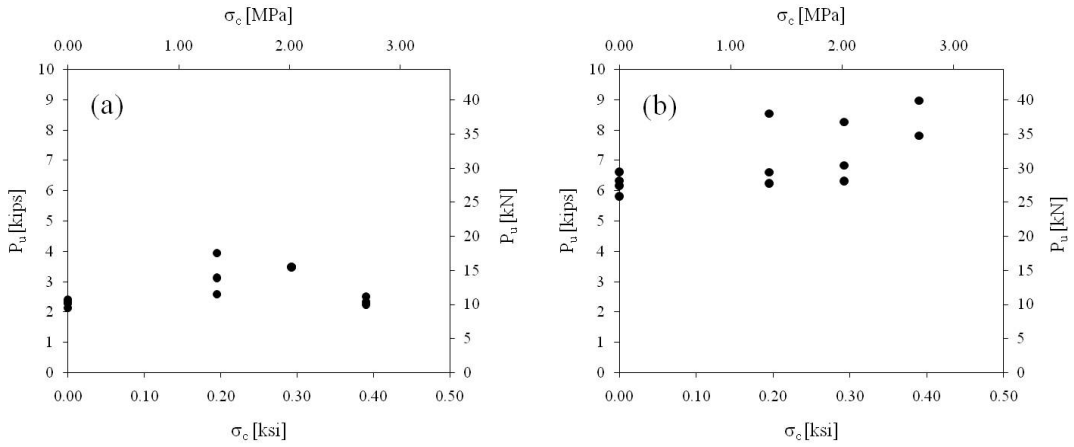

Fig. B1.1 – Ultimate load carrying capacities as function of prestress; (a) $d/c = 1$; (b) $d/c = 2$

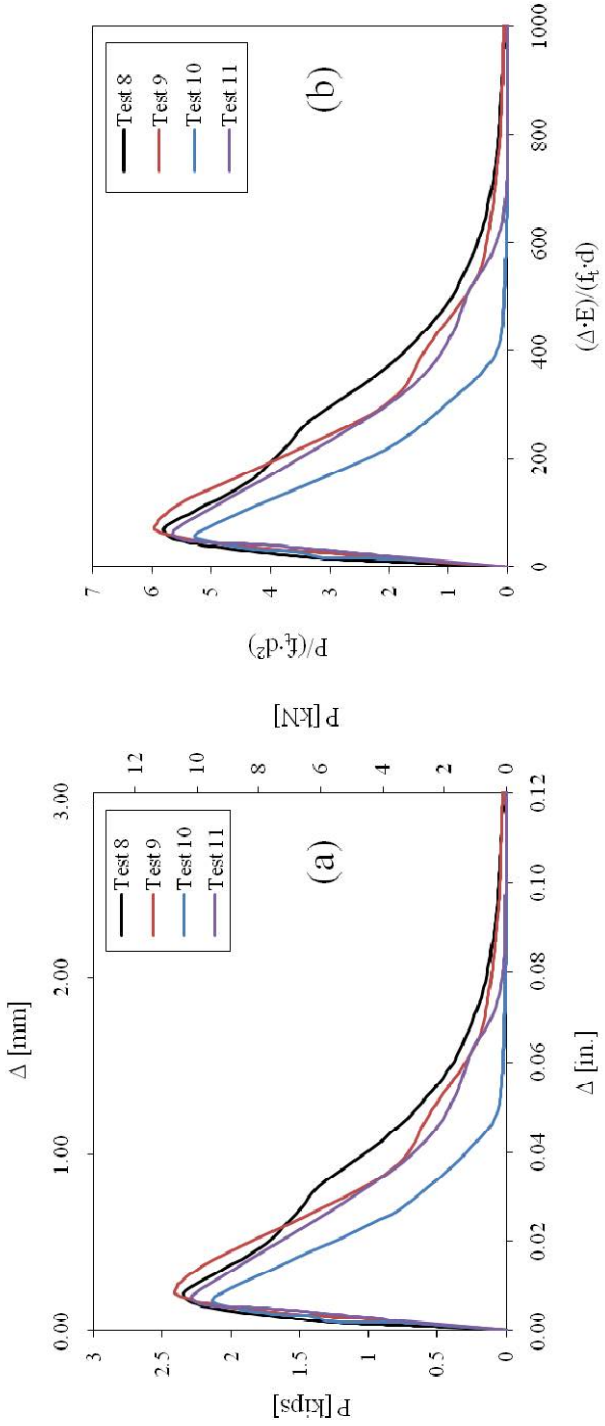

Fig. B1.2 – Load versus displacement curves, $d/c = 1,\ \lambda = 0$; (a) Dimensional, (b) Nondimensional

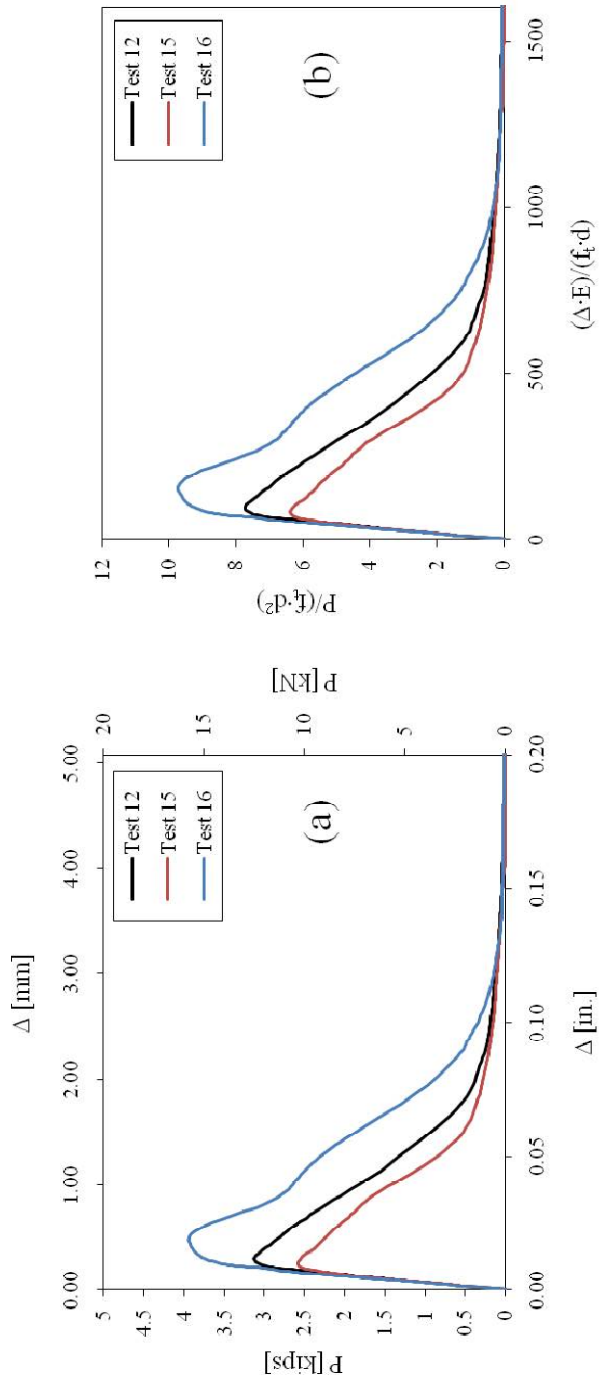

Fig. B1.3 – Load versus displacement curves, $d/c = 1$, $\lambda = 0.47$; (a) Dimensional, (b) Nondimensional

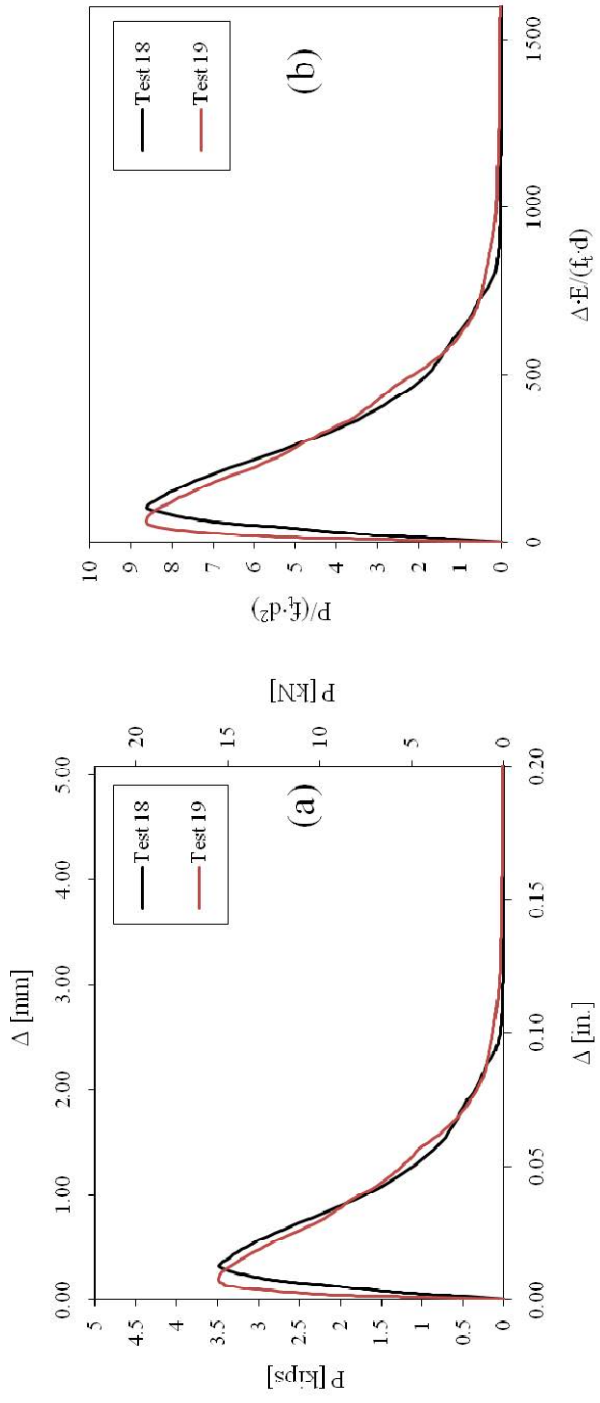

Fig. B1.4 – Load versus displacement curves, $d/c = 1$, $\lambda = 0.7$; (a) Dimensional, (b) Nondimensional

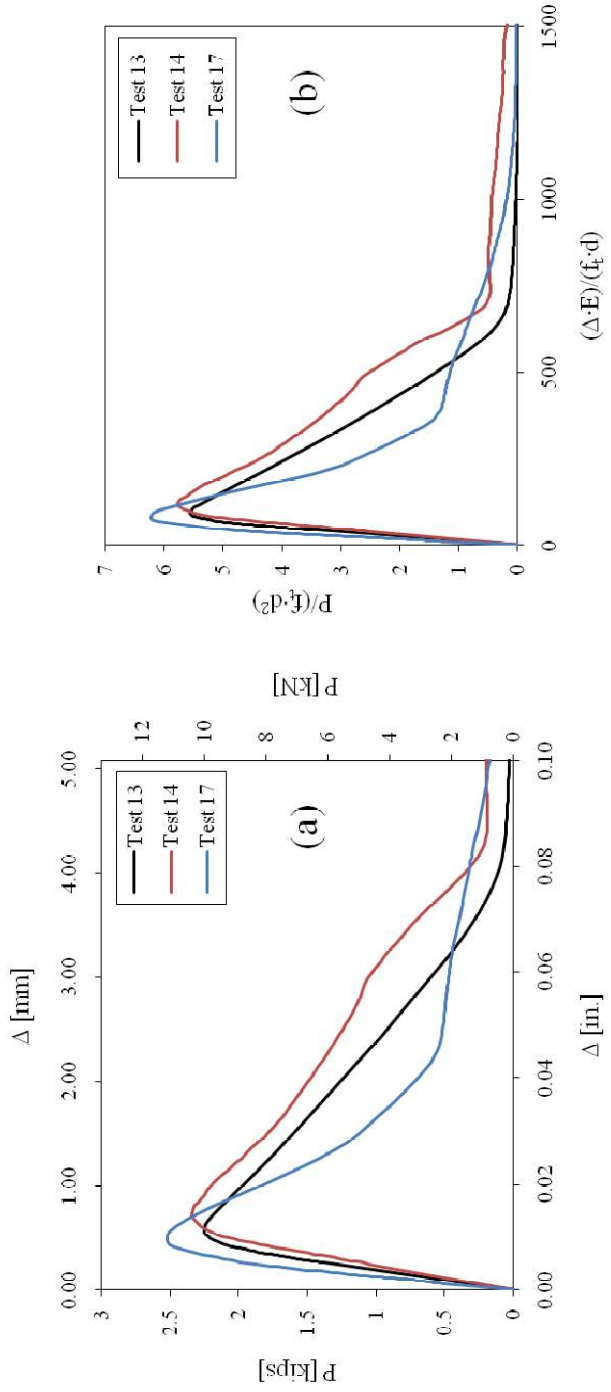

Fig. B1.5 – Load versus displacement curves, $d/c = 1$, $\lambda = 0.94$; (a) Dimensional, (b) Nondimensional

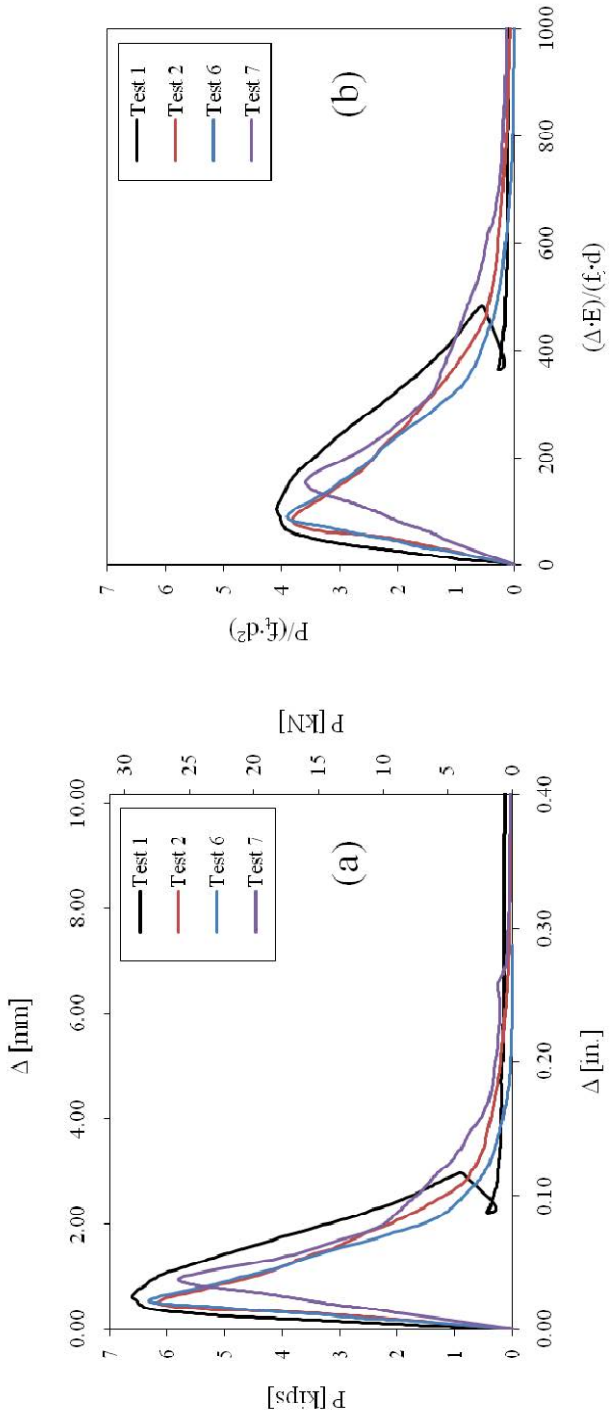

Fig. B1.6 – Load versus displacement curves, $d/c = 2$, $\lambda = 0$; (a) Dimensional, (b) Nondimensional

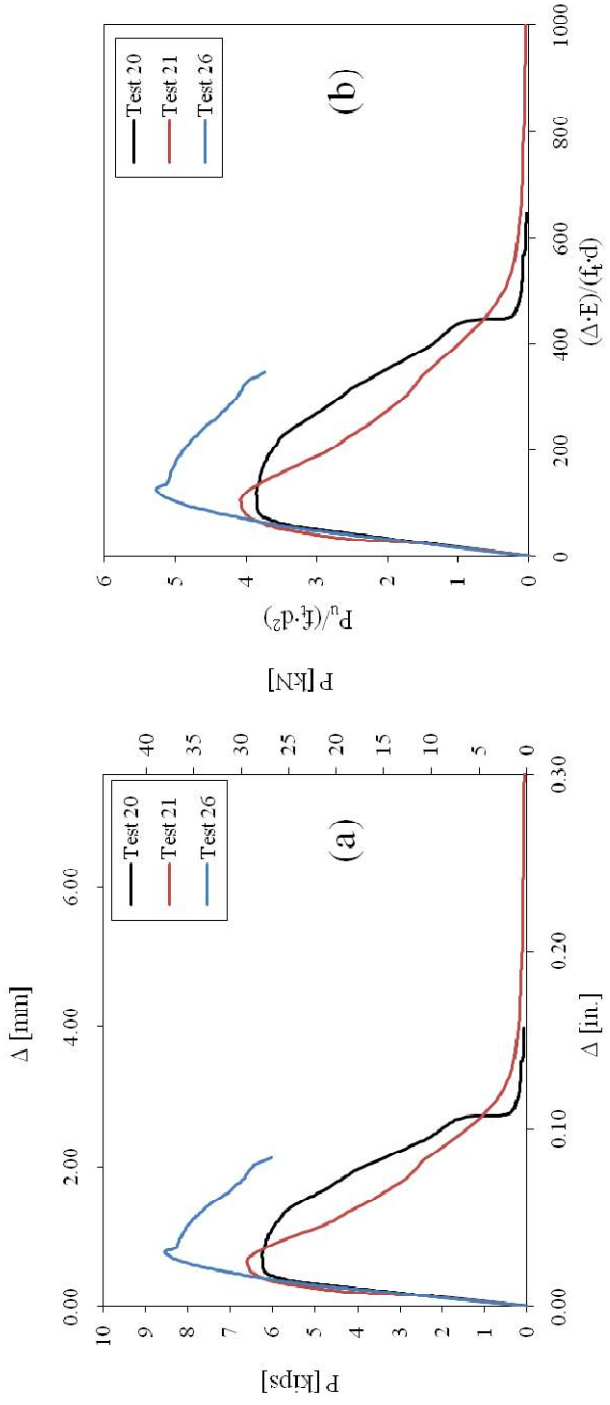

Fig. B1.7 – Load versus displacement curves, $d/c = 2$, $\lambda = 0.47$; (a) Dimensional, (b) Nondimensional

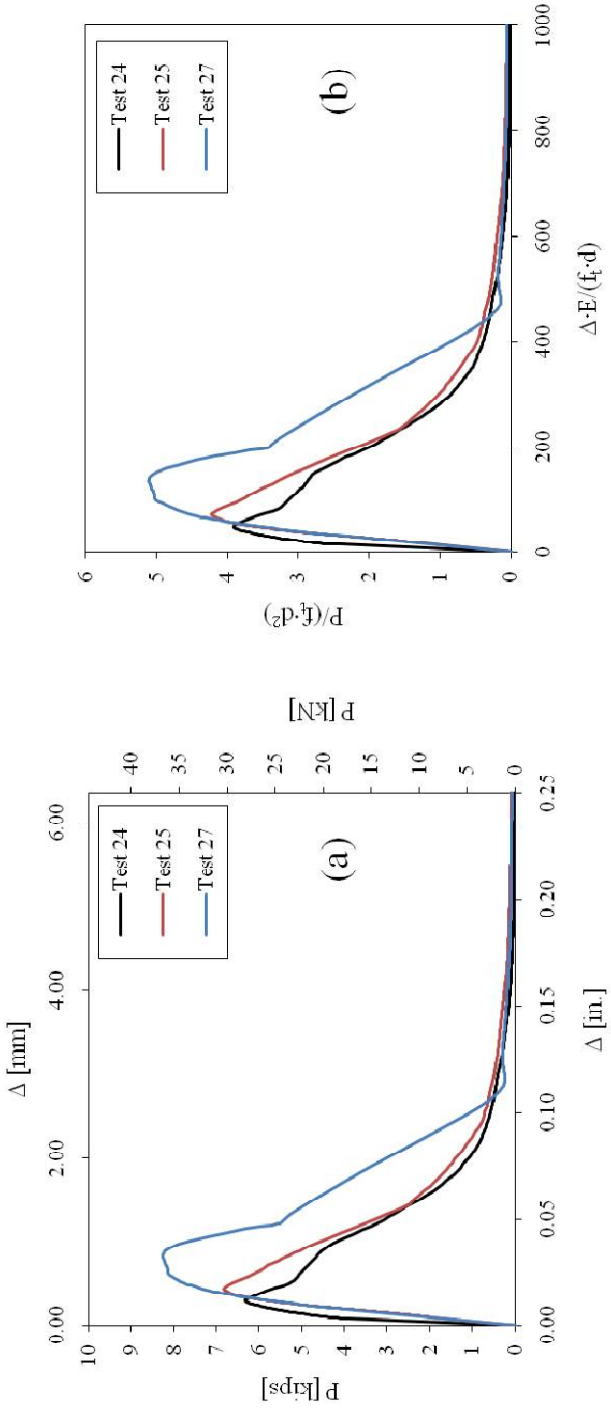

Fig. B1.8 – Load versus displacement curves, $d/c = 2$, $\lambda = 0.7$; (a) Dimensional, (b) Nondimensional

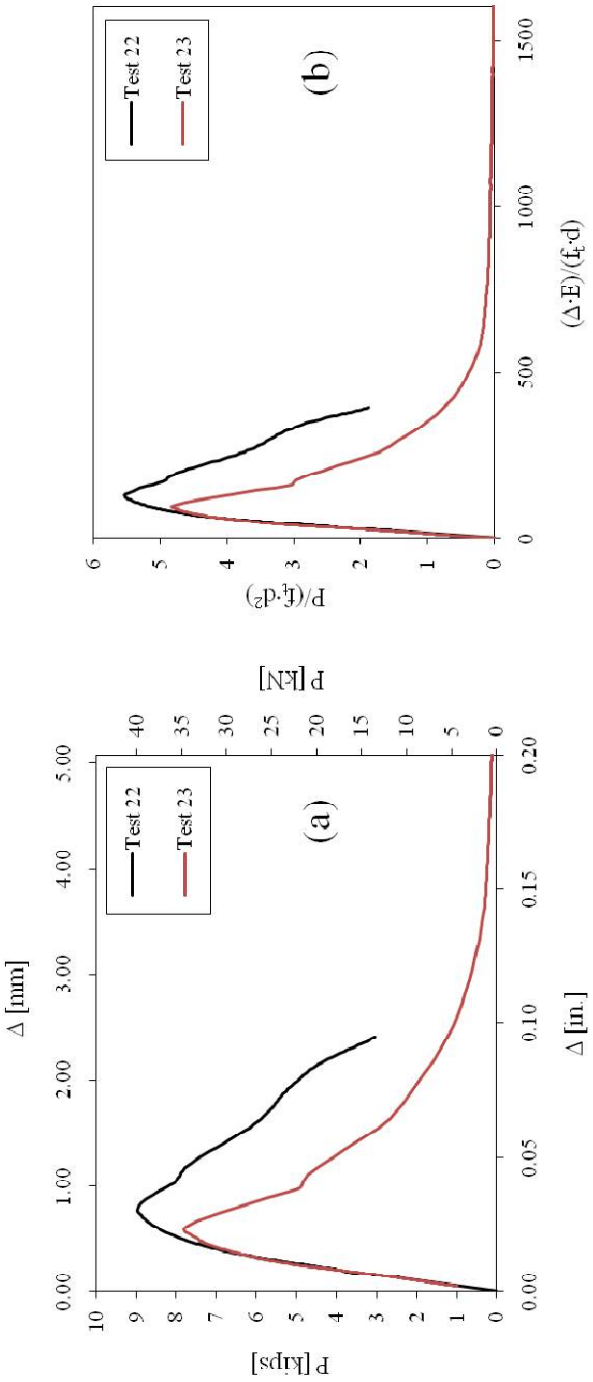

Fig. B1.9 – Load versus displacement curves, $d/c = 2$, $\lambda = 0.94$; (a) Dimensional, (b) Nondimensional

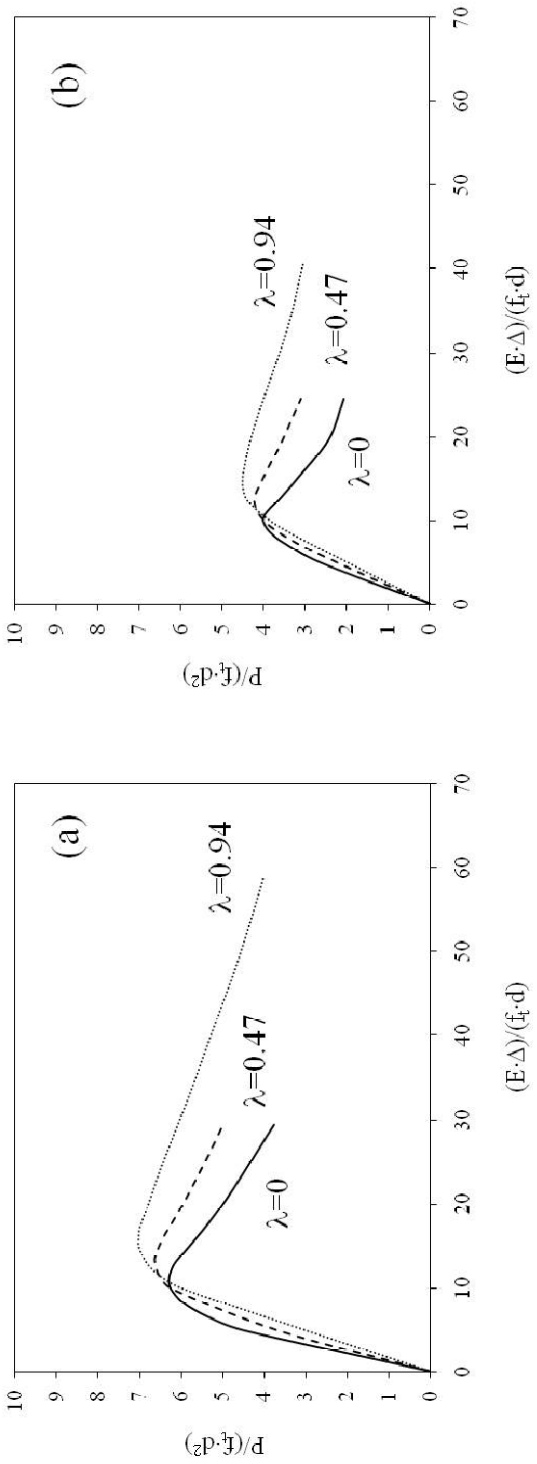

Fig. B1.10 – Normalized load versus displacement curves from NLFM finite element simulations; (a) $d/c=1$; (b) $d/c=2$

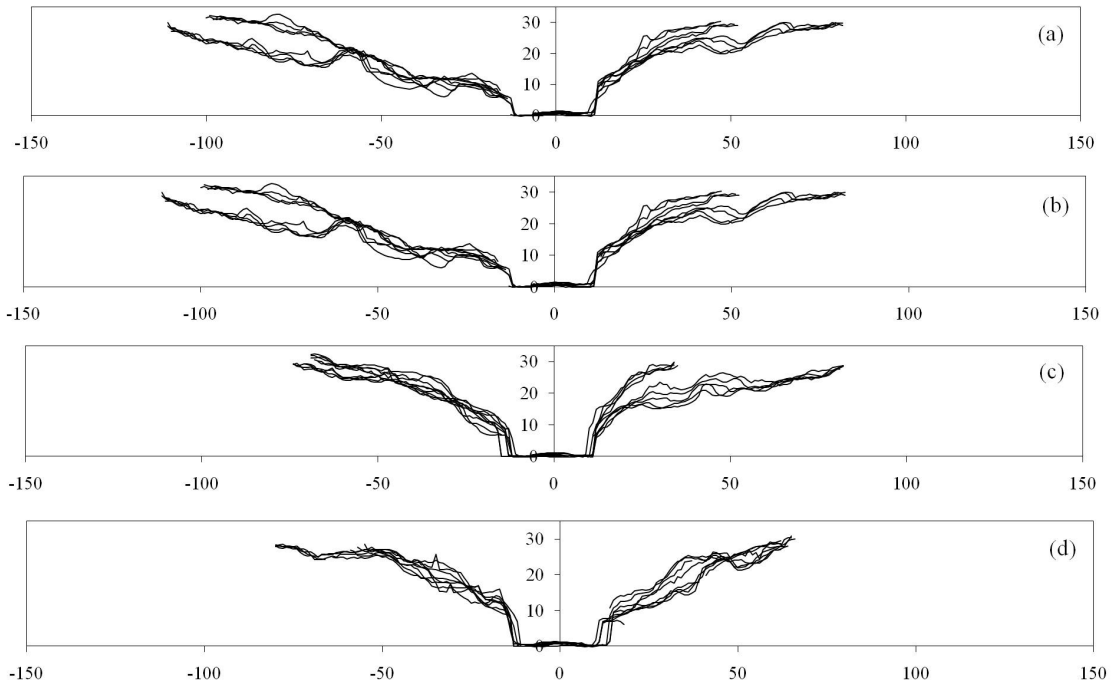

Fig. B1.11 – 2-D experimental crack profiles (from laser scanner), $d/c = 1$, and $\lambda = 0$;

(a) Test 8, (b) Test 9, (c) Test 10, (d) Test 11 (measures in mm)

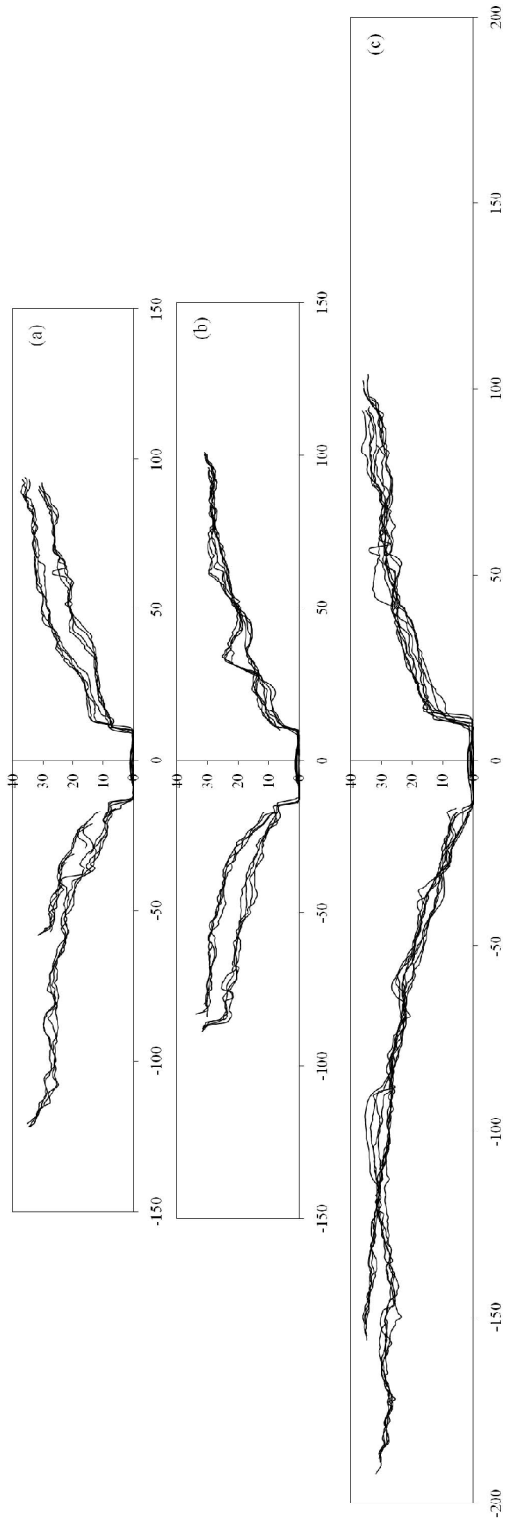

Fig. B1.12 – 2-D experimental crack profiles (from laser scanner), $d/c = 1$, and $\lambda = 0.47$; (a) Test 12, (b) Test 15, (c) Test 16 (measures in mm)

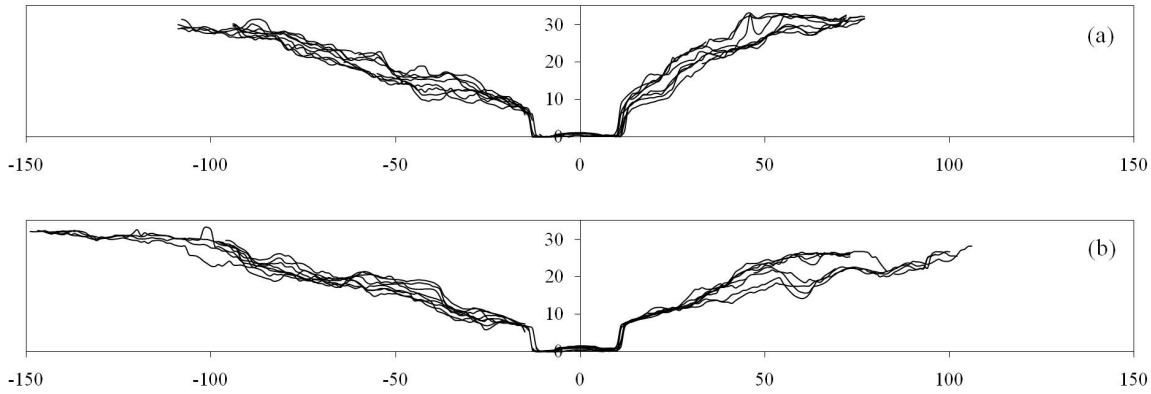

Fig. B1.13 – 2-D experimental crack profiles (from laser scanner), $d/c = 1$, and $\lambda = 0.7$;

(a) Test 18, (b) Test 19 (measures in mm)

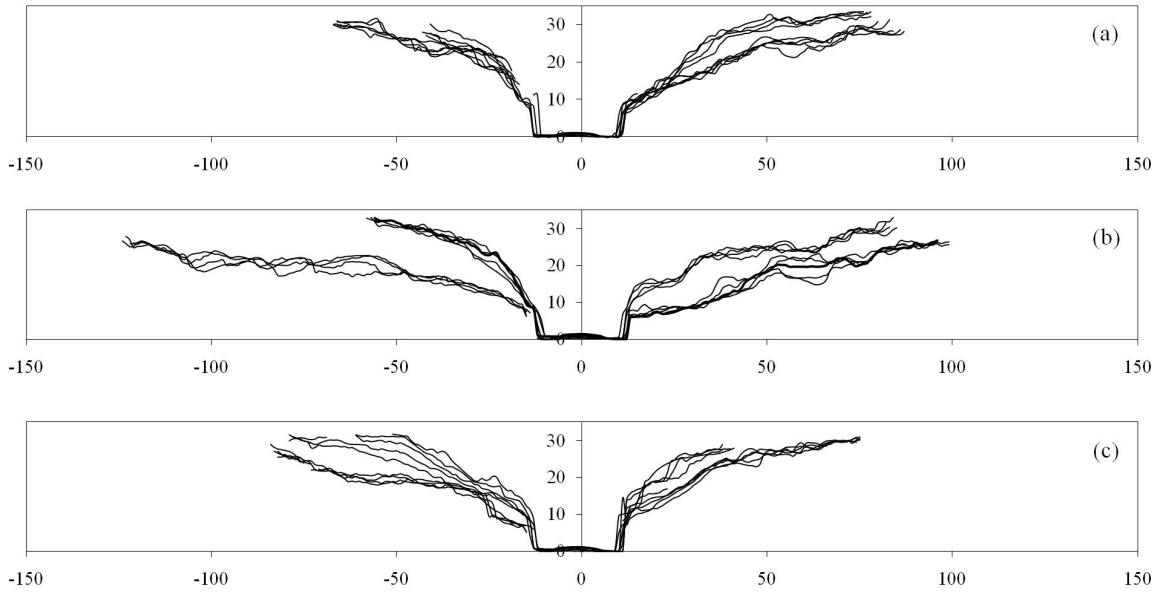

Fig. B1.14 – 2-D experimental crack profiles (from laser scanner), $d/c = 1$, and $\lambda = 0.94$; (a) Test 13, (b) Test 14, (c) Test 17 (measures in mm)

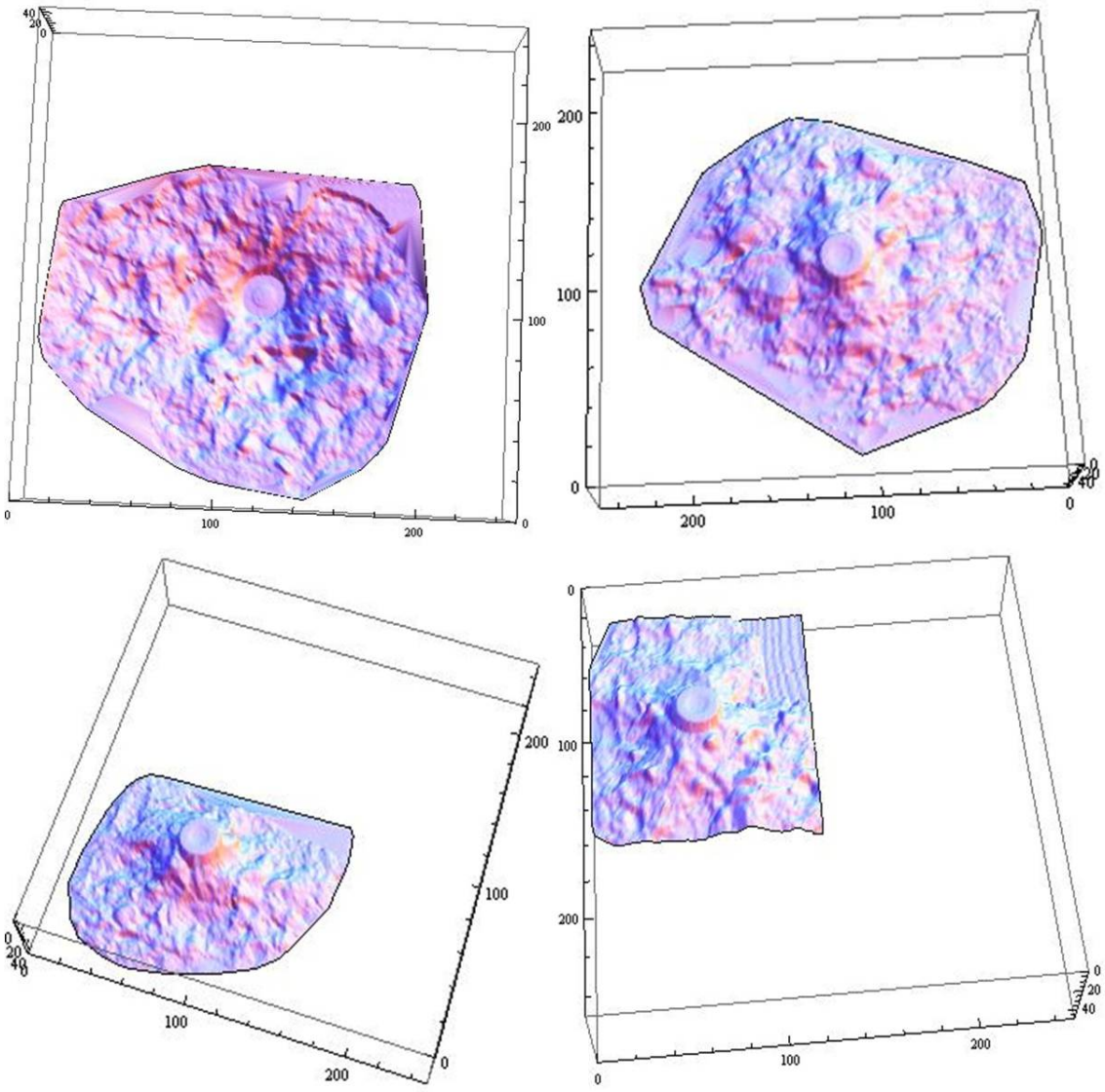

Fig. B1.15 – 3-D experimental crack profiles (from laser scanner), $d/c = 1$; Tests 8, 9, 10, and 11 (from top left, clockwise)

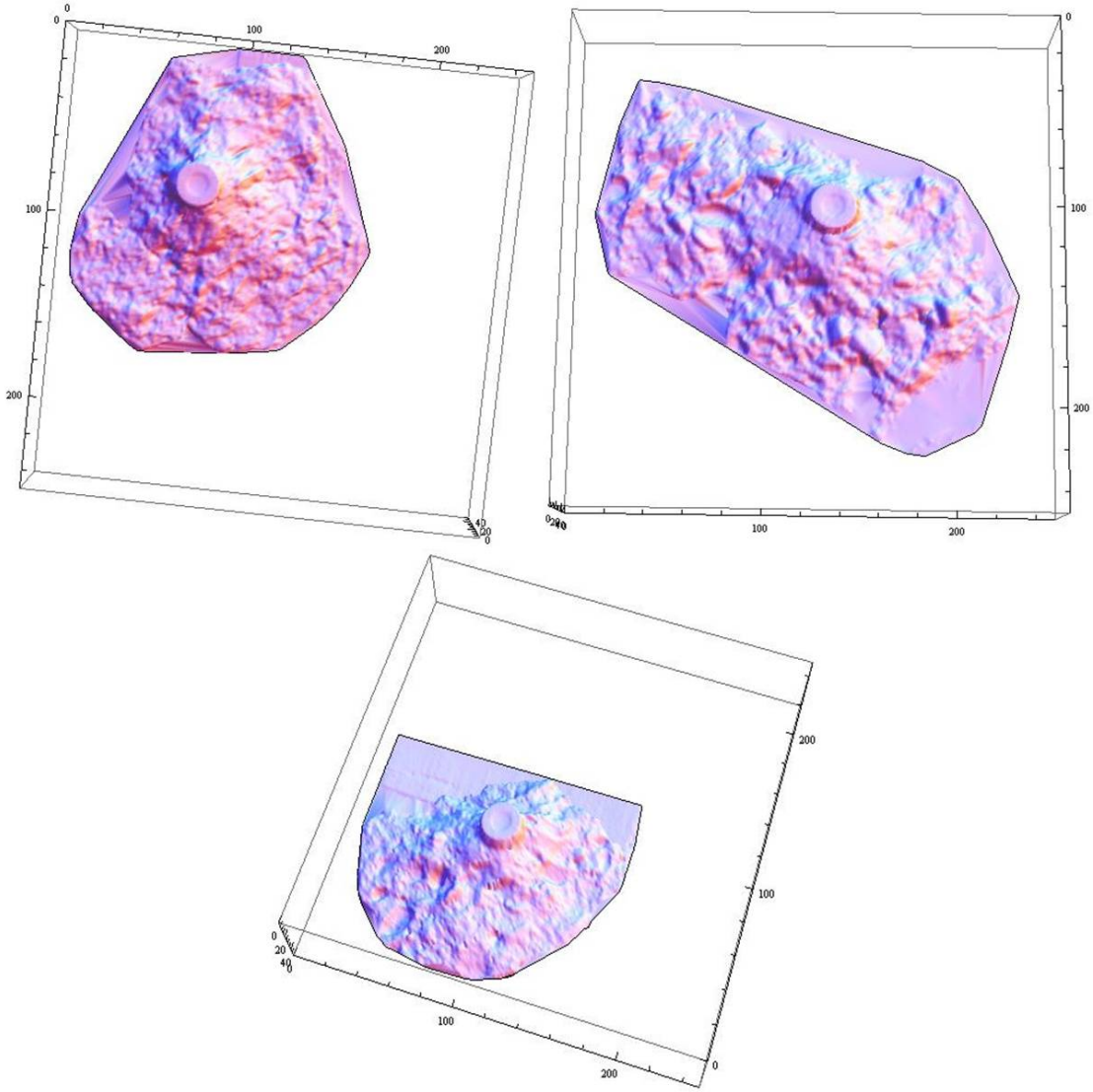

Fig. B1.16 – 3-D experimental crack profiles (from laser scanner), $d/c = 1$; Tests 13, 14, and 17 (from top left, clockwise)

B2.1 Experiments: Part II

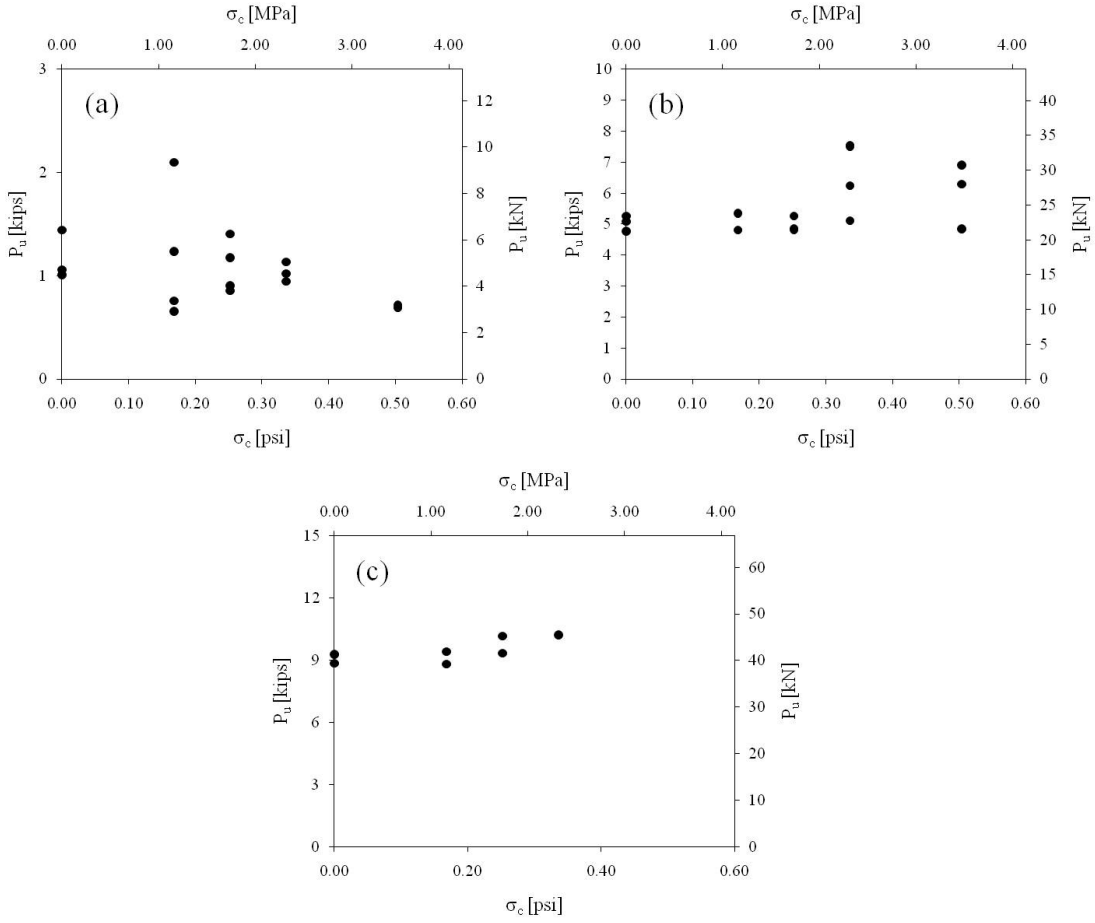

Fig. B2.1 – Ultimate load carrying capacities as function of prestress; (a) $d/c = 0.75$; (b) $d/c = 2$; (c) $d/c = 2.75$

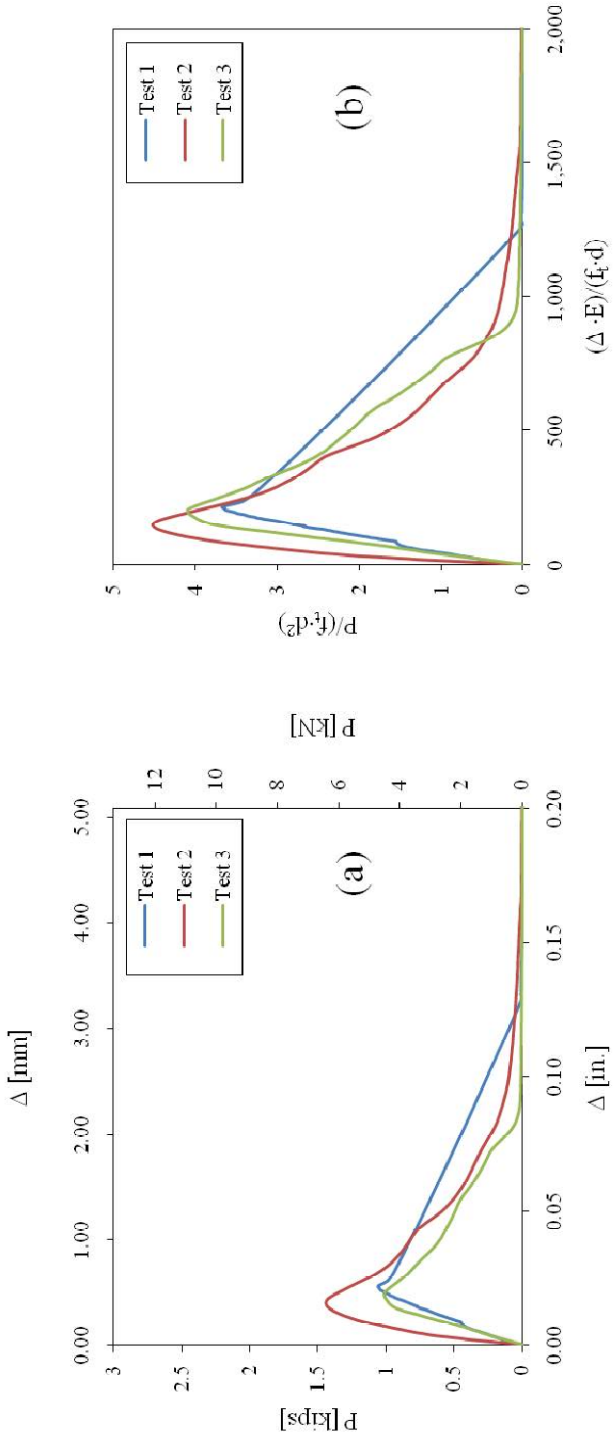

Fig. B2.2 – Load versus displacement curves, $d/c = 0.75$, $\lambda = 0$; (a) Dimensional, (b) Nondimensional

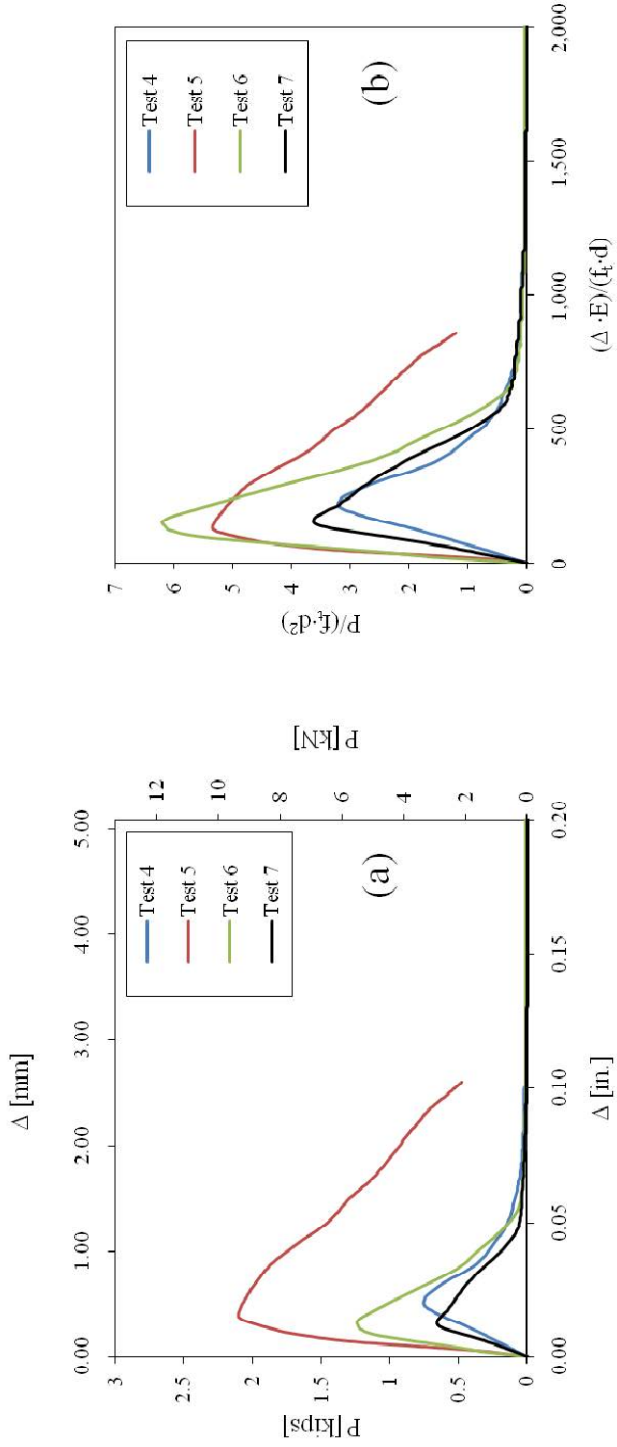

Fig. B2.3 – Load versus displacement curves, $d/c = 0.75$, $\lambda = 0.41$; (a) Dimensional, (b) Nondimensional

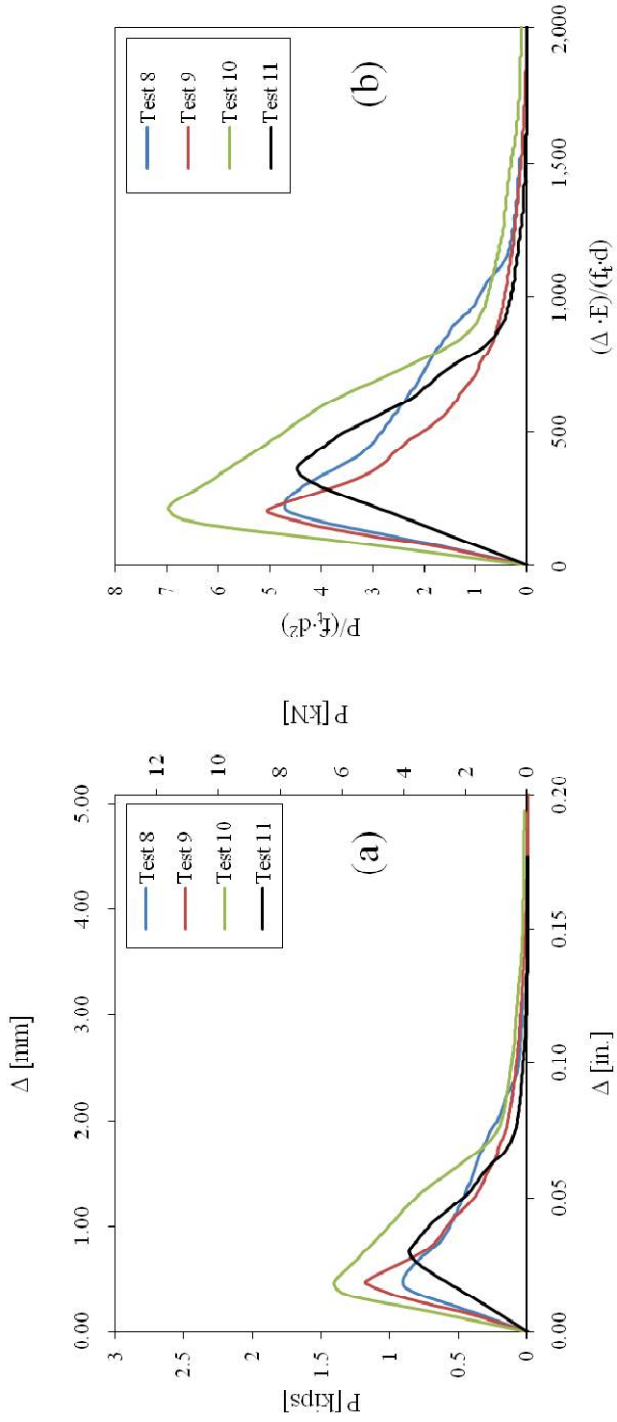

Fig. B2.4 – Load versus displacement curves, $d/c = 0.75$, $\lambda = 0.61$; (a) Dimensional, (b) Nondimensional

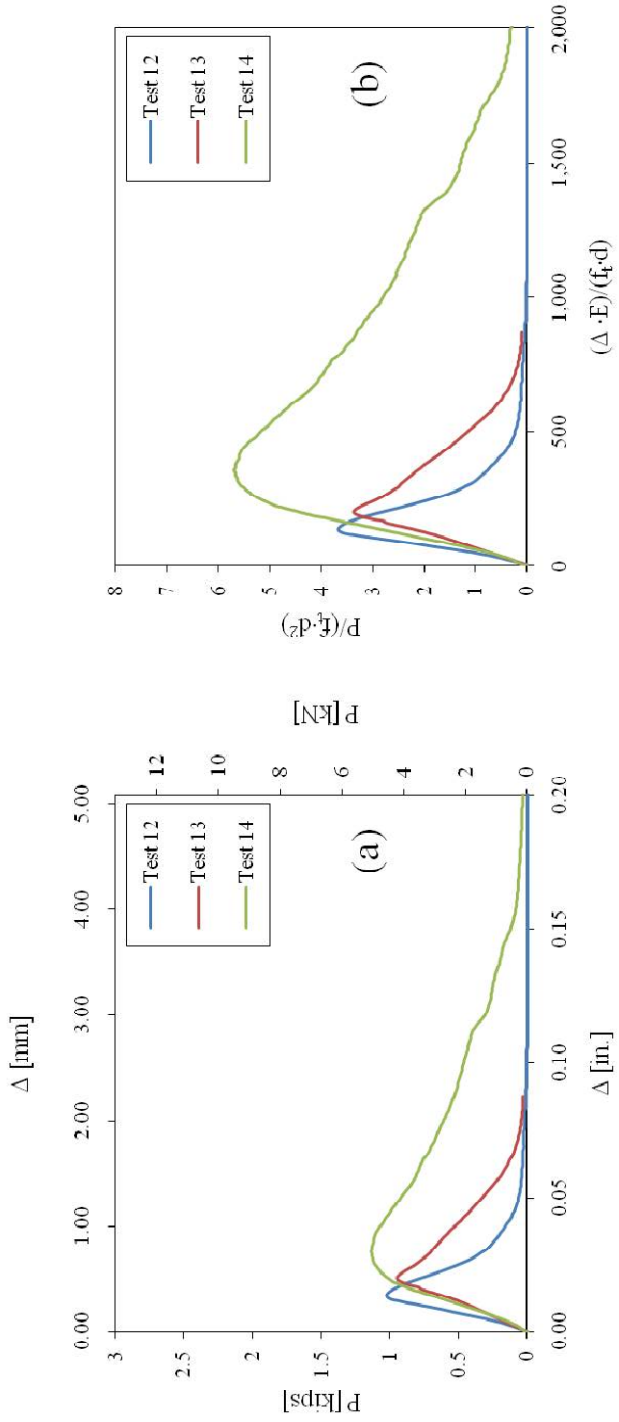

Fig. B2.5 – Load versus displacement curves, $d/c = 0.75$, $\lambda = 0.82$; (a) Dimensional, (b) Nondimensional

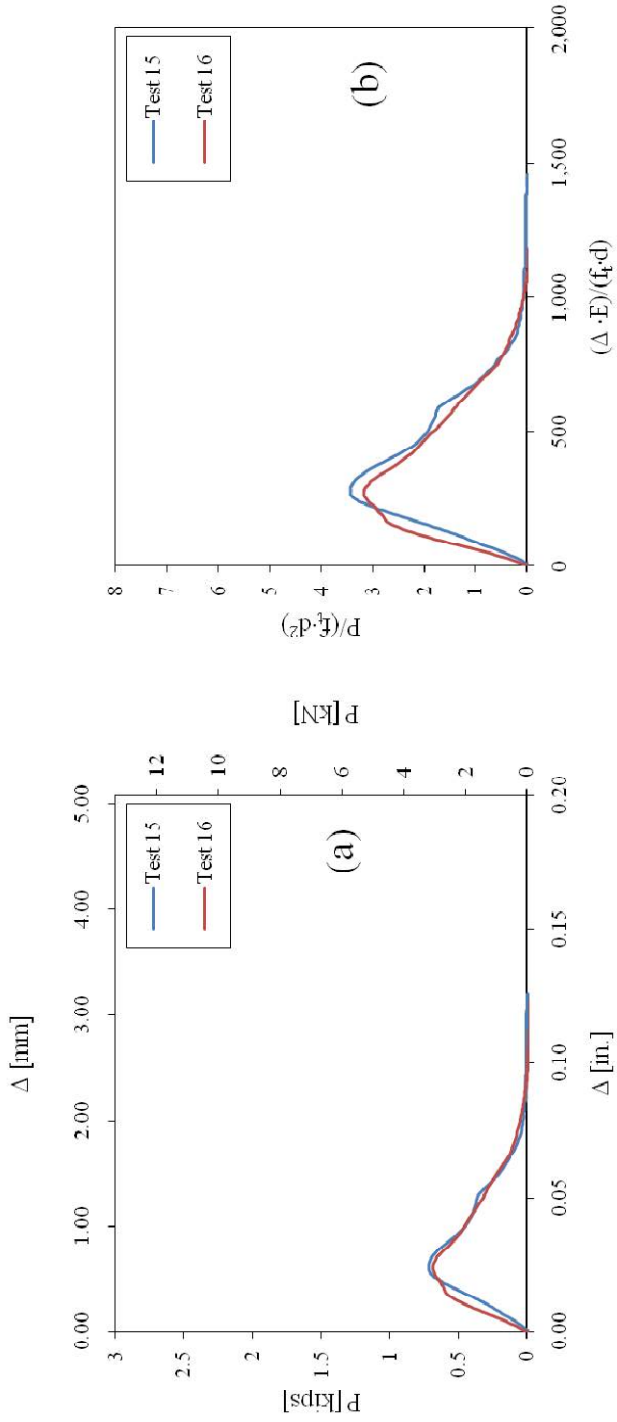

Fig. B2.6 – Load versus displacement curves, $d/c = 0.75$, $\lambda = 1.22$; (a) Dimensional, (b) Nondimensional

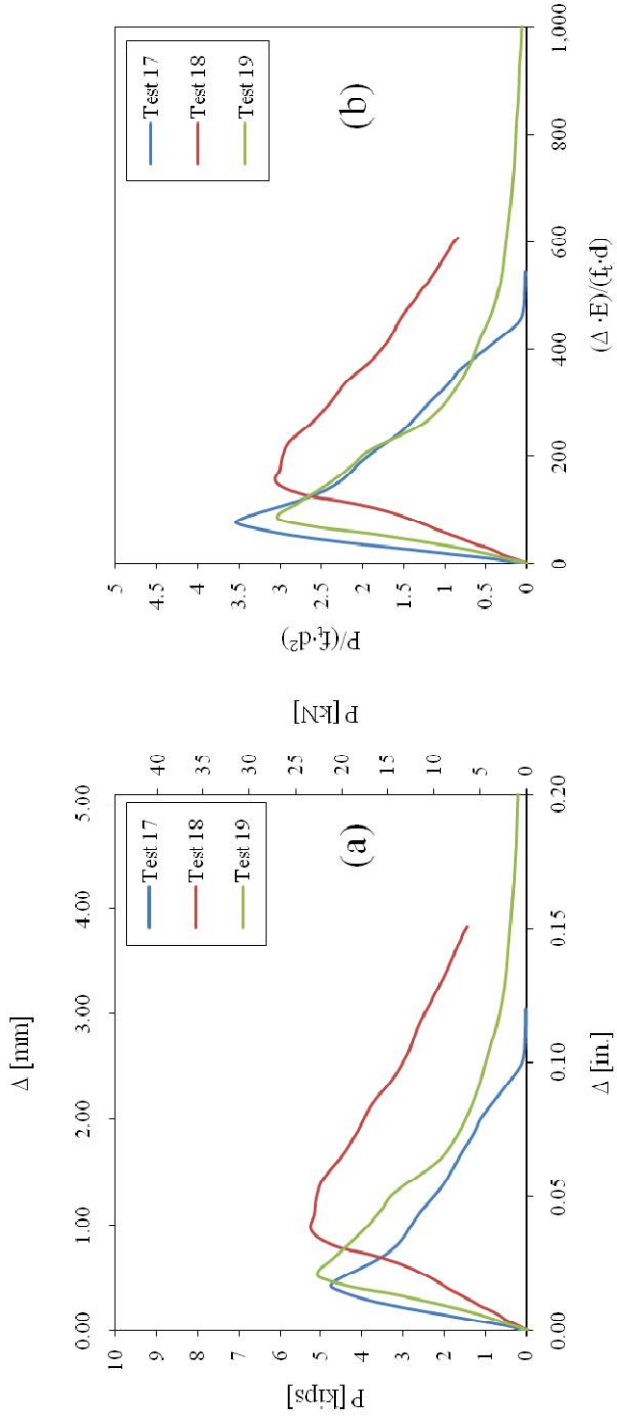

Fig. B2.7 – Load versus displacement curves, $d/c = 2$, $\lambda = 0$; (a) Dimensional, (b) Nondimensional

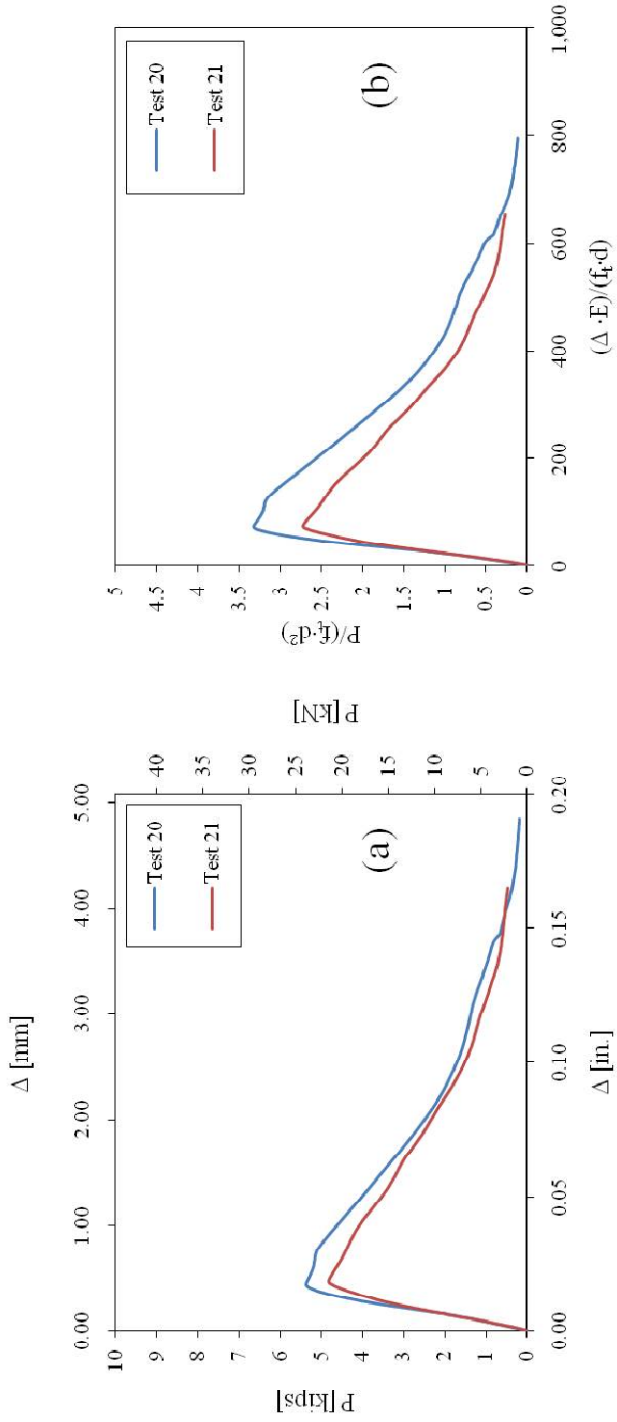

Fig. B2.8 – Load versus displacement curves, $d/c = 2$, $\lambda = 0.41$; (a) Dimensional, (b) Nondimensional

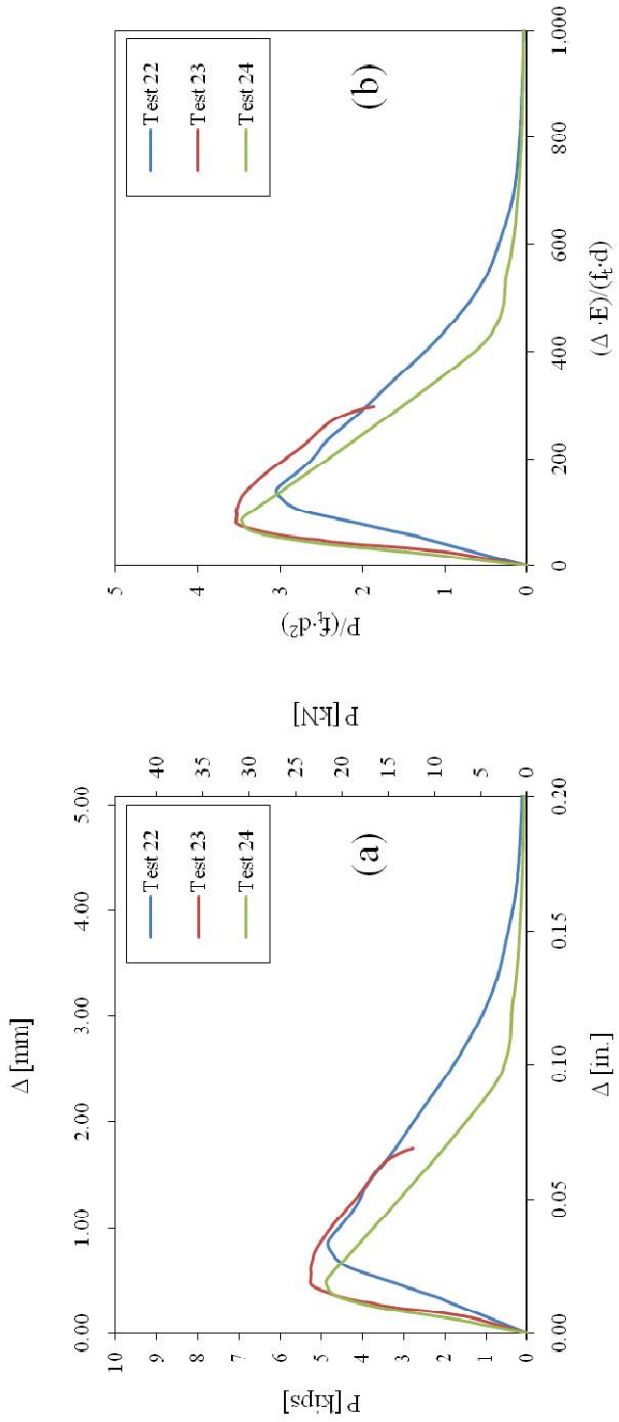

Fig. B2.9 – Load versus displacement curves, $d/c = 2$, $\lambda = 0.61$; (a) Dimensional, (b) Nondimensional

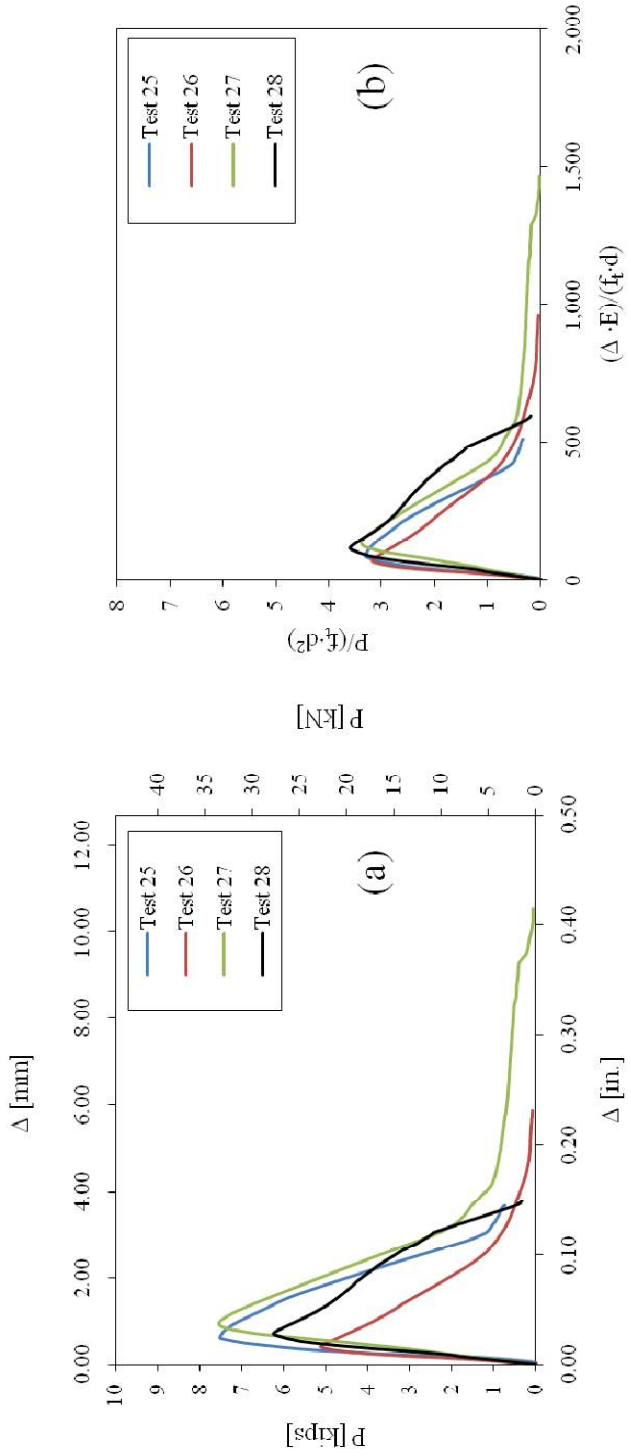

Fig. B2.10 – Load versus displacement curves, $d/c = 2$, $\lambda = 0.82$; (a) Dimensional, (b) Nondimensional

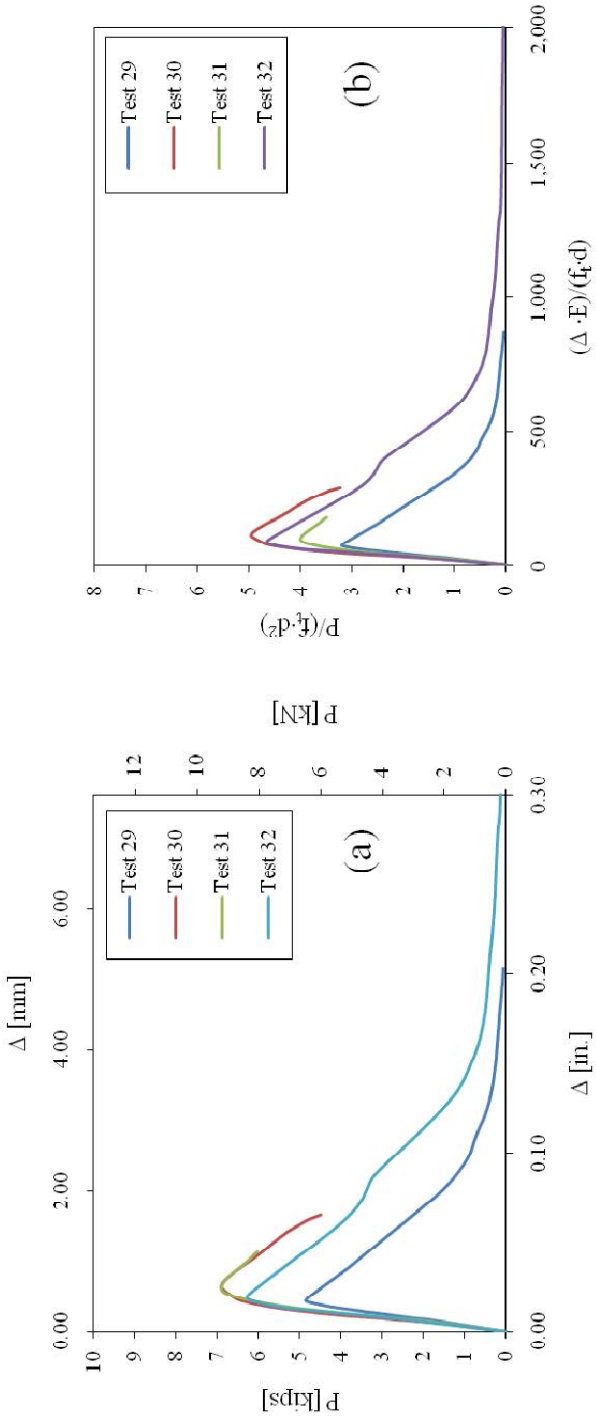

Fig. B2.11 – Load versus displacement curves, $d/c = 2$, $\lambda = 1.22$; (a) Dimensional, (b) Nondimensional

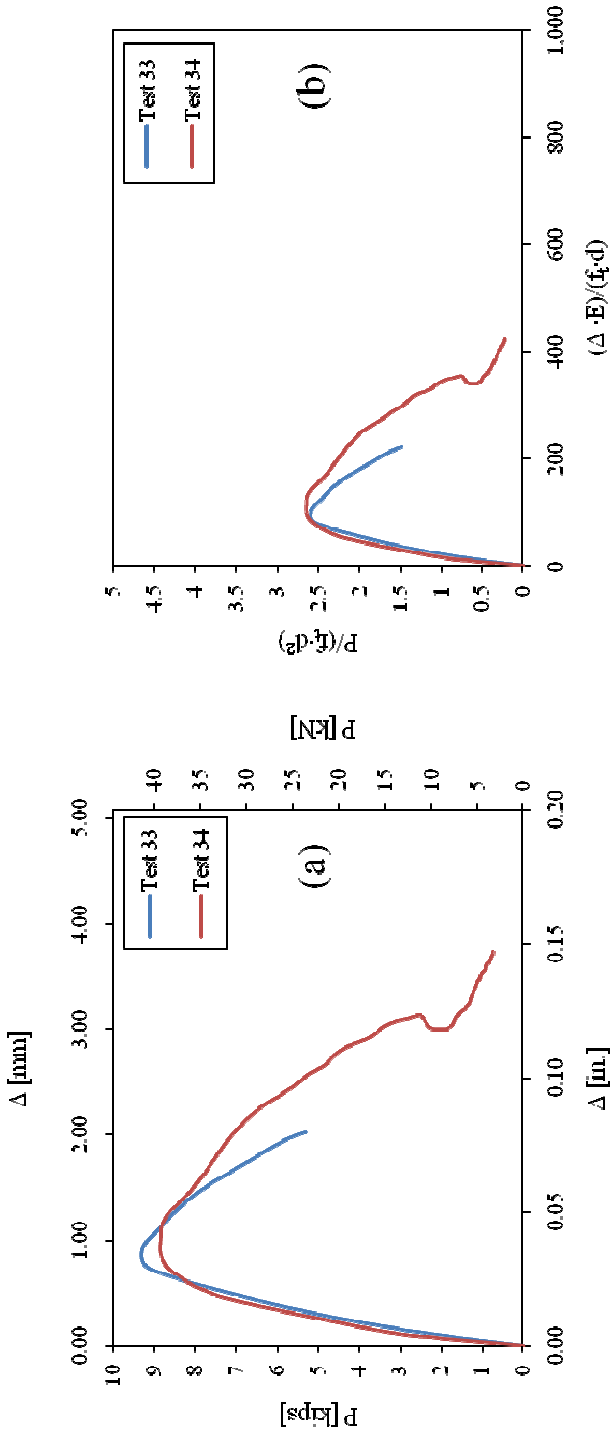

Fig. B2.12 – Load versus displacement curves, $d/c = 2.75$, $\lambda = 0$; (a) Dimensional, (b) Nondimensional

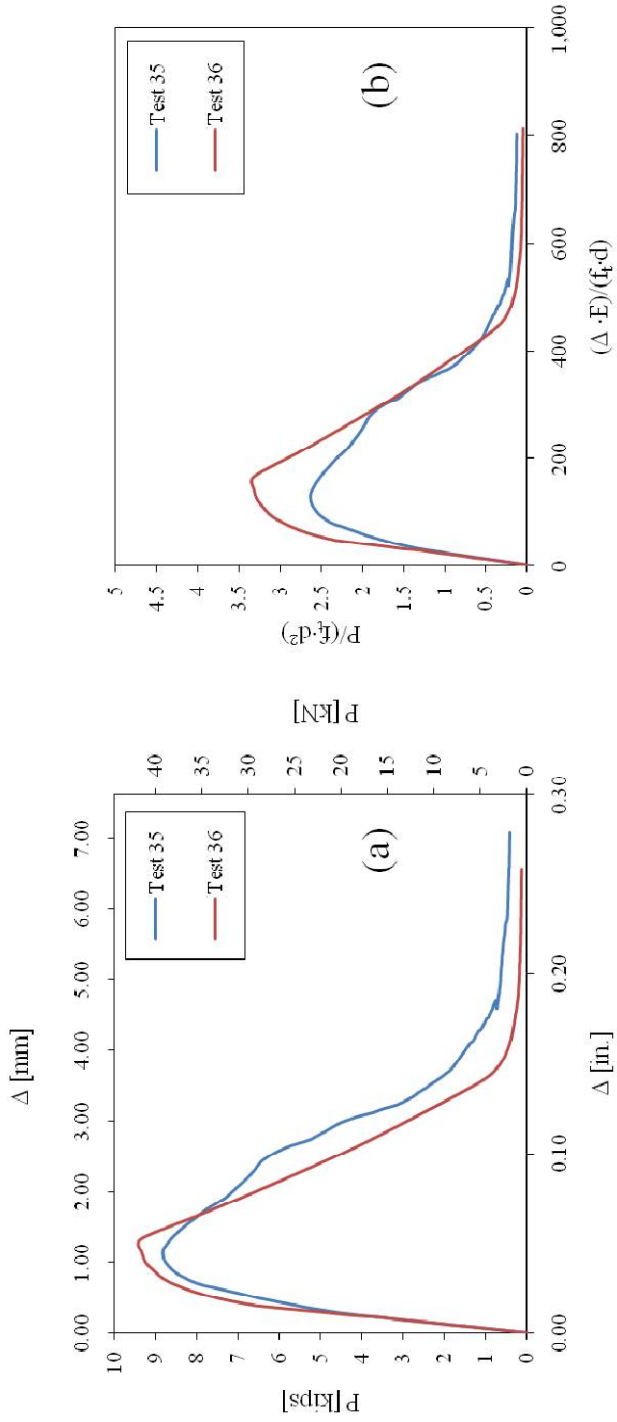

Fig. B2.13 – Load versus displacement curves, $d/c = 2.75$, $\lambda = 0.41$; (a) Dimensional, (b) Nondimensional

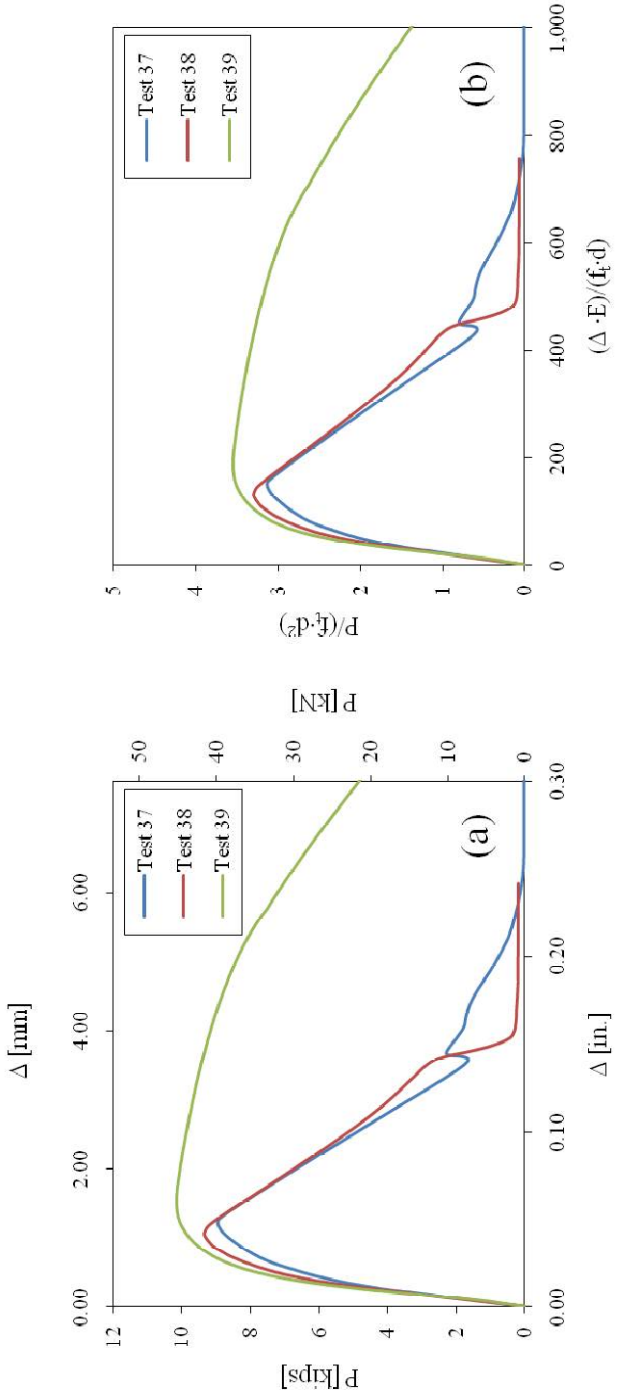

Fig. B2.14 – Load versus displacement curves, $d/c = 2.75$, $\lambda = 0.61$; (a) Dimensional, (b) Nondimensional

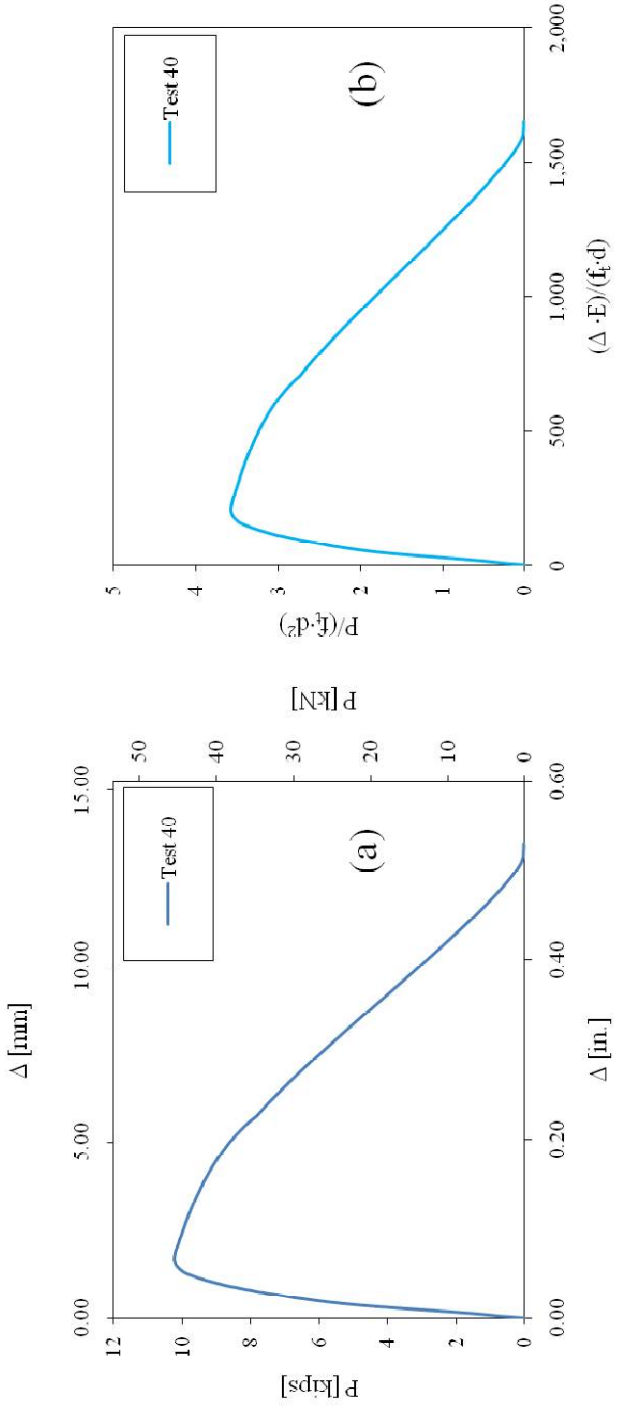

Fig. B2.15 – Load versus displacement curves, $d/c = 2.75$, $\lambda = 0.82$; (a) Dimensional, (b) Nondimensional

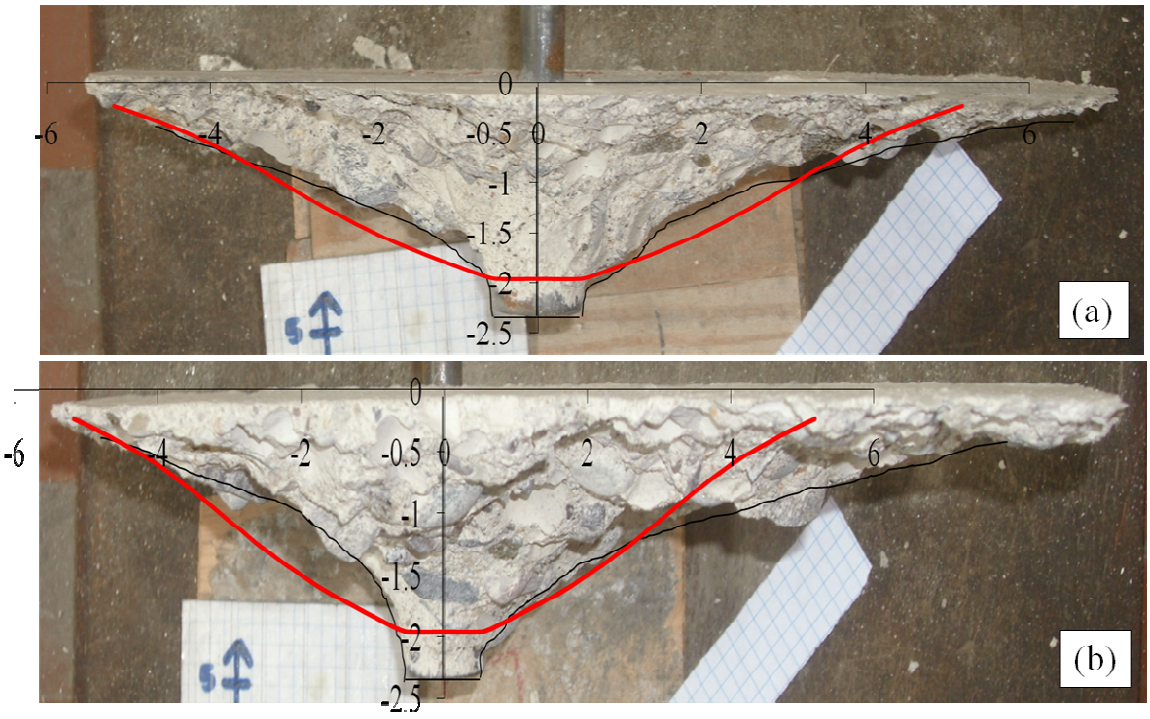

Fig. B2.16 – Experimental and LEFM crack paths, $d/c = 2$ and $\lambda = 0$; (a) Test 17; (b) Test 19 (measures in in.)

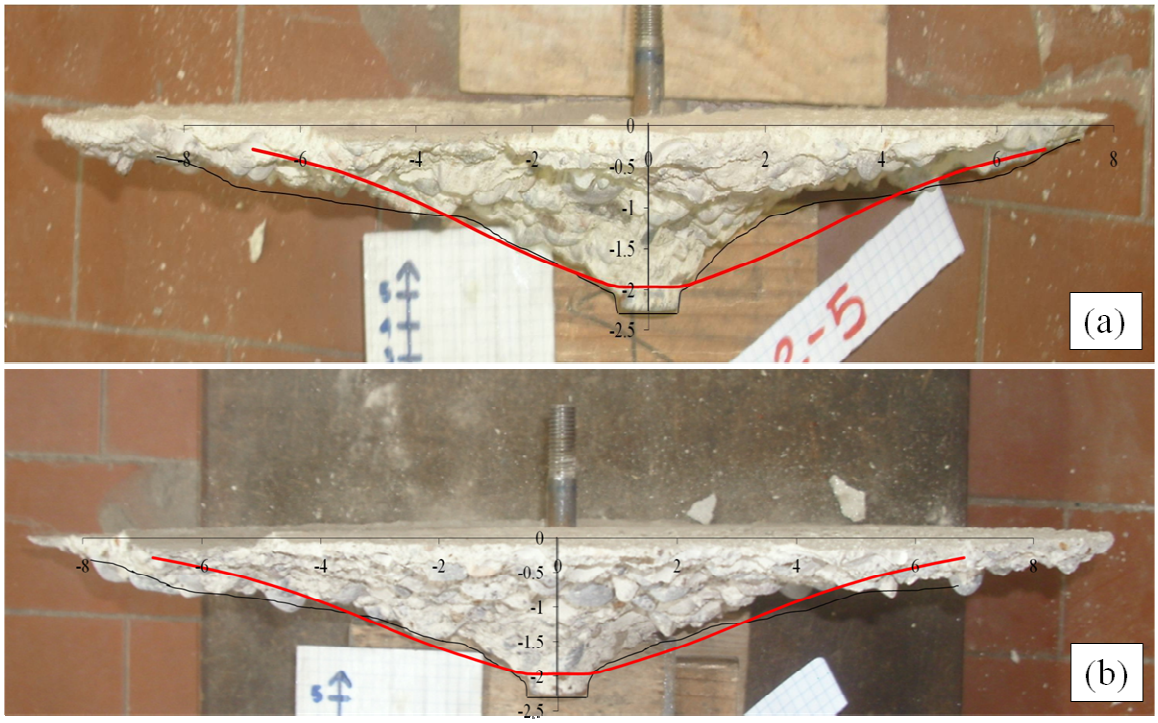

Fig. B2.17 – Experimental and LEFM crack paths, $d/c = 2$ and $\lambda = 0.41$; (a) Test 20; (b) Test 21 (measures in in.)

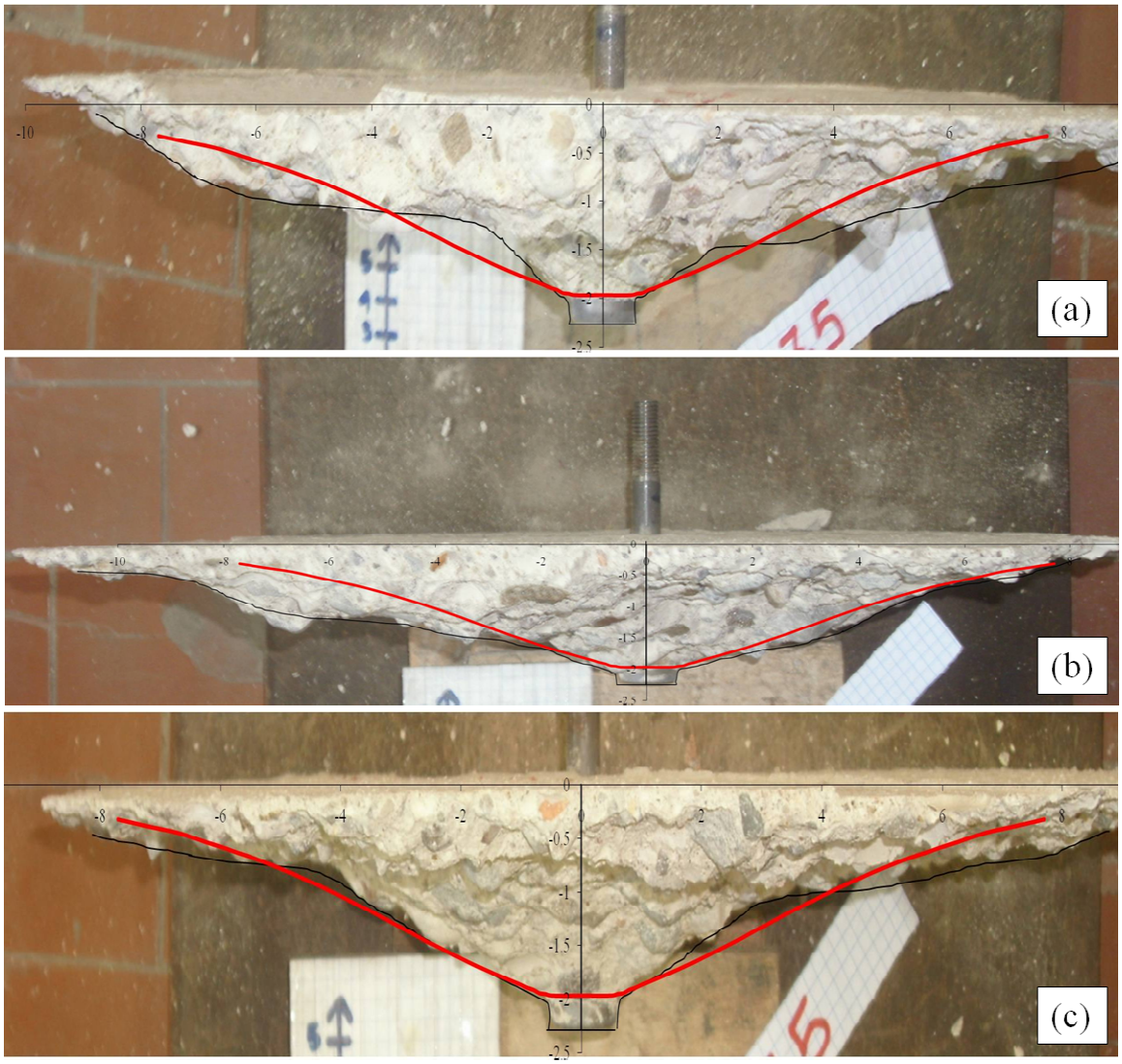

Fig. B2.18 – Experimental and LEFM crack paths, $d/c = 2$ and $\lambda = 0.61$; (a) Test 22; (b) Test 23; (c) Test 24 (measures in in.)

Fig. B2.19 – Experimental and LEFM crack paths, $d/c = 2$ and $\lambda = 0.82$; (a) Test 26; (b) Test 27 (measures in in.)